Study of the kink instability and twist distribution of heliospheric magnetic flux ropes

NASA Goddard Space Flight Center
Heliophysics Science Division (HSD)

Universitat Politècnica de Catalunya
Degree in Mathematics - Degree in Engineering Physics

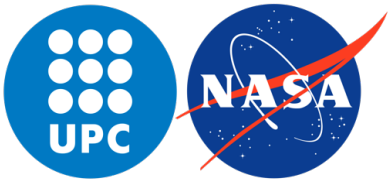

Marta Florido Llinàs

Bachelor Thesis

Degree in Mathematics - Degree in Engineering Physics

Supervisor (NASA GSFC): Teresa Nieves Chinchilla
Co-supervisor (UPC): Jordi José Pont

May 2020

Abstract

Magnetic flux ropes (MFRs) are fundamental plasma structures consisting of magnetic field lines twisted around an axis. They appear in many heliospheric phenomena, including one of the main drivers of adverse space weather: coronal mass ejections (CMEs). Understanding their internal magnetic structure and dynamics is therefore essential to foretell and mitigate their potentially damaging consequences in technological systems. This work starts by providing an explanation of fundamental concepts in heliophysics and magnetohydrodynamics for the modeling and analysis of MFRs. The Circular-Cylindrical (CC) analytical model for magnetic clouds is then studied to include the phenomenon of expansion. Two different reconstruction techniques for CMEs, the Graduated Cylindrical Shell model and the CC model, are compared for a particular event detected by Parker Solar Probe on March 15, 2019, contributing to an article submitted to The Astrophysical Journal (Lario et al., in review). A numerical method has been developed to analyze the helical kink stability of MFRs with different twist profiles, and the results are discussed with the aim of shedding some light on the dynamics of MFRs and the occurrence of rotations, magnetic forces and expansion, among others. A publication with the methodology and outcomes of the stability analysis, obtained in collaboration with the supervisor at NASA GSFC, Teresa Nieves-Chinchilla, and Mark George Linton at NRL (Naval Research Laboratory), has been submitted to Solar Physics (Florido-Llinas et al., in review). Finally, the numerical stability method is used to obtain the optimal values of the parameters of a MFR model, which result in an instability of convenient characteristics for nonlinear solar MHD simulations that will be carried out by researchers Kalman Knizhnik and Mark George Linton at NRL.

Keywords— magnetic flux ropes, kink instability, coronal mass ejections, twist distribution

AMS2020 Code— 76E25, 85-10

Acknowledgements

I would like to express my gratitude to Teresa Nieves Chinchilla for giving me the opportunity to do my bachelor thesis in her research group at NASA Goddard Space Flight Center, for her unconditional availability to solve my doubts and share her knowledge with me, and for her passion and guidance while supervising me during this experience.

Thanks to Mark George Linton, David Lario, Luiz Guedes and Daniel Berdichevsky for the interesting and valuable discussions, and to all the members of the Heliospheric Physics Laboratory for their constant eagerness to share their expertise and experience.

I also wish to thank CFIS and Cellex foundation, in particular Miguel Ángel Barja and Toni Pascual, for making this Mobility Program possible.

And finally, thanks to my family for their endless encouragement and support throughout my studies.

Contents

Introduction

Coronal mass ejections (CMEs) are one of the main drivers of adverse space weather. They are large eruptions of magnetized plasma with the ability to severely impact telecommunications and space systems, due to the sudden injection of magnetic energy into the magnetosphere. CMEs are typically modeled as magnetic flux ropes (MFRs), twisted magnetic configurations that are prone to develop a particular type of plasma instability, the so-called kink instability.

Understanding CMEs internal magnetic structure has become a very important challenge, since it provides the ability to foretell sufficiently far in advance their eruption and evolution, and therefore to mitigate their potentially damaging effects in technological systems and society.

In the first and second chapters of the present work, fundamental concepts will be given about solar physics and CMEs, as well as of the field in charge of studying plasma behavior: magnetohydrodynamics. In particular, the theoretical background behind the MFR modeling of CMEs and the linear stability analysis used in this thesis, will be explained.

The third chapter discusses in detail some of the most common MFR models for CMEs and the importance of the twist distribution in the physical properties and dynamics of these structures. The Circular-Cylindrical (CC) analytical flux-rope model for magnetic clouds is examined more in depth to include the possibility of expansion. In addition, two different reconstruction techniques (the Graduated Cylindrical Shell model and the CC model) are compared in the context of the analysis of a particular CME detected by Parker Solar Probe on March 15, 2019.

The fourth chapter describes the numerical method that has been developed in this thesis as a general method to study the linear kink stability of cylindrical MFRs. It is first applied to differently twisted MFR models and the results are discussed in relation to the occurrence of rotations, magnetic forces and expansion throughout the interplanetary medium, among others. Finally, this numerical stability method is used to obtain optimal parameters for nonlinear MHD simulations of ongoing solar physics research.

1 . Fundamentals of the Sun and CMEs

The study of the variability of the Sun and solar phenomena, as well as of its impact on the vast heliosphere and the environment of planets, has become essential for a society that is increasingly reliant on advanced technological systems. Understanding the magnetic structure and dynamics of the Sun and of adverse space weather events is therefore of critical importance in order to protect our technology and way of life from their potentially damaging consequences. This chapter presents an overview of the current knowledge about the Sun and its largest eruptive phenomena, the so-called coronal mass ejections (CMEs).

1.1 Discovering the Sun and its magnetic field

1.1.1 Historical remarks

The Sun has been an object of great fascination and interest for humans for thousands of years. Not only is it essential for life on Earth, providing the energy, heat and light that is vital to all living organisms, but it also causes radiative and eruptive phenomena whose accompanying energy and magnetic fields can severely interfere with technological systems, both on Earth and its orbit. The study of the Sun allows us to understand how its ever-changing conditions affect our planet and the interplanetary medium, and this knowledge can be extended to stellar systems that are only viewed from afar.

The first observations of the Sun and the effects of space weather date back centuries. There are written records of aurorae from as far back as 2600 BC in China, and reports of simultaneous deviations of compass needles caused by geomagnetic storms in 1724 (Howard, 2011). Even naked-eye observations of *sunspots* (dark regions of lower temperature that appear on the visible surface of the Sun) of the period 165 BC - 1918 AD have been compiled from historical documents and are used nowadays to understand long-period solar variability (Vaquero et al., 2002).

Up until the start of the 20th century, many of the processes taking place within and beyond the Solar System were poorly understood, let alone the magnetic forces that are now known to be responsible for most of the activity and variability of the Sun. In the early 17th century, there were astronomers like Galileo Galilei or Christoph Scheiner who measured the 27-day rotation period of the Sun through the observation of sunspots, and realized that its angular rotation rate decreased towards the poles. However, there was still a long way to go: theories stating that the Sun was a solid or liquid sphere, and that sunspots were meteor impacts or the solar analogs of terrestrial tornadoes or volcanoes, were the most widely accepted ones for a long time (Foukal, 1990).

The first discovery of extraterrestrial magnetic fields, made by George Ellery Hale in 1908, meant a breakthrough in the understanding of the forces pervading solar and space physics. He used the analysis made by the physicist Pieter Zeeman in 1897 of the effect of magnetic fields on spectral lines, and applied it to the study of sunspot spectra. Sunspots occupy regions that are usually as large as Earth and have temperatures of 3500-4500 K, which are much colder than the surrounding materials (about 5800 K), so they appear darker in the solar surface (see Figure 1.1). This is now known to be a consequence of their exceptionally strong magnetic fields (around 1500-3000 G, whereas the Sun's average surface field is 1 G), which inhibit heat convection. Therefore, when

Hale studied the Zeeman effect in sunspot spectra, he found that it showed fine structures that closely resembled iron filings sprinkled around magnets, providing the first evidence of the existence of solar magnetic fields. His findings revolutionized the study of the Sun, since he had actually discovered the main force driving almost all solar activity and a lot of heliophysics phenomena.

Understanding the solar non-spot or background magnetic fields became Hale's next challenge, but their Zeeman effect signatures were too weak to be detected with the technologies that existed back then. It was not until 1953 that his goal was achieved by Babcock with the invention of the photoelectric magnetograph (Harvey, 1999; Stenflo, 2017).

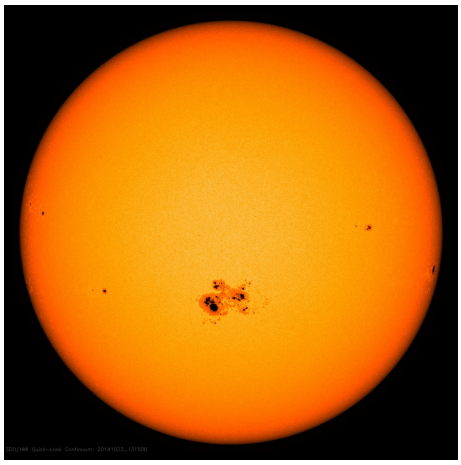

Figure 1.1: Photograph of the sunspot that grew to be the largest active region seen in the solar cycle that started in 2008, taken on October 18, 2014, by NASA Solar Dynamics Observatory (SDO); ten Earths could be laid across its diameter of $130 \cdot 10^6$ m. The largest sunspot ever recorded is almost three times as large as this one. Retrieved from NASA Image and Video Library.

1.1.2 Description of the Sun

Extensive studies have been done of the Sun's structure and magnetic field that provide us with a lot of information about it. For instance, *helioseismology* has revealed how the Sun's interior is organized by analyzing its oscillations, in a similar way as geoseismology uses seismic waves from earthquakes to describe the inside of the Earth. However, there are a lot of phenomena that still require a detailed explanation, such as how solar magnetic fields are generated or how the Sun accelerates particles in the form of solar wind or other transient phenomena like CMEs.

The Sun is now halfway through its life, being 4.6 billion years old. It has a mass of $1.99 \cdot 10^{30}$ kg (thus being 330,000 times more massive than Earth) and a radius of $6 \cdot 10^6$ m (109 times larger than Earth's radius). The mean distance between the Sun and the Earth is $1.496 \cdot 10^{11}$ m (defined as 1 AU), so light needs 8 minutes to travel from one to the other. It takes 250 million years to orbit the center of the Milky Way traveling at a speed of 220 km/s, and flips the polarity of its magnetic field every 11 years. The largest sunspot on its surface was measured in 1947, with 35 times the area of the Earth (Priest, 2013).

Figure 1.2 shows the structure of the Sun. The inner part of it is a massive plasma ball consisting of mostly ionised H (92% by number of atoms, or 73.4% by mass) and He (7.8% by number of atoms, or 25% by mass) atoms, with other elements like C, N and O that constitute about 0.1% of the total. The solar interior is shielded from our view, and only the surface layers can be observed directly, but helioseismology has been used to infer the existence of three main layers where different physical processes dominate:

- **Core:** It extends from the center to about $0.2R_s$ and $0.25R_s$, where R_s is the solar radius. This is where the energy of the star is generated and it is found at around $15 \cdot 10^6$ °C. The exceptionally high temperatures combined with the huge pressure and density, force the

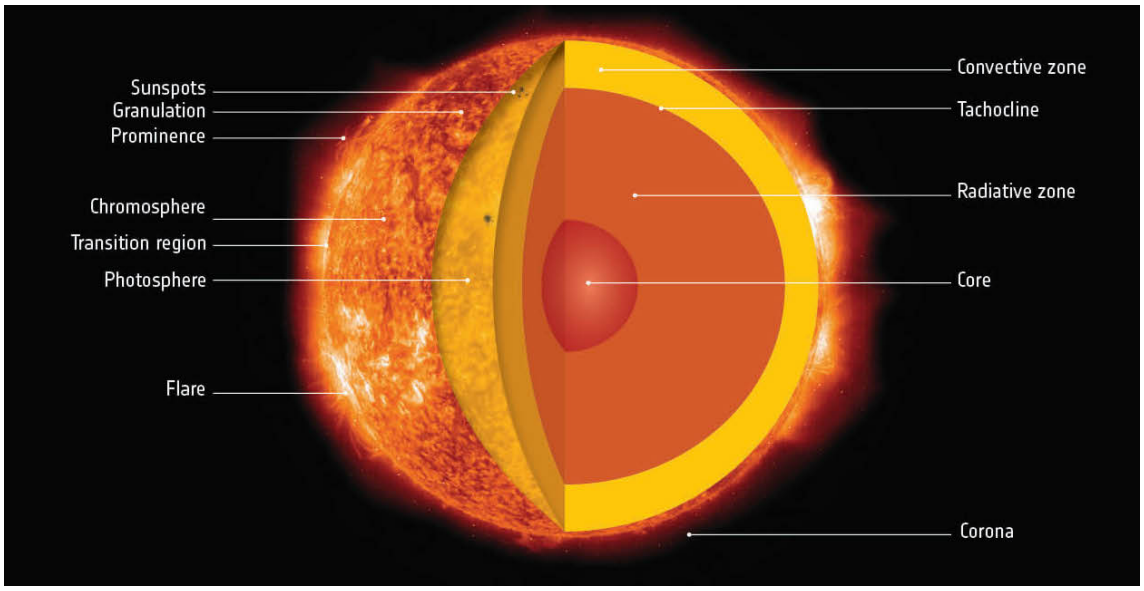

Figure 1.2: Structure of the Sun. Retrieved from `http://www.esa.int/ESA_Multimedia/Images/2019/10/Anatomy_of_our_Sun`.

occurrence of fusion between hydrogen nuclei, resulting in the creation of helium and the release of vast quantities of energy. Every second, the Sun converts $4 \cdot 10^9$ kg of matter into energy that will reach the surface after going through a very slow journey.

- **Radiative zone:** It extends from the core to about $0.7R_s$. The temperature goes from $7 \cdot 10^6$ °C next to the core to $2 \cdot 10^6$ °C at the top of the layer. The density of the plasma in this region is still so high that convection cannot occur, so the energy of the core can only travel through it by radiative diffusion. Whereas a photon would take about 2 seconds to cross this layer if there was vacuum inside, the photons are absorbed and re-emitted so many times that they need around 170,000 years to pass through the radiative zone (Mitalas and Sills, 1992).

- **Convection zone:** It extends from the radiative zone to near the surface. The density of the plasma here is too low to allow radiative diffusion, but low enough to allow the outward energy transport through convection: at the base of this layer, the plasma is heated rapidly since it reaches temperatures of around $2 \cdot 10^6$ °C, so it rises rapidly to the top (found at between 4500-6000 °C) through buoyancy. This movement creates a turbulent convection pattern.

The boundary between the radiative and convective zones is called the *tachocline*. Below it, the Sun rotates like a solid rigid body. Above it, it has different rotation speeds depending on the latitude. As viewed from Earth, the solar equator makes a complete rotation in 26.24 days, while the poles take 36 or 37 days to do so (Priest, 2013). This phenomenon is known as *differential rotation*. The change in rotation speed across the tachocline is so abrupt, that it is considered to be an important source of the shearing forces that play a fundamental role in the creation of much of the Sun's large-scale magnetic field.

Above the aforementioned layers, there is the solar atmosphere, which can be observed because photons can escape directly into space. It consists of multiple regions:

- **Photosphere:** This is the visible surface of the Sun and emits most of the solar radiation, since the energy generated in the core can finally move freely through space. It is a layer with an extremely small thickness (only several hundred kilometers), and a temperature between 4500-6000 °C. A phenomenon known as *granulation* caused by convective currents below the photosphere is manifested here in the form of *granules* or *Bénard cells* (see Figure 1.3). Each

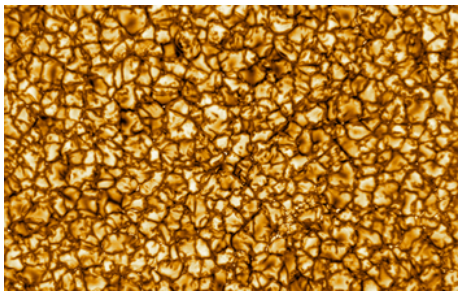

Figure 1.3: Close-up view of the solar surface provided by NSF's Inouye Solar Telescope covering a total area of $36,500 \times 36,500$ km. It shows the pattern of cell-like structures called granules that are the signature of the violent convective motions that transport heat to the Sun's surface. Retrieved from `https://www.nsf.gov/news/news_summ.jsp?cntn_id=299908&linkId=81408478`.

granule is roughly 1000 km wide and lasts for about 20 minutes. Plasma rises in the center of the cell where it is hotter, cools down through the release of energy into space, and then flows to the sides of the granule and sinks down into the photosphere, making the borders appear darker.

- **Chromosphere:** It is found above the photosphere, with a thickness of merely 1000-2000 km and a temperature rising from 4500-6000 °C at the bottom to about 25000 °C on top of it. Here, the plasma density drops dramatically, being only 10^{-4} times that of the photosphere. Right above the chromosphere and separating it from the corona, there is a thin and irregular layer called the *solar transition region*. Its most striking feature is the incredible increase in temperature to nearly a million degrees Celsius that occurs across it. The importance of the transition region relies on the fact that it represents a spatial boundary of two different behaviors of solar plasma: below, gas pressure and fluid dynamics govern the plasma, while above it, magnetic forces dominate its motion and shape.

- **Corona:** It is the Sun's outer atmosphere. Its average temperature is of $1 \cdot 10^6 - 2 \cdot 10^6$ °C and can go up to $20 \cdot 10^6$ °C, although the reason why the Sun's corona is so much hotter than its surface is still an unsolved problem in physics. Its density is about 10^{-12} times the density of the photosphere. This layer extends millions of kilometers away from the Sun, and can be observed during solar eclipses or using *coronagraphs* (devices that block out most part of the direct light coming from the Sun, such that only the relatively faint corona remains visible).

The region of influence of the Sun in space extends much further than the solar corona or even the Solar System. It is known as the *heliosphere* (see Figure 1.4), and it actually forms a giant bubble around the Sun that continuously receives plasma released by it, known as the *solar wind*. The solar wind was discovered by the astrophysicist Eugene Parker in 1958, and it is formed by streams of plasma that possess enough energy to escape the Sun's gravitational field. It reaches speeds of 300-800 km/s, but the acceleration mechanism is still unknown. Moreover, it drags with it the solar magnetic field from the corona, filling the Solar System with the so-called *heliospheric magnetic field* (HMF) (the coupling between plasma and magnetic field will be addressed in section 2.2). Due to the rotation of the Sun, the HMF arranges itself into a pattern similar to a spiral (the *Parker spiral*), and more complexity is added due to the variations of the solar wind in temperature, speed and density over solar latitude, longitude, and time.

1.1.3 Solar dynamo theory and the occurrence of eruptions

Nowadays, very detailed images of the turbulent surface and the different layers of the Sun are available thanks to missions such as the SOlar and Heliospheric Observatory (SOHO) or the Solar TErrestrial RElations Observatory (STEREO). They allow us to see the solar surface and the different atmospheric layers through extreme ultraviolet imagers (EUVI) that select and amplify

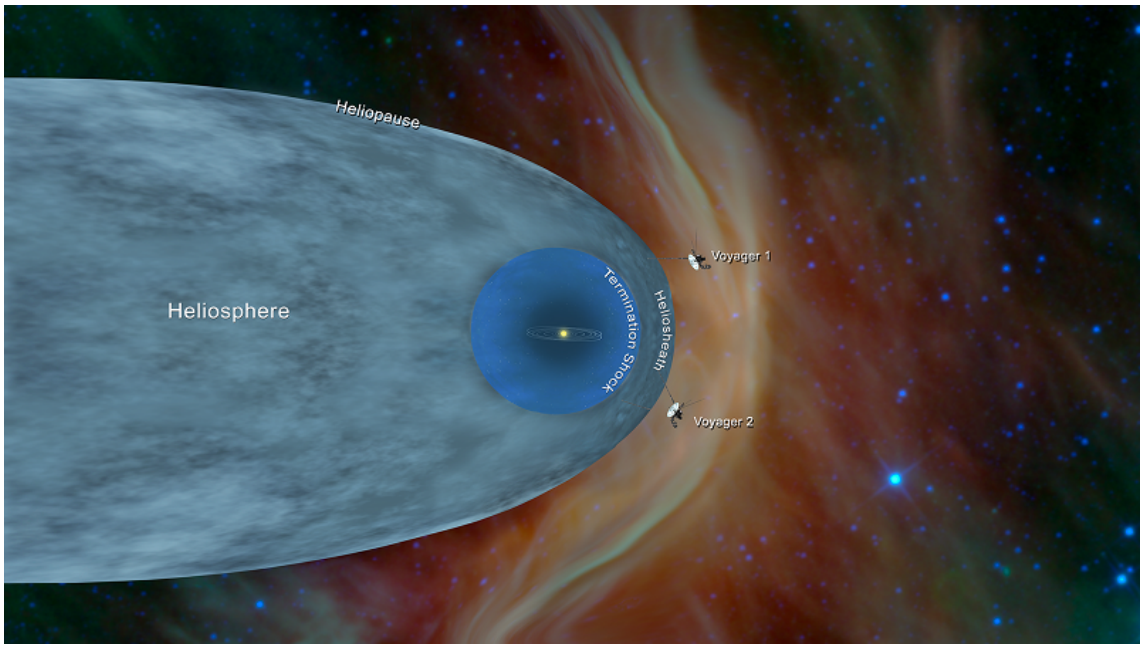

Figure 1.4: Diagram of what is currently believed to be the structure of the heliosphere. The solar wind travels through space without impediments far beyond Pluto until the *termination shock*. There, the outside pressure of the interstellar medium slows it down abruptly and the solar wind becomes turbulent and compressed in a broad transitional region known as the *heliosheath*. The *heliopause* is the outer boundary of the heliosphere where the solar and interstellar wind are in equilibrium. The figure also shows the twin Voyager 1 and 2 spacecraft. They were launched in 1977 and are still providing invaluable scientific data, since they are the first and only probes that have reached the interstellar medium until today. Retrieved from `https://www.jpl.nasa.gov/edu/news/2018/12/18/then-there-were-two-voyager-2-reaches-interstellar-space/`.

particular wavelengths of ultraviolet light emitted by the Sun. The X-ray emission spectra of the Sun has also been observed with missions like the Nuclear Spectroscopic Telescope ARray (NuSTAR). An example of these images can be seen in Figure 1.5. The results reveal very turbulent and constantly changing phenomena: magnetic loops forming, twisting and decaying, brightness variations, plasma flows, eruptions, among others.

Understanding these processes and their consequences requires the study of what the main drivers of the solar magnetic system are and how its magnetic fields are originated. This is one of the central problems in solar physics. *Solar dynamo theory* is currently the most promising theory for the solar behavior (see section 2.2.2), but it still requires further development to be complete.

The Sun is made up of hot plasma, a fundamental state of matter that consists of a gas of ions and free electrons, such that long-range electrostatic interactions and the effect of magnetic fields become relevant. The movement of charged particles is known to create magnetic fields which in turn affect the way the particles move. The area of physics that studies these phenomena is called *magnetohydrodynamics* (MHD), and will be described in Chapter 2.

Solar dynamo theory asserts that these complicated nonlinear interactions between the magnetic fields and the solar plasma, together with the energy released by nuclear fusion reactions at the core of the Sun, generate and maintain its magnetic fields. The plasma material moves along the magnetic field because it is actually frozen into it in most cases (the well-known *Alfvén's theorem*, see section 2.2). Therefore, solar magnetic fields are observable to EUV or X-ray imagers thanks to the fact that the plasma that moves along with them emits light at different wavelengths, as shown in Figure 1.5.

The Sun varies periodically with time, in a cycle that lasts for approximately 11 years. In the beginning of this period, sunspot groups are formed first at high latitudes symmetrically around the equator (40-50°) and then slowly propagate towards it, reaching after some years the phase of

maximum occurrence of the sunspots at latitudes below 25°: the *maximum* of the cycle. At this moment, the magnetic field adopts a very complex shape with magnetic structures that become increasingly twisted and entangled, and continuously interact with emerging fields. When the energy required to sustain these complex structures grows too large, the Sun removes parts of them through eruptions that convert the magnetic energy into gravitational and kinetic energy, which can cause the ejection of large plasma structures into the interplanetary space (e.g. coronal mass ejections). Every eruption contributes to decrease the complexity of the solar magnetic fields while the sunspot groups gradually approach the equator. This goes on until the Sun reaches its simplest state and the sunspots disappear almost completely: the *minimum* of the cycle.

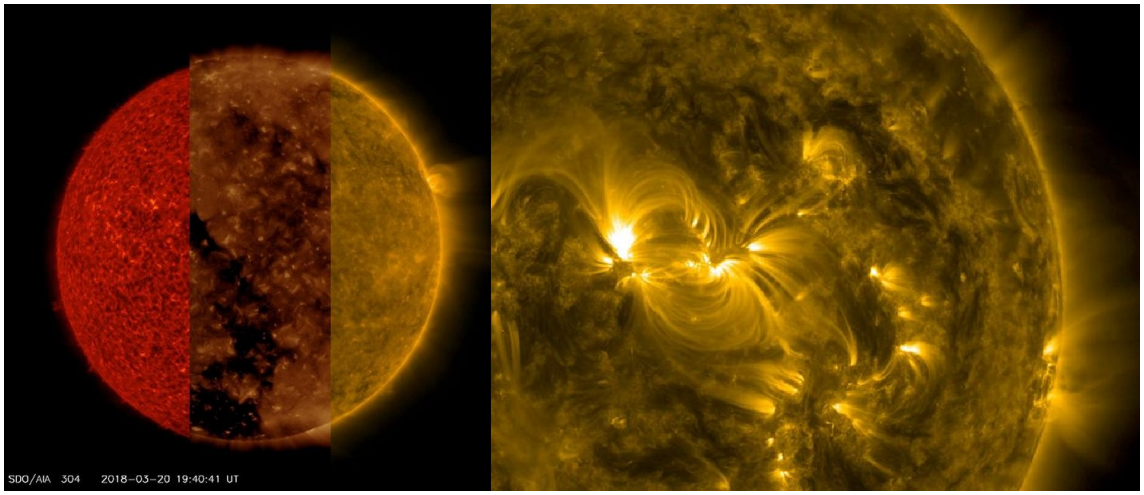

Figure 1.5: Left: extreme ultraviolet images for three different wavelengths (from left to right: 304 Å, 193 Å, 171 Å) taken by NASA's Solar Dynamics Observatory (SDO). It illustrates how each wavelength allows the visualization of only specific solar features. Right: close-up of the complex magnetic structures of an active region during July 15-18, 2016, which appear in the 171 Å EUV image taken by NASA's SDO. See further explanation in section 1.2.3. Retrieved from NASA Image and Video Library.

1.2 Coronal Mass Ejections (CMEs) and Space Weather

The build-up of energy that is produced in the Sun due to the constant motion and twisting of its magnetic field, creates very complex structures which can require an energy too high to be sustained. If that is the case, the Sun releases the excess energy in two possible ways: the usual steady flow of light that is essential for living organisms on Earth, but also in more violent and explosive forms, such as flares, coronal mass ejections (CMEs) and eruptive prominences.

Coronal mass ejections (CMEs) consist of large structures containing plasma and magnetic fields that are expelled from the Sun into the heliosphere. From a scientific point of view, they are particularly interesting in order to understand the solar magnetic field and activity. Moreover, being responsible for the most extreme space weather events, they can have severe impact in our technological systems. The aim of space weather is therefore being able to foretell sufficiently far in advance the eruption and evolution of CMEs and other phenomena, allowing us to prevent or mitigate their potentially damaging effects on our society.

1.2.1 Space weather and the impact of CMEs on Earth

The first relation between geomagnetic storms and solar activity was established in 1859. In that year, the most intense magnetic storm ever recorded on Earth occurred only 18 hours after Richard Carrington made the first observation of a *solar flare* (a sudden burst of increased brightness on the Sun), causing the disruption of telegraph systems across Europe and North America, and aurorae at low-latitude regions like the Caribbean (Howard, 2011).

In fact, as society becomes more reliant on ever more advanced technology systems powered by electricity, its vulnerability to extreme space weather events (generally caused by large and fast CMEs hitting Earth with southward magnetic field) increases. They could have potentially dire consequences for power grids, GPS, aviation and satellites, as well as endanger high-altitude aircraft fliers and astronauts due to increased radiation exposure, or cause the early corrosion of oil and gas metal pipelines. These effects, in turn, would cause the failure of other interdependent infrastructures (e.g. potable water distribution, preservation of perishable foods and medications, heat/air conditioning, sewage disposal, transportation, phone services, operational and communication systems in spacecraft). An example of the severe effects of past geomagnetic storms can be found in a report of a CME hitting Earth on March 1989 Allen et al. (1989). Some studies estimate that future extreme space weather events could cost $1-2 trillion in the first year and take 4-10 years to fully recover (by comparison, hurricane Katrina costed $81-125 billion, and the Northeast blackout of 2003, $4-10 billion) (National Research Council, 2008; Oughton et al., 2017).

The predictability of geomagnetic storms caused by CMEs has therefore recently become one of the primary goals of space weather research. However, the limited information about their 3D magnetic topology provided by measurements, and the insufficient understanding of the evolutionary processes that CMEs may undergo, hinder the development of accurate prediction models.

1.2.2 Overview of CMEs basic features

Coronal mass ejections (CMEs) are large eruptions of magnetized plasma from the solar corona into the heliosphere that are observed as an increase of brightness in the solar telescopes' field of view (see two examples in Figure 1.6). They reach typical velocities of 400-1000 km/s. An Earthward-directed CME would take 2 to 5 days to reach Earth, but the largest CMEs can accelerate particles to about a tenth of the speed of light, which implies that they only need 80 minutes to reach Earth. They have a mass of about $10^{11} - 10^{12}$ kg and typically span several tens of degrees of heliographic latitude (measured from the solar equator to the poles), while the Earth has a mass of around $6 \cdot 10^{24}$ kg and is $(5 \cdot 10^{-3})^{\circ}$ in heliographic latitude. Most of the ejected plasma comes from the low corona, although cooler, denser material is sometimes involved, which is probably originated at the chromosphere or photosphere (Priest, 2013).

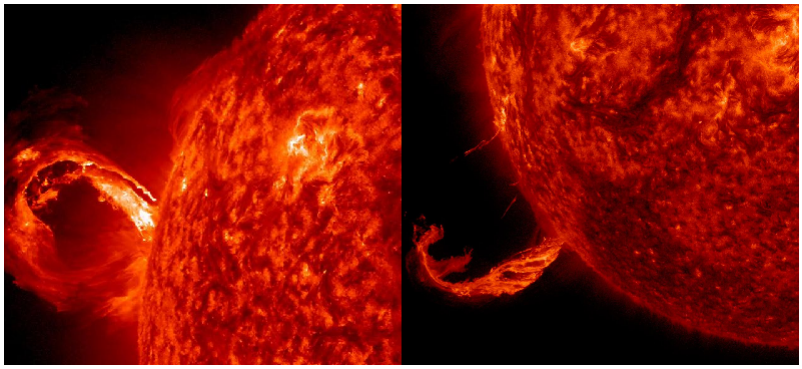

Figure 1.6: Extreme ultraviolet images of erupting CMEs by the Solar Dynamics Observatory (SDO). The pictures were taken on May 1, 2013 (left) and February 24, 2015 (right). Retrieved from NASA Image and Video Library.

The occurrence rate of CMEs depends on the solar cycle, and one can observe between 0.5 per day at solar minimum to 6 per day at solar maximum. Their spatial distribution is clustered about the equator at solar minimum but is much broader at solar maximum. When they erupt, they cause major modifications in the large-scale magnetic structure of the corona (Priest, 2013).

Interplanetary coronal mass ejections (ICMEs) are what CMEs are called when they reach distances of more than 50 solar radii away from the Sun. They are the heliospheric counterpart of CMEs, and possess similar magnetic structure and mass but smaller velocities. When they travel through the interplanetary medium at supersonic speeds, they cause *shock waves* in front of them.

1.2.3 Detection of CMEs and ICMEs

Remote sensing observations

One way to detect CMEs consists in observing them in the images taken by telescopes. Researchers usually refer to these measurements as *remote sensing observations*. There are many different types of them, and can be classified in terms of the wavelengths they detect, for example.

Coronagraphs and heliospheric imagers provide observations of the photospheric white-light that is scattered by the free electrons of the coronal plasma. The invention of the *coronagraph* by Bernard Lyot in 1931 produced the first coronal white-light measurements by blocking out most of the unwanted solar radiation, such that only the corona remained visible. However, the sensitivity of the first devices needed to be improved in order to detect coronal eruptions, since the light from the corona is relatively faint in comparison with the emission from other layers. It was not until 1973 that the astronomer Richard Tousey observed the first CME.

One of the main challenges posed by white-light images of the corona is that one can only observe the projection of the CMEs into the sky plane. Therefore, determining the shape, the trajectory or the characteristics of the dynamic evolution of CMEs is usually a difficult task. It is often helpful to consider multipoint observation measurements, since the real situation can be reconstructed better if two or more different points of view are available. Otherwise, it is useful to look at the solar disk for signatures of eruptions (e.g. erupting prominences, solar flares or disappearing filaments) to have an idea of the initial direction of propagation. This is where extreme ultraviolet (EUV) or X-ray observations come into play.

EUV measurements provide images of the solar disk features. They filter the light coming from the Sun and select only one wavelength for the visualization. EUV measurements have obtained invaluable information to the study of CME initiation theories, the early stage development of CMEs, as well as the detailed examination of solar surface features. Moreover, X-ray images indicate the occurrence of solar flares, which are often associated to CME eruptions.

Images as the ones in Figure 1.5 and 1.7 can be obtained every 12 seconds for more than 10 different extreme ultraviolet wavelengths, providing an almost constant and extensive source of information about the Sun. The bright areas correspond to *active regions*, where the magnetic field is especially strong and can give rise to solar eruptions. The dark areas, on the other hand, correspond to *coronal holes*, where the Sun's magnetic field opens out into the solar system, allowing plasma from the inside to escape. Long thin bright filaments are *prominences*, which can give birth to CMEs at some point.

In situ measurements

Measurements of physical plasma parameters that are taken directly on the ICME while it crosses the instruments of a spacecraft, such as magnetic field and solar wind density or velocity, are known as *in situ* measurements. The detection of the first CMEs in the early 1970s coronagraphs motivated the search for their signatures in *in situ* spacecraft data, and more than 20,000 CME events have been registered to this day. Burlaga et al. (1981) first identified structures containing organized magnetic fields and showing the smooth rotation of at least one of their magnetic components. He named them *magnetic clouds* (MCs) and their connection to CMEs was soon established.

The *in situ* signatures that identify MCs are: the increase in the average magnetic field strength, the monotonic rotation of the magnetic field direction through a large angle, a low proton temperature, and a low ratio of the plasma to magnetic pressure, i.e. $\beta_{proton} \ll 1$, such that the magnetic forces dominate the structure. These signatures actually correspond to the behavior of ideal *magnetic flux ropes* (MFRs), which are defined as collections of field lines wrapping around an internal main axis in a twisting way. They will be discussed in much more detail in Chapter 3, since they constitute the basis of many of the reconstruction techniques that have been developed for CMEs.

The main inconvenience about *in situ* measurements is the fact that they only measure a single 1D track through the ICMEs. The information is thus incomplete, and so it is necessary to make

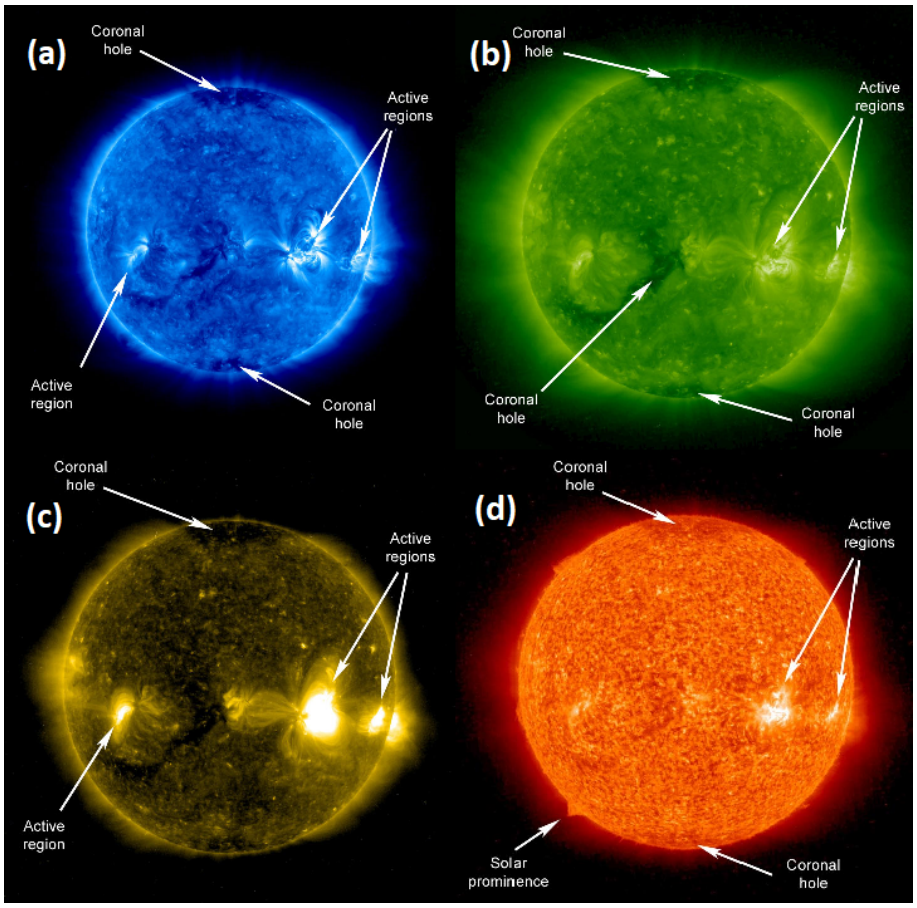

Figure 1.7: Images taken by STEREO A SECCHI/EUVI telescope on June 10, 2007. (a) The Sun at 171 Å. Light mainly emitted by Fe IX and X (iron ionized 8-9 times) at $1.0 \cdot 10^6$ K. (b) The Sun at 195 Å. Light mainly emitted by Fe XII (iron ionized 11 times) at $1.4 \cdot 10^6$ K. (c) The sun at 284 Å. Light mainly emitted by Fe XV (iron ionized 14 times) at $2.2 \cdot 10^6$ K. (d) The Sun at 304 Å. Light mainly emitted by He II (helium ionized once) at 60,000-80,000 K. Retrieved from STEREO Mission Official Website.

strong assumptions about their geometry in order to reconstruct the global 3D picture of the whole structures. Multipoint *in situ* measurements of a single event, when they are available, usually help address this issue.

It has been found that only around a third of the CMEs detected in the solar wind exhibit clear MC signatures. The percentage varies depending on the solar activity level, being significantly higher during solar minima. However, is this small fraction due to the fact that not all ICMEs are MCs? Or is it rather due to the limitations of 1D *in situ* measurements (e.g. crossing the MC far from the axis), or to other phenomena that we do not understand yet, like the interactions between consecutive CMEs and the solar wind, the expansion of the structures, or the occurrence of rotations and deflections? These are open questions that will be addressed in the present work.

1.2.4 Spacecraft for the study of CMEs

There are currently a great number of missions that have provided a lot of valuable information for the study of CMEs. This section gives an overview of the main characteristics of the spacecraft that will be mentioned through this study.

Parker Solar Probe

Parker Solar Prober (PSP) is a NASA mission that was launched on August 12, 2018, from Cape Canaveral Air Force Station (Florida). It is the first spacecraft to fly into the low solar corona, getting as close as 9.86 solar radii (or $6.86 \cdot 10^6$ km) from the center of the Sun, well within Venus' orbit and seven times closer to it than any other spacecraft until now. This mission provides a unique opportunity to study the solar magnetic field and plasma structures and dynamics, as well as the heating mechanisms of the corona and the acceleration of energetic particles.

The spacecraft uses Venus' gravity to get gradually closer to the Sun during a period that will last for over seven years. It has a dual system of photovoltaic arrays as the primary power source, and is prepared to withstand temperatures as high as 1400 °C. PSP has a set of *in situ* and imaging instruments that will hopefully contribute to advance the current understanding of the corona and the solar wind. The instruments that will be used in the analysis of a CME event in section 3.4 can be visualized in Figure 1.8 and are the following:

- The SWEAP, or Solar Wind Electrons Alphas and Protons, contains two complementary instruments that count and measure properties like the velocity, density, and temperature, of electrons, protons and helium ions that constitute the solar wind. The two instruments are: the Solar Probe Cup, or SPC, and the Solar Probe Analyzers, or SPAN. In this work, *in situ* data of the SPC instrument of the solar wind temperature, density and velocity, will be used.
- The FIELDS instrument suite studies the magnitude and shape of electric and magnetic fields in the Sun's atmosphere. We will use its magnetic field measurements to study and reconstruct the CME.

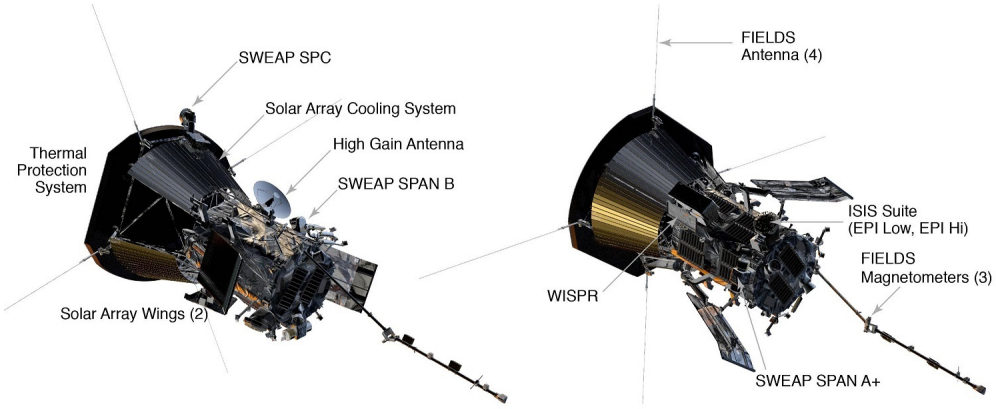

Figure 1.8: Close-up of the PSP spacecraft and its instrument suites. Retrieved from NASA Image and Video Library.

Other missions

- STEREO was launched on October 25, 2006, from Cape Canaveral Air Force Station. It consisted of two nearly identical or so-called *twin spacecraft*, STEREO A (Ahead) and STEREO B (Behind), whose aim was to provide the first stereoscopic measurements of solar phenomena like CMEs. The STEREO mission was designed to last for only two years, but STEREO

A is still operating today and STEREO B was lost on October 1, 2014, after a long period of 8 years since the launch. The most relevant instruments for us will be SECCHI COR1 and COR2, two coronagraphs that provide white-light images of the plane of sky from 1.4 to 4.0 solar radii and from 2.5 to 15.6 solar radii, respectively (see EUV images taken by STEREO in Figure 1.5 and 1.7, and COR2 image in Figure 3.6).

- The SOlar and Heliospheric Observatory (SOHO) is a spacecraft built jointly by the European Space Agency (ESA) and NASA, which was built to last for two years, but is still operating today after over 25 years in space. It is located very close to the Earth and maintains its relative position to the Earth and the Sun. Its main goal is the study of the solar atmosphere with remote sensing observations, as well as the interior structure of the Sun through helioseismology. The instruments that will provide measurements for the reconstruction in section 3.4 are LASCO C2 and C3 white-light coronagraphs, that generate images of the plane of sky from 2 to 7 solar radii and from 3.7 to 30 solar radii, respectively.

- Solar Orbiter is a mission developed by the ESA and NASA that has been launched very recently, on February 10, 2020. In principle, the mission will last 7 years and will address the main challenges about the understanding of the solar wind, the Sun's magnetic fields, and CMEs. Moreover, it will go out of the ecliptic plane to reach latitudes up to 33°, providing images of regions closer to the solar poles than ever before. The design of Solar Orbiter trajectory and its complete set of instruments (see Figure 1.9) will provide very valuable information to address many scientific questions, such as the twist and kink instability of magnetic flux ropes (MFRs) that are analyzed in Chapter 4.

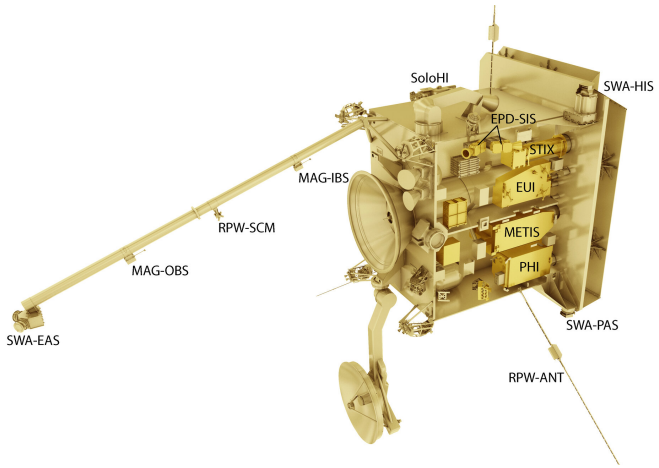

Figure 1.9: Solar Orbiter spacecraft and its instrument suites. Retrieved from `https://www.esa.int/Space_in_Member_States/Spain/Los_instrumentos_de_Solar_Orbiter`.

2 . MHD in space physics

Plasmas are ubiquitous in the Universe and play an important role in almost any phenomenon occurring in the interplanetary, interstellar and intergalactic spaces. They are profoundly affected by magnetic fields and can adopt many different forms and behaviors. Magnetohydrodynamics (MHD) studies the physics of plasmas and their interaction with magnetic fields. This chapter will provide an overview of plasmas and MHD fundamentals, which will be essential in order to understand how the main objects of this study, coronal mass ejections (CMEs), are modeled and reconstructed, as well as the instabilities they can develop.

2.1 Plasma: the fourth state of matter

2.1.1 Space and terrestrial plasmas

Plasma represents over 99% of the matter that is found in the Universe (Kallenrode, 2004), although the existence of dark matter and its unknown properties could challenge this hypothesis. There is an endless list of space plasmas (e.g. galactic jets, supernova bubbles, accretion disks, gallactic and stellar winds, stellar coronas, sunspots, the heliosphere...) and of the many important phenomena that they cause (e.g. cosmic rays, stellar flares, interstellar and interplanetary shock waves, magnetospheric storms, CMEs...).

It is actually not necessary to go so far into the Universe in order to encounter plasmas, since the Earth and its surroundings contain plenty of examples of them. We can find plasmas in our everyday lives, for example in the flash of a lightning bolt, in the aurorae of polar regions, inside fluorescent tubes or neon signs, in fusion plasma research, etc. If we go a little bit further above of us, to the upper part of the atmosphere, there is a plasma layer called *ionosphere* (located from 60 to 1000 km of altitude) that reflects radio waves, therefore allowing the long-distance propagation of radio signals. In fact, the ionosphere forms the inner edge of the Earth's *magnetosphere*, i.e. the region of space that is dominated by Earth's magnetic field. It is mainly populated by plasma too, and acts as a barrier to the solar wind (Borovsky and Valdivia, 2018).

It is worth mentioning here that interplanetary coronal mass ejections (ICMEs), one of the central subjects of this thesis, can severely modify the magnetosphere when they hit it carrying a southward magnetic field, since the process of *magnetic reconnection* (the rearrangement of the field topology to reduce the energy of a system; see an example in Figure 2.4) takes place between the ICME and Earth's polar magnetic field lines. Therefore, the energetic particles of the solar wind plasma are able to enter the terrestrial polar regions through the field lines that have become directly connected to the Sun (see Figure 2.1 (left)). These particles excite the molecules in the Earth's upper atmosphere and make them emit photons when they return to the original state, creating a natural light display in the Earth's sky of high-latitude regions, which are called *aurorae*. Other planets like Jupiter also have their own magnetosphere and aurorae (e.g. see Fig. 2.1 (right)).

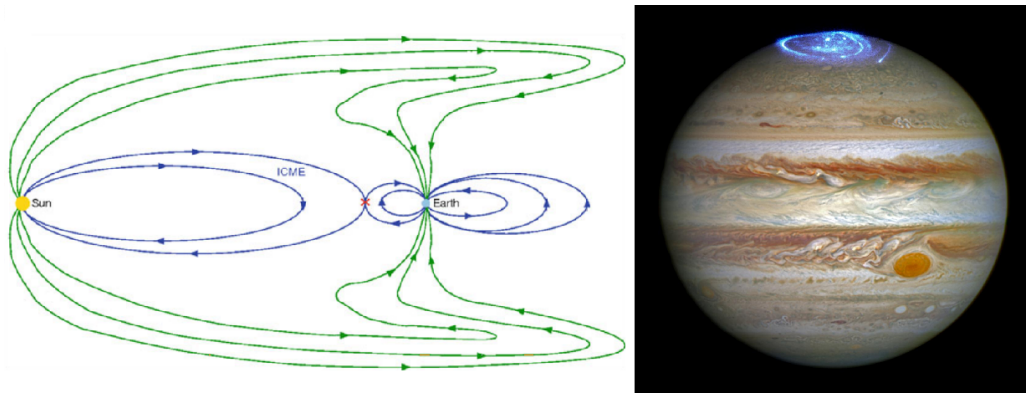

Figure 2.1: Left: Scheme of magnetic reconnection between an ICME and Earth's magnetosphere. The reconnected lines passing through the Sun and the Earth are green, while the field lines that are connected with only one of them appear in blue. Retrieved from Howard (2011). Right: Picture of Jupiter's aurora taken by NASA/ESA Hubble Space Telescope. Retrieved from NASA Image and Video Library.

2.1.2 Definition and basic properties of plasmas

The term 'plasma' was first used to describe an ionized gas in 1927 by the Nobel prize winning chemist Irving Langmuir, since the way it carried electrons and ions reminded him of the way blood plasma carries red and white corpuscles. However, this description of the fourth state of matter needs to be more accurate, since gases always have some small degree of ionization but not all of them behave as plasmas. As stated in Chen (1984), a *plasma* can be defined as a quasineutral gas of charged and neutral particles which exhibit collective behavior.

By *collective behavior*, we are referring to the situation in which the motion of one particle depends not only on its local environment, but also on the state of the plasma in remote regions. This does not occur in ordinary neutral gases, whose molecules move undisturbed unless they collide with another one. The collisions are thus the only mechanism that controls the particles' motion and are responsible for transmitting forces and perturbations around the gas. However, the situation becomes completely different when the gas contains charged particles. Their motion can give rise to local concentrations of positive or negative charge, which in turn generate currents, electric and magnetic fields, so a particle can now affect others that are far away through the action of these electromagnetic fields. In practice, collisions and long-range electromagnetic interactions happen simultaneously. An ionized gas will qualify as a plasma only if collisions do not occur very frequently, such that the behavior is dominated by the electromagnetic forces rather than the typical hydrodynamic ones.

It just remains to specify the meaning of *quasineutrality*. Plasmas are characterized by the fact that they are able to shield out electric potentials, since their free positive and negative charges can form a cloud around the newly introduced charges to cancel them out (see Figure 2.2). In a cold plasma with no thermal motion at all, the shielding would be perfect because the particles would be able to move freely. However, as the temperature is finite in real situations, the ones that are closer to the "edge" of the cloud have enough thermal energy as to escape from the electromagnetic forces that tried to keep them inside. The parameter known as *Debye length* λ_D gives a measure of the scale over which mobile charge carriers in a plasma are able to shield out electric fields, without being dominated by their thermal energy.

Any local concentration of charge or external potential will be shielded out in a distance λ_D. Therefore, if $\lambda_D \ll L$, where L is the characteristic dimension of the system, then the bulk of the plasma can still be considered to be 'almost neutral' or, equivalently, *quasineutral*. While λ_D is of the order of 10^{-4} m in tokamak plasmas (with an electron density of $N_e \sim 10^{20}$ m^{-3}), it can reach macroscopic values in space plasmas with low electron density N_e, such as the solar wind ($N_e \sim 10^6$ m^{-3}, $\lambda_D \sim 10$ m), the magnetosphere ($N_e \sim 10^7$ m^{-3}, $\lambda_D \sim 10^2$ m) or the intergalactic medium ($N_e \sim 1$ m^{-3}, $\lambda_D \sim 10^5$ m) (Chen, 1984).

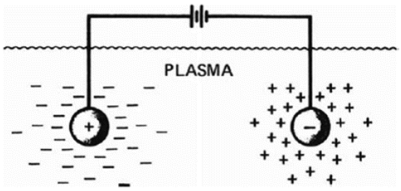

Figure 2.2: Schematic representation of the Debye shielding phenomenon. Retrieved from Chen (1984).

2.2 Fundamentals of magnetohydrodynamics (MHD)

The dynamics and behavior of electrically conducting fluids are studied by MHD, which couples the Navier-Stokes equations for fluid dynamics and Maxwell's equations for electromagnetism, in order to account for the mutual interaction between the movement of the particles and the electromagnetic fields of the system. The fluids under study by MHD are mainly plasmas, liquid metals and strong electrolytes.

During the 19th century, there were physicists who made a few isolated experiments that already addressed some of the concepts behind MHD. However, there was still little incentive by the practical and scientific possibilities offered by it. It was not until astrophysicists realized the ubiquitous presence of plasmas and magnetic fields throughout the Universe in the 1930s or early 1940s that the study of MHD began in earnest. Indeed, for example, Larmor had already hypothesized in 1919 that the Earth's magnetic field was generated due to the liquid-metal nature of its core. The physicist Hannes Alfvén was the first to use the term 'magnetohydrodynamics' in 1942, when he discovered the *Alfvén wave* (a phenomenon peculiar to plasmas in which ions can transmit transverse inertial waves as if they were strings being plucked).

Nowadays, there are three major fields of application of MHD: the study of space plasmas and magnetic fields, the controlled thermonuclear fusion of plasmas (with a special focus on their stability for magnetic confinement), and the metallurgical industry (where magnetic fields are routinely used to stir, heat, pump and levitate liquid metals).

An intuitive picture of the physical effects involved in the mutual interaction of a magnetic field and the velocity of a conducting fluid can be given as follows: when the fluid moves in the presence of a magnetic field, an electromotive force develops in accordance with Faraday's law of induction, generating electrical currents proportional to the conductivity σ of the fluid. The induced currents, in turn, give rise to an induced magnetic field in accordance with Ampère's law, which adds to the original magnetic field in such a way that the fluid seems to drag the magnetic field lines along with it. At the same time, the combined magnetic field interacts with the induced current to give rise to a Lorentz force on the conductor, which generally tends to inhibit the relative movement of the fluid and the magnetic field (Davidson, 2001).

The tendency of these physical mechanisms to couple the magnetic field and the motion of the fluid, generally reducing the relative movement between them, is actually the hallmark of MHD. In the limit of ideal MHD (where the fluid is considered to be a perfect conductor), *Alfvén's theorem* states that the magnetic flux passing through any arbitrary open surface area moving with the plasma is constant. This implies that the flux is conserved globally and locally, and that that magnetic field lines move as if they were 'frozen into' the fluid (see Figure 2.3).

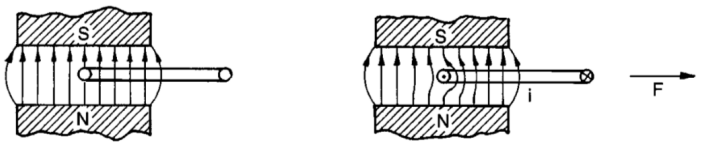

Figure 2.3: Interaction between a magnetic field and a perfectly conducting moving wire loop. Currents and fields are generated such that the wire appears to 'drag' the field lines. Retrieved from Davidson (2001).

2.2.1 The advection-diffusion equation of the magnetic field

MHD kinematics studies one half of the coupling between the magnetic field $\mathbf{B}$ and the velocity $\mathbf{v}$ of the system, by only considering the influence of $\mathbf{v}$ on $\mathbf{B}$, and taking $\mathbf{v}$ to be prescribed, without worrying about its origin or the reaction Lorentz forces on the fluid (so Navier-Stokes equations are not taken into consideration yet).

In this respect, the *induction* (or *advection-diffusion*) *equation* for $\mathbf{B}$ is a key equation in MHD since it dictates the temporal and spatial evolution of $\mathbf{B}$ for some given $\mathbf{v}$. Let $\mathbf{E}$ be the electric field, $\mathbf{j}$ the current density, σ the conductivity of the fluid and μ_0 the vacuum permeability. The starting point is to combine Faraday's law ($\nabla \times \mathbf{E} = -\frac{\partial \mathbf{B}}{\partial t}$) with Ohm's law ($\mathbf{j} = \sigma(\mathbf{E} + \mathbf{v} \times \mathbf{B})$) in

$$\frac{\partial \mathbf{B}}{\partial t} = -\nabla \times \mathbf{E} = -\nabla \times \left(\frac{\mathbf{j}}{\sigma} - \mathbf{v} \times \mathbf{B} \right) = \nabla \times (\mathbf{v} \times \mathbf{B}) - \frac{1}{\sigma} \nabla \times \mathbf{j}.$$

The second term can be rewritten using Ampère's law ($\nabla \times \mathbf{B} = \mu_0 \mathbf{j}$) and the vector identity $\nabla \times (\nabla \times \mathbf{B}) = \nabla(\nabla \cdot \mathbf{B}) - \nabla^2 \mathbf{B}$, such that Gauss' law for magnetism ($\nabla \cdot \mathbf{B} = 0$) reduces it to $\nabla \times (\nabla \times \mathbf{B}) = -\nabla^2 \mathbf{B}$. The previous expression becomes

$$\frac{\partial \mathbf{B}}{\partial t} = \nabla \times (\mathbf{v} \times \mathbf{B}) + \lambda \nabla^2 \mathbf{B}, \tag{2.1}$$

where $\lambda = 1/(\mu_0 \sigma)$ is the so-called *magnetic diffusivity*. Eq. (2.1) is actually the induction equation for $\mathbf{B}$. The first term corresponds to the *advection* or motion of the magnetic field caused by the fluid, and the second one to diffusion through the medium.

The *magnetic Reynolds number* is an important dimensionless parameter since it measures the strength of the coupling between the magnetic field and the fluid flow. It is defined as

$$R_m = \frac{lv}{\lambda} = \mu_0 \sigma l v, \tag{2.2}$$

where l and v are the typical length and velocity scales of the fluid, respectively. Indeed, R_m gives a tentative value for the magnitude of the ratio of the advective to diffusive terms in Eq. (2.1), since $\nabla \times (\mathbf{v} \times \mathbf{B}) \sim B_0 v / l$ and $\lambda \nabla^2 \mathbf{B} \sim \lambda B_0 / l^2$, and dividing them results in Eq. (2.2). Consequently, the behavior of the magnetic field depends crucially on the magnitude of R_m:

- **Diffusive limit** ($R_m \ll 1$): the induction equation reduces to a simple diffusion equation,

  $$\frac{\partial \mathbf{B}}{\partial t} = \lambda \nabla^2 \mathbf{B}.$$

  In this limit, the velocity $\mathbf{v}$ has little influence on $\mathbf{B}$, and the magnetic field induced by the motion of the fluid is negligible. However, $\mathbf{B}$ can still severely modify $\mathbf{v}$ through the Lorentz force $\mathbf{j} \times \mathbf{B}$ if the magnitude of the imposed magnetic field is strong enough. Laboratory liquid-metal MHD lies closer to this limit.

- **Ideal limit** ($R_m \gg 1$): the induction equation reduces to

  $$\frac{\partial \mathbf{B}}{\partial t} = \nabla \times (\mathbf{v} \times \mathbf{B}).$$

  Alfvén's theorem of the flux conservation, which was stated in the end of the previous section, is valid in this limit, and therefore the field lines behave as if they were frozen to the plasma, and move with it. In this regime, small disturbances can give rise to near-elastic inertial oscillations where the restoring force is provided by $\mathbf{B}$, known as *Alfvén waves*. This phenomenon has an important role in the propagation of energy and momentum of space plasmas, for example. The ideal limit is valid for many astrophysical plasmas, which usually posses R_m values over 10^8 due to their exceptionally large length scales, as well as for liquid-metal cores of planets like Earth ($R_m \sim 10^2$), or hot fusion laboratory plasmas ($R_m \sim 10^6 - 10^9$) (Zohm, 2015).

2.2.2 MHD applications: magnetic reconnection and dynamo theory

We have seen that Alfvén's theorem of flux conservation is only valid in the limit of ideal MHD, when the magnetic diffusivity λ of the system becomes completely negligible. Since any allowable physical motion of a fluid requires that the fluid elements remain adjacent to one another (such that they cannot break or tear into separate pieces) and the magnetic field is frozen into them, this implies that the magnetic field topology must be preserved in any physically allowed motion. Even if it would be energetically favorable for field lines to break and reconnect into other configurations at some point, they are not physically allowed to do so.

However, the introduction of even a very small value of λ can have dramatic effets on the behavior of the plasma and its stability. The topological constraint is removed, and the diffusion allows the field lines to reconnect, converting the excess magnetic energy to kinetic and thermal energy, and particle acceleration. This can give rise to very violent and explosive phenomena (see Figure 2.4). Magnetic reconnection is actually thought to be a key mechanism in the initiation of CMEs and solar flares, as well as the cause of solar geomagnetic storms by the reconnection of the magnetic field lines of CMEs and the Earth's magnetosphere (see Figure 2.1 (left)).

A common approach to study plasma stability is to use the ideal MHD limit, since the equations become significantly simpler, and astrophysical and laboratory fusion plasmas are usually close to it. However, it should be taken into account that the introduction of a very small diffusivity can dramatically affect the plasma stability and behavior through the phenomenon of magnetic reconnection. Instabilities in the presence of diffusivity are studied in resistive MHD but lie far beyond the scope of the present work.

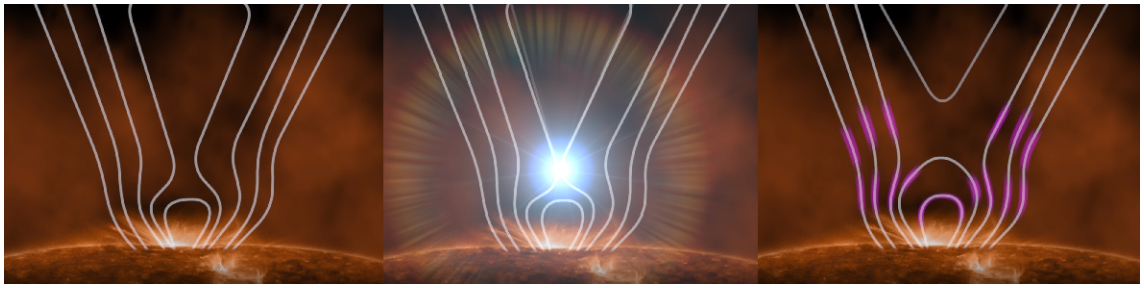

Figure 2.4: Schematic representation of the phenomenon of magnetic reconnection that usually occurs in solar magnetic fields. Retrieved from `https://svs.gsfc.nasa.gov/13422`.

Apart from magnetic reconnection, which is involved in many phenomena occurring in the Sun and the interplanetary space, there is a very interesting application of MHD that has given us great insight into the origin and evolution of magnetic fields throughout the Universe: *dynamo theory*.

The motivations for the development of dynamo theory came from different questions that had remained unanswered for a long time. The Earth's magnetic field has been shown to exist at around its present strength for $3 \cdot 10^9$ years, but it cannot account for its own magnetism by itself since conducting bodies with the same spatial dimensions can retain their magnetic fields only for around $2 \cdot 10^5$ years. The same conclusions are reached for other planets. So how do they maintain their magnetospheres if they cannot be a fossil relic of their birth?

In the case of stars similar to the Sun, the time that the magnetic field would require to dissipate, taking into account the turbulence of its plasma, would be of the order of a decade. Indeed, the magnetic field of the Sun follows an 11-year cycle, and at the end of each period it generates a new magnetic configuration with opposite polarity. A lot of stars similar to the Sun have analogous cycles. What is the mechanism behind the origin and the periodic variability of the Sun's magnetic field?

Dynamo theory provides a possible answer to these questions by proposing complex nonlinear interactions arising from the twisting, rotating and stretching motions of the highly conducting material they contain (i.e. plasma or liquid-metal cores) as the source that maintains and continuously intensifies the magnetic field (Proctor et al., 1995).

2.3 Studying MHD instabilities

In general, plasmas have a strong tendency to spontaneously change and develop rapid dynamics when they are slightly perturbed. These changes can completely destroy the original structure, since they usually involve large-scale motions at high speeds. Learning how to avoid MHD instabilities became crucial especially after the 1950s, when research on controlled thermonuclear fusion began in earnest and required the effective magnetic confinement of the plasma. In contrast to the extreme difficulty encountered in confining laboratory plasmas, it is surprising how a lot of solar plasma structures, like prominences or filaments, remain stable for long periods of time. At some point, however, they can also suddenly develop an instability and erupt towards the interplanetary space in the form of CMEs or stellar flares.

There is a very long list of instabilities of different nature that occur in plasmas. They can be internal or external (depending on whether they modify the plasma outer surface or not), pressure-driven or current-driven (according to the dominant driving source), etc. In the present work, we will focus on a particular type of current-driven instability, the *kink instability*, which is very common in space plasmas and acts upon magnetic configurations that are twisted around their axis, such that the axis itself becomes a helix (see Figure 2.5).

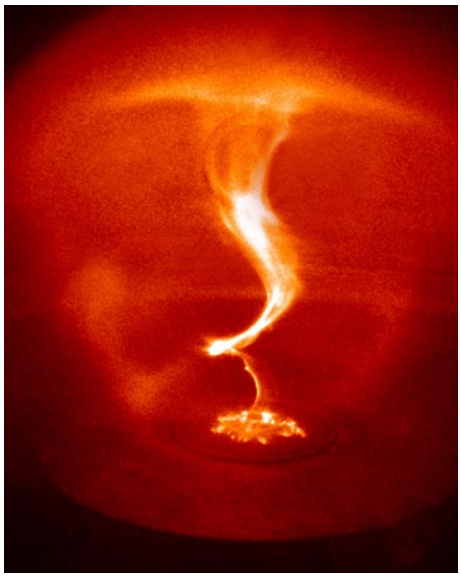

Figure 2.5: Photograph of the kink instability in a laboratory plasma column, where the helical shape of the axis can be clearly observed. Retrieved from Bellan et al. (2005).

2.3.1 Ideal MHD equations and equilibrium

Since MHD equations describe the motion of a conducting fluid interacting with a magnetic field, the first step towards obtaining them consists in combining Maxwell's equations with the governing equations of fluid mechanics. The set of ideal MHD equations will be presented here as in Goedbloed and Poedts (2010).

Let $\mathbf{E}(\mathbf{r},t)$ and $\mathbf{B}(\mathbf{r},t)$ denote the electric and magnetic fields, $\mathbf{j}(\mathbf{r},t)$ the current density, $\rho(\mathbf{r},t)$ the plasma density, $p(\mathbf{r},t)$ the pressure in the plasma, $\tau(\mathbf{r},t)$ the charge density, σ the conductivity of the fluid, γ the ratio of specific heats at constant pressure and volume, μ_0 the vacuum permeability,

ε_0 the vacuum permittivity, and c the speed of light. Maxwell's equations are

$$\nabla \times \mathbf{E} = -\frac{\partial \mathbf{B}}{\partial t} \qquad \text{(Faraday's law)} \tag{2.3}$$

$$\nabla \times \mathbf{B} = \mu_0 \mathbf{j} + \frac{1}{c^2}\frac{\partial \mathbf{E}}{\partial t} \qquad \text{(Ampère's law)} \tag{2.4}$$

$$\nabla \cdot \mathbf{E} = \frac{\tau}{\varepsilon_0} \qquad \text{(Gauss' law)} \tag{2.5}$$

$$\nabla \cdot \mathbf{B} = 0 \qquad \text{(Gauss' law for magnetism)} \tag{2.6}$$

and the additional relations for Ohm's law and charge conservation are

$$\mathbf{j} = \sigma(\mathbf{E} + \mathbf{v} \times \mathbf{B}) \qquad \text{(Ohm's law)} \tag{2.7}$$

$$\nabla \cdot \mathbf{j} = -\frac{\partial \tau}{\partial t} \qquad \text{(charge conservation)} \tag{2.8}$$

On the other hand, the equations for gas dynamics are

$$\frac{D\rho}{Dt} + \rho \nabla \cdot \mathbf{v} = 0 \qquad \text{(mass conservation)} \tag{2.9}$$

$$\frac{Dp}{Dt} + \gamma p \nabla \cdot \mathbf{v} = 0 \qquad \text{(entropy conservation)} \tag{2.10}$$

where one defines

$$\frac{D}{Dt} \equiv \frac{\partial}{\partial t} + \mathbf{v} \cdot \nabla.$$

The coupling between both sets of equations is established through Newton's equation of motion for a fluid element that is subject to gravity, electromagnetic forces, and a pressure gradient,

$$\rho \frac{D\mathbf{v}}{Dt} = \mathbf{F} \equiv -\nabla p + \rho \mathbf{g} + \mathbf{j} \times \mathbf{B}. \tag{2.11}$$

In the ideal limit ($\sigma \to \infty$), it is required that $\mathbf{E} + \mathbf{v} \times \mathbf{B} = 0$, and the spatial charge τ as well as its time derivative $\partial\tau/\partial t$ can be neglected. Moreover, in the case of non-relativistic plasmas, the second term in the right hand side of Ampère's law (2.4) vanishes. All of these approximations allow to eliminate variables $\mathbf{E}$ and $\mathbf{j}$, and to obtain the basic set of equations of ideal MHD,

$$\rho\left(\frac{\partial \mathbf{v}}{\partial t} + \mathbf{v} \cdot \nabla \mathbf{v}\right) = -\nabla p + \mathbf{j} \times \mathbf{B} - \rho \mathbf{g}, \quad \mathbf{j} = \nabla \times \mathbf{B} \tag{2.12}$$

$$\frac{\partial \mathbf{B}}{\partial t} = \nabla \times (\mathbf{v} \times \mathbf{B}), \quad \nabla \cdot \mathbf{B} = 0 \tag{2.13}$$

$$\frac{\partial p}{\partial t} = -\mathbf{v} \cdot \nabla p - \gamma p \nabla \cdot \mathbf{v} \tag{2.14}$$

$$\frac{\partial \rho}{\partial t} = -\nabla \cdot (\rho \mathbf{v}) \tag{2.15}$$

The relation $\nabla \cdot \mathbf{B} = 0$ is actually considered an initial condition, since the induction equation (2.13a) shows that, if it vanishes initially, then it remains satisfied at any time. Therefore, (2.12)-(2.15) form a complete set of eight nonlinear partial differential equations for the eight variables $\mathbf{B}(\mathbf{r}, t)$, $\mathbf{v}(\mathbf{r}, t)$, $\rho(\mathbf{r}, t)$ and $p(\mathbf{r}, t)$. The initial and boundary conditions will depend on the particular problem under study.

Ideal MHD equilibrium assumes that all quantities are independent of time and a static plasma ($\mathbf{v} = 0$). Under these assumptions, the conservation of mass (2.9) and energy (2.10) relations are trivially satisfied. The static ideal Ohm's law requires $\mathbf{E} = 0$, such that Faraday's law is automatically fulfilled. The remaining non-trivial equations that define the MHD equilibrium of

the system are given by

$$\mathbf{j} \times \mathbf{B} = \nabla p \tag{2.16}$$
$$\nabla \times \mathbf{B} = \mu_0 \mathbf{j} \tag{2.17}$$
$$\nabla \cdot \mathbf{B} = 0 \tag{2.18}$$

From (2.16)-(2.18) can be deduced that the magnetic field and current density lines must lie in surfaces of constant pressure, since multiplying the first equation by $\mathbf{B}$ or $\mathbf{j}$ results in $\mathbf{B} \cdot \nabla p = 0$ or $\mathbf{j} \cdot \nabla p = 0$. Constant pressure surfaces are sometimes called *flux surfaces*, since no magnetic flux goes across them.

2.3.2 Linear stability analysis

In order to know if a plasma that is slightly perturbed will return to its original equilibrium state (stability) or further enhance the disturbance (instability), it is generally enough to do a linear stability analysis. Indeed, plasma instabilities are usually so virulent that they can destroy and completely modify the structure of the system. This is the reason why it is better to completely avoid their onset in laboratory contexts, which can be ensured by linear stability, such that nonlinear analyses are not really interesting because they only provide details on the plasma self-destruction. For solar phenomena, however, nonlinear simulations can provide meaningful insights on the evolutionary processes and dynamics of the Sun. In this work, we will develop a linear stability analysis, which will greatly simplify the problem. The complete derivation of the linear stability analysis can be found in the literature (e.g. see Bernstein et al., 1958; Biskamp, 1997; Goedbloed and Poedts, 2010).

Assume that an ideal plasma is in MHD stationary equilibrium, and is perturbed by an arbitrarily small perturbation. First, the quantities describing the plasma are linearized,

$$\begin{aligned}
\mathbf{B}(\mathbf{r}, t) &= \mathbf{B}_0(\mathbf{r}) + \mathbf{B}_1(\mathbf{r}, t) \\
\mathbf{v}(\mathbf{r}, t) &= \mathbf{v}_1(\mathbf{r}, t) \\
\rho(\mathbf{r}, t) &= \rho_0(\mathbf{r}) + \rho_1(\mathbf{r}, t) \\
p(\mathbf{r}, t) &= p_0(\mathbf{r}) + p_1(\mathbf{r}, t)
\end{aligned}$$

where $Q_0(\mathbf{r}, t)$ are the equilibrium solutions obtained from (2.16)-(2.18), and the disturbance terms $Q_1(\mathbf{r}, t)$ satisfy $Q_1(\mathbf{r}, 0) = 0$ and $|Q_1/Q_0| \ll 1$. Since the initial equilibrium is static, we set $\mathbf{v}_0$ to 0. Substituting the above quantities into the ideal MHD equations and keeping only linear terms on the perturbed quantities, it is obtained

$$\rho_0 \frac{\partial \mathbf{v}_1}{\partial t} = -\nabla p_1 + \mathbf{j}_1 \times \mathbf{B}_0 + \mathbf{j}_0 \times \mathbf{B}_1 - \rho_1 \mathbf{g}, \quad \mathbf{j}_1 = \nabla \times \mathbf{B}_1 \tag{2.19}$$
$$\frac{\partial \mathbf{B}_1}{\partial t} = \nabla \times (\mathbf{v}_1 \times \mathbf{B}_0), \quad \nabla \cdot \mathbf{B}_1 = 0 \tag{2.20}$$
$$\frac{\partial p_1}{\partial t} = -\mathbf{v}_1 \cdot \nabla p_0 - \gamma p_0 \nabla \cdot \mathbf{v}_1 \tag{2.21}$$
$$\frac{\partial \rho_1}{\partial t} = -\nabla \cdot (\rho_0 \mathbf{v}_1). \tag{2.22}$$

Consider now the vector $\boldsymbol{\xi}(\mathbf{r}, t)$ that represents the displacement of the plasma away from its equilibrium position, such that it satisfies

$$\mathbf{v}_1 = \frac{\partial \boldsymbol{\xi}}{\partial t}.$$

A significant simplification can be done using equations (2.21)-(2.22) to eliminate all the perturbed

quantities and express them only in terms of $\boldsymbol{\xi}$,

$$\mathbf{B}_1 = \nabla \times (\boldsymbol{\xi} \times \mathbf{B}_0) \tag{2.23}$$

$$p_1 = -\boldsymbol{\xi} \cdot \nabla p_0 - \gamma p_0 \nabla \cdot \boldsymbol{\xi} \tag{2.24}$$

$$\rho_1 = -\nabla \cdot (\rho_0 \boldsymbol{\xi}). \tag{2.25}$$

Substituting these expressions into (2.19), the final equation of motion is obtained,

$$\rho_0 \frac{\partial^2 \boldsymbol{\xi}}{\partial t^2} = \mathbf{F}\{\boldsymbol{\xi}\}, \tag{2.26}$$

where $\mathbf{F}$ is the linear self-adjoint operator that represents the force per unit volume,

$$\begin{aligned}\mathbf{F}\{\boldsymbol{\xi}\} &\equiv -\nabla p_1 + \mathbf{j}_1 \times \mathbf{B}_0 + \mathbf{j}_0 \times \mathbf{B}_1 = \\ &= -\nabla p_1 + \nabla \cdot (\rho_0 \boldsymbol{\xi}) \mathbf{g} + \{\nabla \times [\nabla \times (\boldsymbol{\xi} \times \mathbf{B}_0)]\} \times \mathbf{B}_0 / \mu_0 + (\nabla \times \mathbf{B}_0) \times [\nabla \times (\boldsymbol{\xi} \times \mathbf{B}_0)] / \mu_0.\end{aligned}$$

The boundary conditions depend on the particular properties of the system under study. For instance, if we are seeking solutions that do not perturb the outer surface S_p of the plasma (*internal modes*), then the boundary condition can be expressed as $\mathbf{n} \cdot \boldsymbol{\xi}|_{S_P} = 0$, where $\mathbf{n}$ is the normal vector to the plasma surface at each point. Instead, if the boundary is free to move (*external modes*), the problem becomes substantially more complicated. The second approach was taken in the stability analysis that is used in this thesis, since it better represents the situation in the solar corona and interplanetary space. The initial conditions for (2.26) that correspond to a static equilibrium are

$$\boldsymbol{\xi}(\mathbf{r}, 0) = 0, \quad \frac{\partial \boldsymbol{\xi}(\mathbf{r}, 0)}{\partial t} = \mathbf{v}_1(\mathbf{r}, 0) \neq 0.$$

Since $\mathbf{F}$ is a self-adjoint linear functional of $\boldsymbol{\xi}$ (proof in Goedbloed and Poedts, 2010) where the time variable t does not appear explicitly, normal mode solutions of the form

$$\boldsymbol{\xi}(\mathbf{r}, t) = \boldsymbol{\xi}(\mathbf{r}) e^{i\omega t}$$

can be sought. The corresponding eigenvalue equation is

$$-\omega^2 \rho_0 \boldsymbol{\xi} = \mathbf{F}\{\boldsymbol{\xi}\}, \tag{2.27}$$

where $\omega^2 \in \mathbb{R}$ due to the self-adjointness of $\mathbf{F}$ and ρ_0 will be assumed constant. Therefore, if there exists any eigenvalue $\omega^2 < 0$, the perturbation grows exponentially in time and the system is unstable. If $\omega^2 > 0$ for all the eigenvalues of $\mathbf{F}$, then the system is stable.

The concept of exponential stability is valid when $\mathbf{F}$ has a discrete spectrum, which has been shown to be generally true for the unstable part of the spectra of most of the configurations studied until now, including the one that is considered in this work. However, the operator $\mathbf{F}$ becomes ill-behaved for the continuous spectrum, and the stability analysis is significantly more complex. A detailed discussion and exploration of the spectral properties of $\mathbf{F}$, and of the existence and uniqueness of solutions to (2.26) with the appropriate boundary conditions, is beyond the scope of this thesis, and has been addressed in the literature (see e.g. Lifschitz, 1989; Goedbloed and Poedts, 2010; Freidberg, 2014).

As stated in Bernstein et al. (1958) and Goedbloed and Poedts (2010), the eigenfunctions $\boldsymbol{\xi}(\mathbf{r})$ of the operator $\mathbf{F}$ make the *Rayleigh quotient* Λ,

$$\Lambda\{\boldsymbol{\xi}\} = \frac{\displaystyle\int_V \mathrm{d}^3 x \; \boldsymbol{\xi}^* \cdot \mathbf{F}\{\boldsymbol{\xi}\}}{\displaystyle\int_V \mathrm{d}^3 x \; |\boldsymbol{\xi}|^2} \tag{2.28}$$

stationary (i.e. its derivative vanishes), where $\boldsymbol{\xi}^*$ is the complex conjugate of $\boldsymbol{\xi}$, and the stationary values of Λ correspond to the eigenvalues of $\mathbf{F}$. This equivalent variational formulation allows us

to introduce the method developed in Linton et al. (1996) that has been adopted for the stability analysis in the present work. The potential energy of the system $W\{\boldsymbol{\xi}\}$ and the kinetic energy $K\{\boldsymbol{\xi}\}$ are defined as

$$W\{\boldsymbol{\xi}\} = -\frac{1}{2}\int_V \mathrm{d}^3x\ \boldsymbol{\xi}^* \cdot \mathbf{F}\{\boldsymbol{\xi}\}, \quad K\{\boldsymbol{\xi}\} = \frac{1}{8\pi}\int_V \mathrm{d}^3x\ |\boldsymbol{\xi}|^2.$$

Extremizing the generalized energy $U\{\boldsymbol{\xi}\} = W\{\boldsymbol{\xi}\} + \lambda K\{\boldsymbol{\xi}\}$ can be shown to give the extrema of the quotient $W\{\boldsymbol{\xi}\}/K\{\boldsymbol{\xi}\}$, where $K\{\boldsymbol{\xi}\}$ is held constant and λ is the unknown Lagrange multiplier (Freidberg, 2014). Then, since $W\{\boldsymbol{\xi}\}/K\{\boldsymbol{\xi}\} = 4\pi\Lambda\{\boldsymbol{\xi}\}$, with Λ is given in (2.28), this is equivalent to finding the eigenvalues ω^2 of $\mathbf{F}$ in the normal mode formulation (2.27), and at an extremum the Lagrange multiplier λ is related to the eigenvalues by

$$\lambda = -4\pi\rho_0\omega^2.$$

The system is unstable with growth rate $|\omega|$ if $\omega^2 < 0$ (or $\lambda > 0$). If $\lambda < 0$ for all perturbations $\boldsymbol{\xi}$ that solve (2.26) and satisfy the initial and boundary conditions, then the system is stable.

The stability problem can be simplified further if the exact growth rates and evolution of the perturbation are not needed, such that we only want to obtain under which conditions the system is ideal MHD stable. This is achieved through the *energy principle* (Bernstein et al., 1958), which asserts that an equilibrium is stable if and only if $W\{\boldsymbol{\xi}\} > 0$ for all possible displacements $\boldsymbol{\xi}$ satisfying the boundary conditions.

2.3.3 Analysis of the helical kink instability

Assume that the magnetic configuration under study has cylindrical symmetry with fixed cross-sectional radius R and is described by the cylindrical coordinates (r, y, φ), so the magnetic field in equilibrium depends only on the radial coordinate r and has the form

$$\mathbf{B}_0(\mathbf{r}) = (0, B_y(r), B_\varphi(r)).$$

Since the coefficients in the linearized MHD equations are independent of y, φ, a single Fourier harmonic of the perturbation $\boldsymbol{\xi}(\mathbf{r})$ in y, φ at a time can be analyzed (Bateman, 1978),

$$\boldsymbol{\xi}(\mathbf{r}) = (\xi_r(r), \xi_y(r), \xi_\varphi(r))e^{i(ky+m\varphi)},$$

where m and $k \in \mathbb{R}$ determine the type and physical behavior of the instability (see Figure 2.6). The *helical kink instability* corresponds to the value $m = 1$, and k will be referred to as the *wavenumber* of the instability.

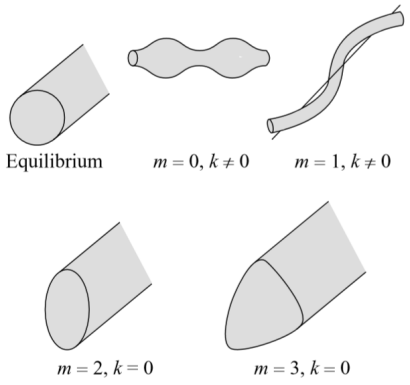

Figure 2.6: Graphical representation of perturbations corresponding to different values of m, k. The pair $m = 0, k \neq 0$ is called the *sausage instability*, and $m = 1, k \neq 0$ is the *kink instability* that makes the axis adopt a helical shape. Retrieved from Freidberg (2007).

The present work uses the stability analysis method developed by Linton et al. (1996), and the details of the derivation that follows can be found there. The perturbation is assumed to be incompressible ($\nabla \cdot \boldsymbol{\xi} = 0$) because it is a condition that is generally fulfilled for the most unstable modes of the system. Then, the perturbation that minimizes the generalized energy of the system $U\{\boldsymbol{\xi}\} = W\{\boldsymbol{\xi}\} + \lambda K\{\boldsymbol{\xi}\}$ with respect to $\boldsymbol{\xi}$ can be obtained from the radial component ξ_r given by the Euler-Lagrange equation

$$\frac{\mathrm{d}}{\mathrm{d}r}\left(f\frac{\mathrm{d}\xi_r}{\mathrm{d}r}\right) - g\xi_r = 0, \tag{2.29}$$

where f and g are defined as

$$f = \frac{r^3(\lambda + \left(kB_y + \frac{B_\varphi}{r}\right)^2}{1 + k^2r^2},$$

$$g = \frac{k^2 r}{1+k^2r^2}\left[r^2\left\{\lambda + \left(kB_y + \frac{B_\varphi}{r}\right)^2\right\} - r\frac{\mathrm{d}|\mathbf{B}_0(r)|^2}{\mathrm{d}r}\right.$$

$$\left. -2B_\varphi^2\left\{\frac{2\left(kB_y + \frac{B_\varphi}{r}\right)^2}{\lambda + \left(kB_y + \frac{B_\varphi}{r}\right)^2} - 1\right\} + \frac{2}{1+k^2r^2}(r^2\lambda + k^2r^2B_y^2 - B_\varphi^2)\right].$$

Regularity at the origin is ensured by the boundary conditions $\dot{\xi}_r(0) = 0$ and $\xi_r(0) = \xi_0$ (ξ_0 can be set to 1 without loss of generality).

With regard to the external medium and its relation to the plasma, there are many configurations that can be considered. For example, stability analyses in tokamaks or coronal loops sometimes assume the confinement of the plasma by a conducting wall ($\xi_r(R) = 0$, so it is an internal mode) or the presence of an external vacuum field $B(r > R) \neq 0$. In contrast, Linton et al. (1996) considers that the plasma has a free boundary and no external magnetic field. An additional boundary condition is therefore obtained when imposing the continuity of the total pressure across the plasma boundary and the Euler-Lagrange equation at the outer edge of the configuration, even if there is a discontinuity in the magnetic field,

$$D(\lambda; R, k) = \left[k^2|\mathbf{B}(R)|^2 + \lambda + \lambda\frac{(1+k^2R^2)K_1(|k|R)}{|k|RK_0(|k|R) + K_1(|k|R)}\right]\xi_r(R)$$
$$+\left\{R\lambda + R\left(kB_y + \frac{B_\varphi}{r}\right)^2\right\}\dot{\xi}_r(R) = 0, \tag{2.30}$$

where K_0 and K_1 are modified Bessel functions. Eq. (2.30) can be regarded as a dispersion relation for the eigenvalue λ.

A cylindrical magnetic configuration is said to be kink stable if it is stable to perturbations of any wavenumber k. And so, taking into account the discussion of the previous section (the system is unstable if there exists $\lambda > 0$), we reach the main conclusion that has been used as the basis of the stability analysis of the present work: *the necessary and sufficient condition for the kink stability of an MFR is that the largest λ for which the dispersion relation (2.30) holds is negative for all k.* This method also allows us to obtain the growth rates and the shape of the most unstable modes.

2.4 MHD description of magnetic flux ropes (MFRs)

Magnetic fields are present throughout the universe and strongly interact with plasmas, structuring them into different configurations and causing many of the most common phenomena. These structures are mainly combinations of two basic building blocks: *magnetic flux tubes* (see Figure 2.7) and *current sheets*. This section will describe magnetic flux tubes and MFRs that are essential in the derivation of different CME models (discussed in the next chapter).

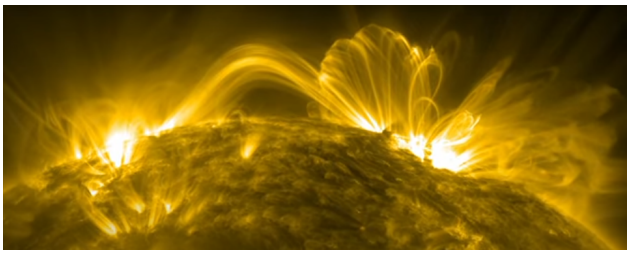

Figure 2.7: Photograph taken by NASA/SDO of coronal loops in the Sun surface, resembling the structure of flux tubes. Retrieved from `https://www.nasa.gov/mission_pages/sdo/news/flux-ropes.html`.

2.4.1 Defining magnetic flux tubes and flux ropes

A *magnetic field line* is a curve that is tangent to the magnetic field $\mathbf{B}$ at any point. From here, a *magnetic flux tube* can be defined as the volume enclosed by the set of field lines intersecting a simple closed curve (see Figure 2.8). A *magnetic flux rope* (MFR) is a twisted magnetic flux tube, such that the field lines are wrapped around the axis (Priest, 2013).

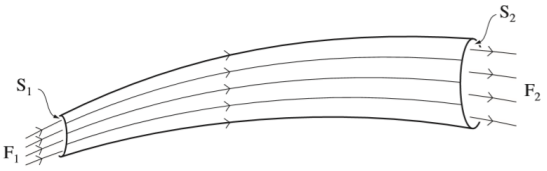

Figure 2.8: Diagram of part of a magnetic flux tube bounded by the areas S_1, S_2 and with fluxes F_1, F_2. Retrieved from Priest (2013).

Flux conservation

The *strength* of a flux tube is defined as the magnetic flux that crosses a section S,

$$F = \int_S \mathbf{B} \cdot \mathrm{d}\mathbf{S},$$

where $\mathrm{d}\mathbf{S}$ is taken in the same sense as $\mathbf{B}$, so F is always positive. In fact, $F = \langle B_n \rangle A$, where $\langle B_n \rangle$ is the absolute value of the mean normal field to the surface S, and A is the cross-sectional area of the section considered. Integrating Gauss' law for magnetism $\nabla \cdot \mathbf{B} = 0$ over the volume of a flux tube enclosed between two sections S_1 and S_2 gives

$$0 = \int_V \nabla \cdot \mathbf{B} \, \mathrm{d}V = \int_{S_1} \mathbf{B} \cdot \mathrm{d}\mathbf{S} + \int_{S_2} \mathbf{B} \cdot \mathrm{d}\mathbf{S} = -F_1 + F_2,$$

where F_1 and F_2 are the strengths of $\mathbf{B}$ across S_1 and S_2, respectively (see Figure 2.8). This implies that the strength is constant across any surface intersecting the tube. Therefore, from $F = \langle B_n \rangle A$ can be inferred that if a flux tube narrows, the mean field $\langle B_n \rangle$ must increase and vice versa.

2.4.2 Magnetic forces and a physical picture of the kink instability

In section 2.3.1, we saw that the magnetic field acted on the plasma through the Lorentz force $\mathbf{j} \times \mathbf{B}$ that appears in Newton's equation of motion for a fluid element (2.11). An important feature to take into account about magnetic forces is that they do not promote nor inhibit the motion of the plasma along the magnetic field lines. This means that any motion or variation of density along them must have been caused by other forces (i.e. pressure gradients or gravity).

In order to better understand the effects of the magnetic forces acting on the plasma, it is worth decomposing them into two different terms, using Ampère's law ($\mathbf{j} = (\nabla \times \mathbf{B})/\mu_0$) and the vector identity $(\nabla \times \mathbf{B}) \times \mathbf{B} = \mathbf{B} \cdot \nabla \mathbf{B} - \nabla(\mathbf{B}^2/2)$. Keeping only the terms that are orthogonal to the magnetic field, the Lorentz force can be rewritten as

$$\mathbf{j} \times \mathbf{B} = \frac{B^2}{\mu_0 R_c} \hat{\mathbf{n}} - \nabla_\perp \left(\frac{B^2}{2\mu_0} \right), \tag{2.31}$$

where $\hat{\mathbf{n}}$ is the principal normal direction of the magnetic field line, R_c is the local radius of curvature, and $\nabla_\perp$ takes the gradient only in the direction orthogonal to $\mathbf{B}$.

The first term in (2.31) corresponds to the *magnetic tension force*. It is directed radially inward with respect to the magnetic field line curvature and tends to straighten it, in the same way as tension would act on a curved wire or string (see Figure 2.9 (left)).

The second term corresponds to the so-called *magnetic pressure*. It is exerted from regions with higher magnetic pressure to regions with lower values of it (see Figure 2.9 (right)).

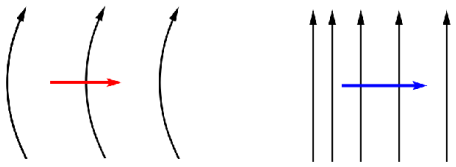

Figure 2.9: Left: the magnetic tension force direction is radially inward with respect to the magnetic field line curvature. Right: the magnetic pressure, $B^2/(2\mu_0)$, creates a force directed towards the regions where it adopts a lower value.

We can now use these concepts to develop more intuition on the helical kink instability of MFRs, whose stability analysis was discussed in section 2.3.3 and an example of its occurrence in a laboratory plasma is shown in Figure 2.5. When the axis of a cylindrical MFR is slightly disturbed to adopt a helical shape (see Figure 2.10), which corresponds to the onset of a potential kink instability, the magnetic pressure increases at region A, and decreases at region B. Therefore, a force appears that is directed from A to B and has a destabilizing effect, since it tends to increase the curvature of the axis. Conversely, as the curvature increases, a stabilizing magnetic tension force appears that tends to straighten the field lines and thus decreases the perturbation. If the axial magnetic field B_y is not strong enough, the magnetic tension will not compensate for the force caused by the magnetic pressure gradient, and therefore the kink instability will keep on growing.

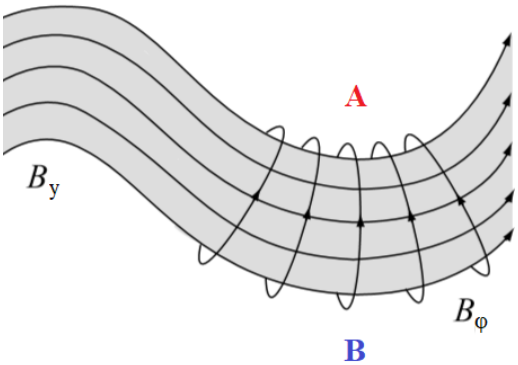

Figure 2.10: Schematic representation of a MFR that is developing a helical kink instability. The axial and poloidal magnetic field components, B_y and B_φ, are depicted separately.

2.4.3 Magnetic helicity

Apart from storing magnetic energy and acting as a channel for flows of fast particles, heat and plasma, magnetic flux tubes are also described by an important topological quantity, *magnetic helicity*, which is related to their internal structure (the amount of internal twist) as well as the external structure (the linkage between different flux tubes). This quantity can be defined in a volume V as

$$H = \int_V \mathbf{A} \cdot \mathbf{B} \ \mathrm{d}V,$$

where $\mathbf{A}$ is the vector potential ($\mathbf{B} = \nabla \times \mathbf{A}$). If the volume V is magnetically closed, that is to say, if the magnetic field lines do not enter nor leave it, the helicity H is gauge invariant (i.e. it does not change if $\mathbf{A}$ is replaced by $\mathbf{A} + \nabla\Phi_A$, where Φ_A is an arbitrary function).

However, is it possible to define an alternative expression that is also gauge invariant for non-magnetically closed volumes? (Berger and Field, 1984) proposed such a quantity, the *relative magnetic helicity*, H_r, that is defined as

$$H_r = \int_V (\mathbf{A} \cdot \mathbf{B} - \mathbf{A}_0 \cdot \mathbf{B}_0) \ \mathrm{d}V, \tag{2.32}$$

where $\mathbf{B}_0 = \nabla \times \mathbf{A}_0$ is a potential field that satisfies $\mathbf{B}_0 \cdot \mathbf{n} = \mathbf{B} \cdot \mathbf{n}$ on S, and S is the surface that encloses V. The potential field $\mathbf{B}_0$ is actually uniquely specified in all V just from imposing the boundary condition $\mathbf{B_0} \cdot \mathbf{n} = \mathbf{B} \cdot \mathbf{n}$ on S. $\mathbf{A}_0$ is also fully determined by requiring $\mathbf{A} \times \mathbf{n} = \mathbf{A}_0 \times \mathbf{n}$ on S.

The relative magnetic helicity turns out to be very useful, since it has been shown to be a global topological invariant in ideal MHD. Even in weakly resisitve MHD, which allows the occurrence of reconnection, the helicity decays very slowly with time. The conservation of magnetic helicity thus imposes important constraints on physically allowed plasma motions (Priest, 2013), and will provide us with interesting conclusions about the occurrence of the kink instability in expanding MFRs.

3 . MFR modeling of CMEs

An important fraction of the *in situ* signatures of ICMEs that have been detected until now, displays the characteristics of the heliospheric magnetic structures known as *magnetic clouds* (MCs): the increase in the average magnetic field strength, the monotonic rotation of the magnetic field direction through a large angle, a low proton temperature, and a small ratio of the plasma to magnetic pressure, i.e. $\beta_{proton} \ll 1$, such that the magnetic forces dominate the structure.

The large net rotation of the magnetic field that is observed in MCs is an indicator of their magnetic flux rope (MFR) configuration: fundamental structures that can be defined as collections of magnetic field lines wrapping around an internal main axis in a twisting way, confining magnetized plasma within them (see section 2.4.1).

This chapter describes the MFR models that will be used to analyze the kink instability of magnetic clouds: the *circular-cylindrical* (CC) analytical model developed by Nieves-Chinchilla et al. (2016), the linear force-free Lundquist model, and the uniformly-twisted Gold-Hoyle (GH) model. Some comments will be made regarding the inclusion of expansion to the CC model. Finally, two different types of reconstruction techniques will be compared in the study of a particular CME observed by Parker Solar Probe, which has contributed to the thorough analysis in Lario et al. (in review).

3.1 Cylindrically symmetric models of MFRs

3.1.1 Derivation of the general equations

A cylindrical MFR structure of radius R at equilibrium is considered (see Figure 3.1). It is parametrized in circular-cylindrical coordinates (r, y, φ), with $r \in (0, R], y \in \mathbb{R}, \varphi \in [0, 2\pi)$, which are related to the Cartesian coordinates (x_c, y_c, z_c) through

$$x_c = r\cos\varphi, \quad y_c = y, \quad z_c = r\sin\varphi.$$

The orthonormalized basis vectors $\{\mathbf{e}_r, \mathbf{e}_y, \mathbf{e}_\varphi\}$ in the cylindrical coordinate system can be written in terms of the Cartesian basis vectors $\{\mathbf{u}_x, \mathbf{u}_y, \mathbf{u}_z\}$ as

$$\begin{aligned}\mathbf{e}_r &= \cos\varphi\mathbf{u}_x + \sin\varphi\mathbf{u}_z\\ \mathbf{e}_y &= \mathbf{u}_y\\ \mathbf{e}_\varphi &= -\sin\varphi\mathbf{u}_x + \cos\varphi\mathbf{u}_z.\end{aligned}$$

The *cylindrical approximation* is used, which assumes that the radial magnetic field vanishes, $B_r = 0$, and that the magnetic field components only depend on r. The magnetic field is thus given by

$$\mathbf{B}(\mathbf{r}) = (0, B_y(r), B_\varphi(r)),$$

and the field lines lie in cylindrical surfaces around the y axis, about which they are twisted with a constant angle for each particular r. Under these assumptions, Gauss' law for magnetism $\nabla\cdot\mathbf{B} = 0$ is satisfied, and to obtain the relation between the magnetic field and the current density, Ampère's

law $\nabla \times \mathbf{B} = \mu_0 \mathbf{j}$ in cylindrical coordinates is applied,

$$\mu_0 \mathbf{j} = \nabla \times \mathbf{B} = \left(\frac{\partial B_\varphi}{\partial y} - \frac{1}{r} \frac{\partial B_y}{\partial \varphi} \right) \mathbf{e}_r + \frac{1}{r} \left(\frac{\partial B_r}{\partial \varphi} - \frac{\partial (r B_\varphi)}{\partial r} \right) \mathbf{e}_y + \left(\frac{\partial B_y}{\partial r} - \frac{\partial B_r}{\partial y} \right) \mathbf{e}_\varphi.$$

Since $B_r = 0$ and the derivatives on y and φ vanish due to the cylindrical approximation, the following set of equations that are valid in every point of the MFR are obtained,

$$j_r = 0 \tag{3.1}$$

$$j_y = -\frac{1}{\mu_0 r} \frac{\partial (r B_\varphi)}{\partial r} \tag{3.2}$$

$$j_\varphi = \frac{1}{\mu_0} \frac{\partial B_y}{\partial r} \tag{3.3}$$

Equations (3.2) and (3.3) are integrated from 0 to r, taking into account that $B_\varphi(r = 0) = 0$ to maintain regularity at the origin, and setting $B_y(r = 0) = B_y^0$, such that the final result expresses the magnetic field components in terms of the current density,

$$\begin{cases} B_r = 0 \\ B_y = B_y^0 + \mu_0 \displaystyle\int_0^r j_\varphi(r')\, \mathrm{d}r' \\ B_\varphi = -\dfrac{\mu_0}{r} \displaystyle\int_0^r r' j_y(r')\, \mathrm{d}r' \end{cases} \tag{3.4}$$

Any other physical quantity can be derived from these equations, which actually represent the core of any cylindrical MFR model.

For a straight cylindrical structure, it can be shown (Dasso et al., 2003) that the relative magnetic helicity per unit length, as defined in equation (2.32), is given by

$$\frac{H_r}{L} = 4\pi \int_0^R A_\varphi B_\varphi r dr. \tag{3.5}$$

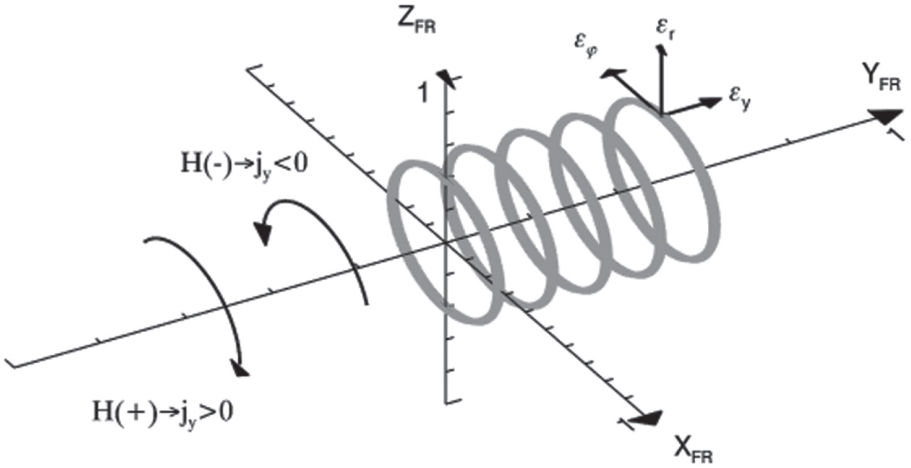

Figure 3.1: Schematic representation of the MFR and the circular-cylindrical basis vectors. The *handedness* of the MFR is indicated according to the the sign of the axial current component j_y, assuming $B_y \geq 0$. Retrieved from Nieves-Chinchilla et al. (2016).

3.1.2 Force-free MFR models

Force-free (FF) models are those in which the Lorentz force vanishes throughout the MFR,

$$\mathbf{j} \times \mathbf{B} = \mathbf{0}.$$

Therefore, in the static magnetic equilibrium defined by equations (2.16)-(2.18), the pressure of a FF magnetic configuration is constant and $\mathbf{j}$ is aligned with $\mathbf{B}$, so Ampère's law becomes

$$\nabla \times \mathbf{B} = \alpha \mathbf{B}, \tag{3.6}$$

where α is, in general, spatially dependent. Taking the divergence of (3.6) and using $\nabla \cdot \mathbf{B} = 0$, it is obtained that α must obey $\mathbf{B} \cdot \nabla \alpha = 0$, which means that α is constant along field lines. Fields that have constant α throughout the plasma are called *linear (or constant-α) FF fields*. Otherwise, they are called *nonlinear FF fields*.

Linear force-free fields: the Lundquist model

The circular-cylindrical linear FF model has been the standard model to reconstruct the *in situ* magnetic signatures of MCs since the 1990s (Lepping et al., 1990). It is known as the *Lundquist model* (Lundquist, 1951), and for a MFR of radius R, it is given by

$$B_y(\bar{r}) = B_y^0 J_0(\alpha \bar{r}), \quad B_\varphi(\bar{r}) = B_y^0 J_1(\alpha \bar{r}), \tag{3.7}$$

where J_0, J_1 are Bessel functions, $\bar{r}$ is the normalized radius coordinate ($\bar{r} = r/R$), B_y^0 is the magnitude of the magnetic field at the axis, and α is the fitting parameter (see Figure 3.2 (left)).

A property that makes linear FF models particularly interesting was proved by Woltjer (1958): the state of minimum magnetic energy for a given total magnetic helicity of a closed system is given by a linear FF field. Actually, he showed that any constant-α FF field extremizes the energy of the system, but not necessarily minimizes it.

Nonlinear force-free fields: the Gold-Hoyle model

Another MFR model that is very commonly used is the nonlinear FF uniformly-twisted *Gold-Hoyle* (GH) model. For a MFR of radius R, its magnetic field is given by

$$B_y(\bar{r}) = \frac{B_y^0}{1 + q^2 \bar{r}^2}, \quad B_\varphi(\bar{r}) = \frac{q \bar{r} B_y^0}{1 + q^2 \bar{r}^2} \tag{3.8}$$

where $\bar{r}$ is the normalized radius coordinate ($\bar{r} = r/R$), B_y^0 is the magnitude of the magnetic field at the axis, and q is the fitting parameter (see Figure 3.2 (right)).

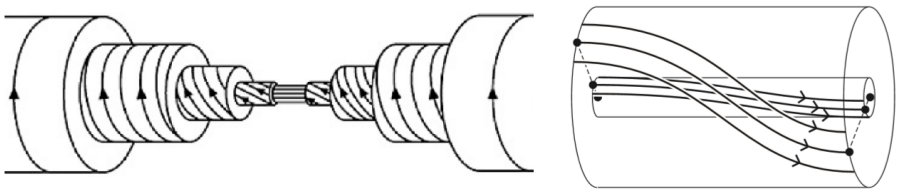

Figure 3.2: Left: Lundquist MFR at different r. It can be observed that the field lines are increasingly twisted around the axis as r increases. Retrieved from Rong et al. (2013). Right: GH MFR at different r. It shows that the twist of the field lines remains constant along the radius. Retrieved from Priest (2013).

3.2 Twist distribution of MFR models

Different MFR models have been developed since the early 1980s for the reconstruction of MFRs in ICMEs only from 1D measurements along the spacecraft observational path. The linear FF Lundquist model (3.7) or the nonlinear FF GH model (3.8) are two of the most commonly used. However, they impose strong conditions on the magnetic field since they ignore the magnetic forces that can arise from interactions with other CMEs or the ambient solar wind, as well as other phenomena like rotations, cross-sectional distortions or instabilities.

Non-force-free (NFF) methods are important to account for more general situations that occur in the interplanetary space. Some of them assume a particular current density and then solve Maxwell's equations for the magnetic field with circular or elliptical cross sections (e.g. the CC model that will be explained in section 3.3 and the elliptical-cylindrical model for MCs, both developed by Nieves-Chinchilla et al., 2016, 2018b). Another well-known technique is the Grad-Shafranov model, which is based on MHD equilibrium equations with some geometric simplifications. It usually shows good agreement with multipoint *in situ* measurements (Hu, 2017).

All of these models differ in the *twist* they predict, i.e. the number of turns that the magnetic field lines make around the axis per unit length. Some of them show twist profiles that increase with radius within the cylindrical structure, like the Lundquist model or the most commonly used forms of the CC model. Others like the Gold-Hoyle (GH) model, assume uniform twist. This section will define this quantity and stress its importance in the physical behavior of MFRs.

3.2.1 Definition of twist

The *total twist angle* Φ of a field line going from one end to the other of a MFR with length L is

$$\Phi(r) = \frac{LB_\varphi(r)}{rB_y(r)}, \tag{3.9}$$

and its geometrical interpretation is shown in Figure 3.3. The total number of turns done by a magnetic field line around the MFR axis is given by $N = \Phi/(2\pi)$, where Φ is measured in radians. Finally, the *twist* Q of a MFR is defined as the angle covered by a magnetic field line around the axis per unit length,

$$Q = \frac{\Phi}{L} = \frac{B_\varphi}{rB_y}. \tag{3.10}$$

Therefore, for example, the twist of the Lundquist model (3.7) is given by $Q = J_1(\alpha\bar{r})/(R\bar{r}J_0(\alpha\bar{r}))$ (it increases along the radius of the MFR), and for the GH model (3.8) it adopts the uniform value of $Q = q/R$ (see schematic representation in Figure 3.2).

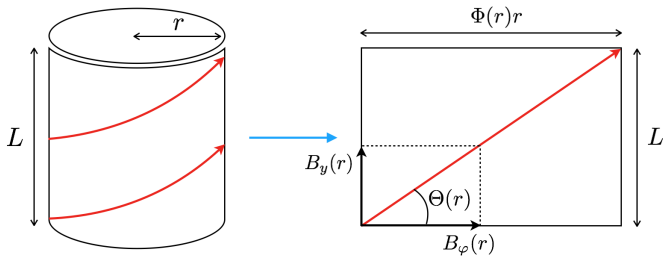

Figure 3.3: The trajectory of a magnetic field line in going from one end of the MFR to the other is represented in red. The cylindrical surface is flattened out, so $\tan\Theta(r) = L/(r\Phi(r)) = B_y(r)/B_\varphi(r)$. Isolating $\Phi(r)$, the total twist angle is obtained $\Phi(r) = LB_\varphi(r)/(rB_y(r))$.

3.2.2 The role of the twist in the occurrence of MFR instabilities

The twist is an important quantity describing MFRs, since it is related to the amount of magnetic free energy density stored in the structure and its tendency to develop certain instabilities. This is because twisted plasma structures are subject to the occurrence of the helical kink instability, which makes the axis become a helix itself, as explained in section 2.3.3. Studying the twist distribution of MFRs therefore gives us a lot of information about the configuration and physical properties of ICMEs that contain MCs (see Figure 3.4).

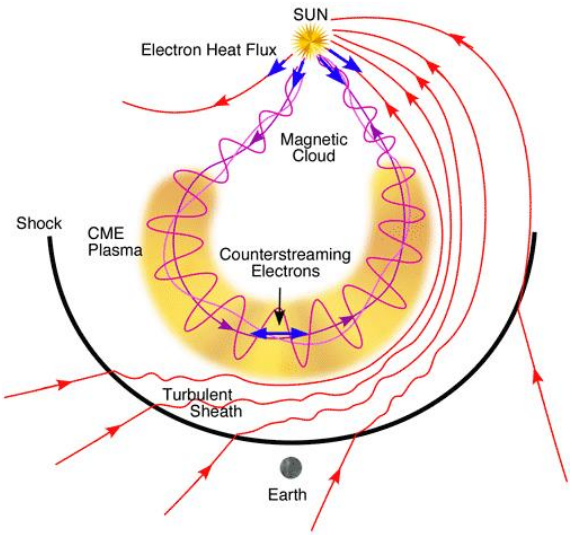

Figure 3.4: Model of the structure of an ICME. The twisted field lines of the MFR extending around the axis can be clearly observed. Retrieved from `https://eclipse2017.nasa.gov/coronal-mass-ejections`.

Although a MFR needs the presence of twist to maintain the integrity of the structure (Schuessler, 1979; Longcope et al., 1996), the kink instability takes place when the twist becomes larger than a critical value and can completely alter the original configuration. The stability threshold depends on many factors, like the internal magnetic configuration, the external field, the β_{proton} or the aspect ratio, among others (Mikic et al., 1990; Linton et al., 1996; Török and Kliem, 2005). We can mention some examples:

- For toroidal fusion power reactors, a well-known result is the *Kruskal-Shafranov limit*, which states that $\Phi_c = 2\pi$, where Φ_c is the critical total twist angle of a field line around the axis for the occurrence of the kink instability.
- For straight circular-cylindrical geometries, it was found in Dungey and Loughhead (1954) that the critical twist Φ_c follows the relation $\Phi_c = 2\frac{L}{R}$, where L is the axial length and R is the radius of the MFR.
- For *line-tied* MFRs (with the footpoints anchored on the photosphere) described by the GH model, Hood and Priest (1981) found that the line-tying condition had a stabilizing effect, with $\Phi_c = 2.5\pi$.

3.2.3 Measurements and relevance of the twist in interplanetary MFRs

In the heliosphere, the are two main ways that are used to estimate the twist of interplanetary MFRs: using MFR modeling along with the Grad-Shafranov reconstruction technique, or probes of energetic particles to infer the total field-line length (Kahler et al., 2011). For example, the velocity-modified GH model was applied in the analysis of the 126 MCs in Lepping's list (Lepping et al., 2006), and the results showed that all interplanetary MFRs have a twist smaller than 12π

rad per AU, with total twist angle Φ bounded by $0.2\frac{L}{R} < \Phi < 2\frac{L}{R}$, and an average of $\Phi = 0.6\frac{L}{R}$ (Wang et al., 2016).

However, twist observations have not yet provided a consensus on how the twist distribution of CMEs should be. Some support that CMEs are uniformly-twisted structures, or that they have a high-twist core enveloped by a less-twisted outer shell. On the other hand, a recent study based on a superposed epoch analysis of a set of MCs detected by Wind between 1995-2012 showed that the twist distribution is nearly constant in about half their central part (with an average of 11.5 turns per AU), and then it increases up to a factor two towards the MC boundaries (Lanabere et al., 2020).

Even the most commonly used MFR models have differing twist distributions: the linear force-free (LFF) Lundquist model, which has been widely used to fit a large variety of ICMEs, shows an increasing twist profile along the radius of the cross section; the GH model has uniform twist; and other NFF models, like the CC model, can show a wide range of twist profiles and are also able to fit great collections of events (Nieves-Chinchilla et al., 2018a).

Further research and measurements of the twist distribution within interplanetary MFRs is very important, since not only it allows us to gain better insight into the most plausible initiation process as well as MFR models, according to the theoretical twist distributions they predict; it also makes it possible to predict the range of parameters for which MFRs become kink unstable, and possibly start to rotate (Vourlidas et al., 2011; Nieves-Chinchilla et al., 2012). In fact, the kink instability is nowadays regarded as a promising phenomenon to explain the way MFRs emerge through the photosphere (Knizhnik et al., 2018). With regard to CME propagation in the interplanetary space, the analysis of the kink stability behavior in expanding CMEs (Berdichevsky, 2013) could also provide insightful contributions to the field. All of these points will be further addressed in section 4.2.

3.3 CC model and expanding MFRs

The CC model developed in Nieves-Chinchilla et al. (2016) does not impose any force-free condition on the MFR. It assumes a generic polynomial expansion of the current density

$$\mathbf{j} = \sum_{m=0}^{\infty} \beta_m r^m \mathbf{e}_y - \sum_{n=1}^{\infty} \alpha_n r^n \mathbf{e}_\varphi, \tag{3.11}$$

where α_n, β_m are arbitrary real coefficients. Substituting this expression into the general equations for the magnetic field of a cylindrically symmetric MFR (3.4), the expression of the CC magnetic field is obtained as

$$\begin{cases} B_r = 0 \\ B_y = B_y^0 - \mu_0 \displaystyle\sum_{n=1}^{\infty} \alpha_n \frac{r^{n+1}}{n+1} \\ B_\varphi = -\mu_0 \displaystyle\sum_{m=0}^{\infty} \beta_m \frac{r^{m+1}}{m+2}. \end{cases} \tag{3.12}$$

It is necessary to impose $\lim_{r\to 0} B_\varphi(r) = 0$ and $\lim_{r\to 0} j_\varphi(r) = 0$ to avoid a singularity in the axis, which implies that $n \geq 1$ and $m \geq 0$. By convention, the component B_y is assumed to be positive and decreases from a maximum B_y^0 at the axis to a minimum at the boundary $r = R$, so that j_φ is taken to be negative (i.e. $\alpha_n > 0$). The *handedness* or *chirality* (indicated as H in Figure 3.1) is thus determined by the sign of j_y.

3.3.1 The CC model reconstruction technique

The details on the reconstruction technique of the CC model are specified in Nieves-Chinchilla et al. (2016). It uses a multiple regression technique to infer the spacecraft trajectory with the

Levenberg-Marquardt algorithm. Its aim is to minimize the quantity χ^2,

$$\chi^2 = \frac{1}{N}\sum[(B_x^{exp} - B_x^{GSE})^2 + (B_y^{exp} - B_y^{GSE})^2 + (B_z^{exp} - B_z^{GSE})^2], \tag{3.13}$$

where N is the number of data points, $(B_x^{exp}, B_y^{exp}, B_z^{exp})$ are the experimental data in the spacecraft coordinate system (Geocentric Solar Ecliptic or GSE), and $(B_x^{GSE}, B_y^{GSE}, B_z^{GSE})$ are the corresponding theoretical values obtained from the model.

It is assumed that the mean solar wind bulk velocity v_{sw} and the transit time t_s of the spacecraft across the MFR are known. The parameters of the model are θ (tilt), ϕ (longitude), y_0 (*impact parameter* or minimum distance of the spacecraft to the MFR y axis), and the coefficients α_n, β_m of the CC model (3.12).

The transformation to go from the local MFR Cartesian coordinate system, $\mathbf{B}^L$, to the spacecraft GSE coordinate system, $\mathbf{B}^{GSE}$, is done applying a rotation of θ around $\hat{x}_{GSE}$, and of ϕ around $\hat{z}_{GSE}$, which results in

$$\begin{pmatrix} B_x^{GSE} \\ B_y^{GSE} \\ B_z^{GSE} \end{pmatrix} = \begin{pmatrix} \cos\phi & -\sin\phi\cos\theta & \sin\phi\sin\theta \\ \sin\phi & \cos\phi\cos\theta & -\cos\phi\sin\theta \\ 0 & \sin\theta & \cos\theta \end{pmatrix} \begin{pmatrix} B_x^L \\ B_y^L \\ B_z^L \end{pmatrix} \tag{3.14}$$

The values (B_x^L, B_y^L, B_z^L) are obtained from the CC model (3.12) as follows. The MFR is expanding radially away from the Sun (which corresponds to the $\hat{x}_{GSE}$ direction). The satellite local-cylindrical coordinates along the MFR are

$$r_{sat} = \sqrt{x_{sat}^2 + z_{sat}^2} \tag{3.15}$$

$$\sin\varphi_{sat} = \frac{z_{sat}}{r_{sat}}, \tag{3.16}$$

where x_{sat} and z_{sat} are the spacecraft coordinates in the local MFR Cartesian system. Assuming that the spacecraft trajectory in GSE coordinates across the MFR is $(v_{sw}(t-t_0) - x_0, 0, -z_0)$ (where t_0 is the time at which the MFR encounters the spacecraft, $-x_0$ is the x GSE coordinate at the entrance, and z_0 is constant), and then applying the inverse transformation of (3.14),

$$\begin{cases} x_{sat} = (v_{sw}(t-t_0) - x_0)\cos\phi \\ z_{sat} = (v_{sw}(t-t_0) - x_0)\sin\theta\sin\phi - z_0\cos\theta \end{cases}$$

The magnetic field circular-cylindrical components given by (3.12), (B_r, B_y, B_φ), can now be transformed into (B_x^L, B_y^L, B_z^L) by

$$\begin{pmatrix} B_x^L \\ B_y^L \\ B_z^L \end{pmatrix} = \begin{pmatrix} \cos\varphi_{sat} & 0 & -\sin\varphi_{sat} \\ 0 & 1 & 0 \\ \sin\varphi_{sat} & 0 & \cos\varphi_{sat} \end{pmatrix} \begin{pmatrix} B_r \\ B_y \\ B_\varphi \end{pmatrix}. \tag{3.17}$$

It only remains to find z_0 and x_0 in terms of the parameters of the model. The value z_0 comes from imposing that the impact parameter y_0 is the minimum distance to the flux rope axis that the spacecraft ever reaches, such that it minimizes the function

$$D^2(t) = r_{sat}^2(t) = (v_{sw}(t-t_0) - x_0)^2\cos^2\phi + ((v_{sw}(t-t_0) - x_0)\sin\theta\sin\phi - z_0\cos\theta)^2.$$

The derivative vanishes at t_{min} given by

$$t_{min} = t_0 + \frac{x_0}{v_{sw}} + \frac{z_0\sin\theta\cos\theta\sin\phi}{v_{sw}H^2},$$

where $H = \sqrt{\cos^2\phi + \sin^2\phi \sin^2\theta}$. Imposing $y_0^2 = D^2(t_{min})$, and isolating z_0, it is obtained that

$$z_0 = \frac{y_0 H}{\cos\theta \cos\varphi}. \tag{3.18}$$

The quantity x_0 is computed by making the radial coordinate of the spacecraft at the entrance and at the exit of the MFR be the same, such that $R^2 = D^2(t_0) = D^2(t_0 + t_s)$, since a circular cross section without expansion has been assumed:

$$R^2 = D^2(t_0) = x_0^2 \cos^2\phi + (-x_0 \sin\theta \sin\phi - z_0 \cos\theta)^2 \tag{3.19}$$

$$R^2 = D^2(t_0 + t_s) = (v_{sw}t_s - x_0)^2 \cos^2\phi + ((v_{sw}t_s - x_0)\sin\theta \sin\phi - z_0 \cos\theta)^2 \tag{3.20}$$

The solution for x_0 is

$$x_0 = \frac{v_{sw}t_s}{2} + \frac{\tan\phi \sin\theta}{H} y_0. \tag{3.21}$$

Therefore, $(B_x^{GSE}, B_y^{GSE}, B_z^{GSE})$ are calculated this way at each iteration of the Levenberg-Marquardt algorithm until χ^2 is minimized, and the output parameters of the model are φ, θ, y_0 and the coefficients α_n, β_m, of which an initial approximation is initially required.

3.3.2 Conservative quantities in expanding CC MFRs

When an ICME travels through the heliosphere, and there is no erosion nor reconnection with the ambient solar wind, the relative magnetic helicity H_r and the axial and poloidal magnetic fluxes ϕ_y, ϕ_φ are conserved (Nieves-Chinchilla, 2018). The magnetic fluxes in the CC model (3.12) of a MFR with radius R and length L, are given by

$$\begin{aligned} \phi_y(r) &= \int_{S_y} \mathbf{B} \cdot \mathrm{d}\mathbf{S} = \pi r^2 \left(B_y^0 - 2\mu_0 \sum_{n=1}^{\infty} \alpha_n \frac{r^{n+1}}{(n+1)(n+3)} \right) \\ \phi_\varphi(r) &= \int_{S_\varphi} \mathbf{B} \cdot \mathrm{d}\mathbf{S} = \mu_0 L \sum_{m=0}^{\infty} \beta_m \frac{r^{m+2}}{(m+2)^2} \end{aligned} \tag{3.22}$$

The relative magnetic helicity H_r is calculated as expressed in (3.5). Assuming that a MFR is described by the CC model when it expands from radius R to R', and from length L to L', the conservation of $\phi_y, \phi_\varphi, H_r$ imposes physical constraints on the free coefficients of the CC model (see section 4.1.4 in next chapter).

3.3.3 Including the expansion to the CC reconstruction process

The expansion velocity (v_{exp}) of MFRs can be analyzed and measured in different ways from *in situ* observations, and it can include a radial as well as an axial expansion components. Assume that v_{exp} corresponds to the expansion rate of the MFR cross-sectional radius R with respect to the axis. Then, the only thing that needs to be changed in the reconstruction technique of section 3.3.1 is the radius of the MFR at the exit of the spacecraft, which will now have expanded to $R + v_{exp}t_s$. Therefore, equations (3.19)-(3.20) are rewritten as

$$R^2 = D^2(t_0) = x_0^2 \cos^2\phi + (-x_0 \sin\theta \sin\phi - \cos\theta z_0)^2 \tag{3.23}$$

$$(R + v_{exp}t_s)^2 = D^2(t_0 + t_s) = (v_{sw}t_s - x_0)^2 \cos^2\phi + ((v_{sw}t_s - x_0)\sin\theta \sin\phi - z_0 \cos\theta)^2 \tag{3.24}$$

Substituting z_0 in (3.18) into equations (3.23)-(3.24), and using $H = \sqrt{\cos^2\phi + \sin^2\phi \sin^2\theta}$, they can be rewritten as

$$R^2 = x_0^2 H^2 + \frac{y_0^2 H^2}{\cos^2\phi} - 2x_0 y_0 H \sin\theta \tan\phi \tag{3.25}$$

$$\begin{aligned}(R + v_{exp}t_s)^2 = x_0^2 H^2 + \frac{y_0^2 H^2}{\cos^2\phi} - 2x_0 y_0 H \sin\theta \tan\phi + \\ + 2v_{sw}t_s y_0 H \sin\theta \tan\phi + v_{sw}^2 t_s^2 H^2 - 2x_0 t_s v_{sw} H^2\end{aligned} \tag{3.26}$$

Now, (3.26) is simplified using (3.25), and the following expression is obtained

$$\begin{aligned}2v_{exp}t_s + v_{exp}^2 t_s^2 &= 2v_{sw}t_s y_0 H \sin\theta \tan\phi + v_{sw}^2 t_s^2 H^2 - 2x_0 t_s v_{sw} H^2 \\ \implies x_0 &= \frac{v_{sw}t_s}{2} + \frac{\sin\theta\tan\phi}{H} y_0 - \frac{1}{2H^2}\frac{v_{exp}}{v_{sw}}(v_{exp}t_s - 2R) = \\ &= x_0^{\text{no exp.}} - \frac{1}{2H^2}\frac{v_{exp}}{v_{sw}}(v_{exp}t_s - 2R),\end{aligned} \tag{3.27}$$

where $x_0^{\text{no exp.}}$ coincides with the result obtained without expansion (3.21). The new expression for x_0 in expanding MFRs depends on R, which is not a free parameter of the model. This dependence can be eliminated by substituting the x_0 given by (3.27) in equation (3.23), and solving the resulting equation for R. The expanding CC model represents a more realistic approach to the evolution of ICMEs in the interplanetary space, and therefore could enhance the capability of the model to predict the orientation and physical parameters of MCs.

3.4 Analysis of an event observed by PSP

This section presents an outline of an ICME encountered by Parker Solar Probe (PSP) at 0.547 AU from the Sun on March 15, 2019. The contribution to the comprehensive analysis done in Lario et al. (in review) has consisted of comparing the results of two types of reconstruction techniques for this event, the Graduated Cylindrical Shell (GCS) and the CC model, using the procedures developed by González-Álvarez (2019).

3.4.1 *In situ* measurements

Figure 3.5 displays the ICME *in situ* measurements made by the FIELDS and SWEAP sets of instruments of PSP spacecraft. The black vertical line, located at 08:58 UT on March 15, 2019, indicates the start of the ICME (the so-called *interplanetary shock*, characterized by a remarkable discontinuity of the physical parameters, and followed by the *sheath* period with fluctuations that do not follow any specific pattern). The MC period is delimited by two dashed vertical green lines, and goes from 12:14 UT to 17:45 UT on March 15, 2019. The typical *in situ* signatures of MCs that were listed at the beginning of this chapter are observed: the increase in the average magnetic field strength, the monotonic rotation of the magnetic field direction (mainly in the R-N plane), a low proton temperature, and $\beta_{proton} \ll 1$.

The expansion velocity v_{exp} has also been calculated as indicated in (Nieves-Chinchilla et al., 2018c) with the expression $v_{exp} = (v_s - v_e)/2$, where v_s and v_e are the start and end speeds obtained from a linear fit of the v_{sw} data in the MC interval. The result leads to a negligible value of $v_{exp} = 0.813$ km/s. Another parameter that accounts for the cross-section distortion that occurs in MCs as a result of the interaction with the solar wind is the *distortion parameter* (DiP), defined as the fraction of the MC duration that contains half of the total area accumulated under the magnetic field magnitude curve, such that it satisfies

$$\frac{\int_0^{\text{DiP}\cdot T_d} B(t')\,\mathrm{d}t'}{\int_0^{T_d} B(t')\,\mathrm{d}t'} = 0.5,$$

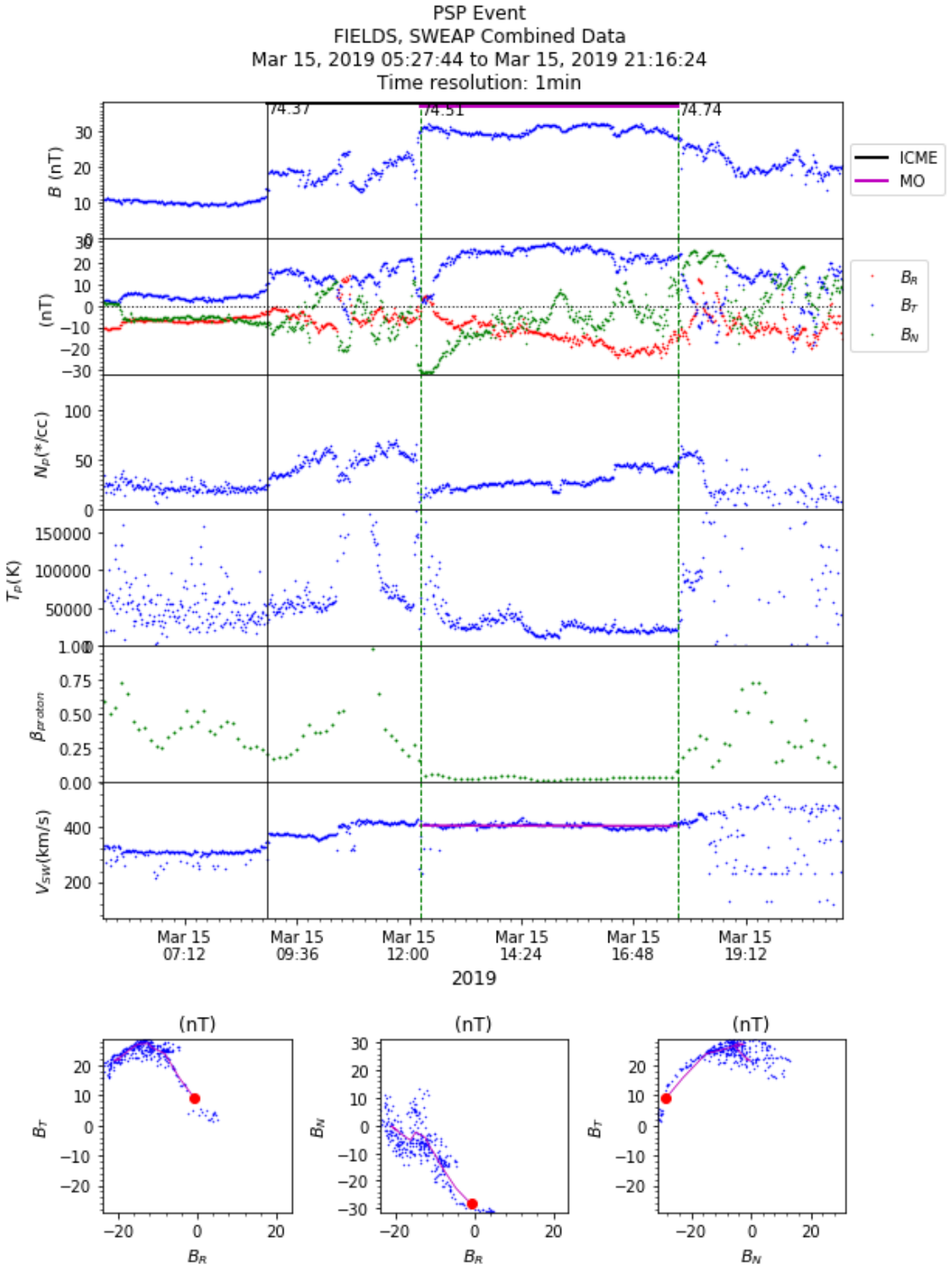

Figure 3.5: *In situ* data of the ICME detected by PSP on March 15, 2019. From top to bottom: magnetic field magnitude, magnetic field components in the RTN coordinate system of the spacecraft, plasma density, proton plasma thermal speed, β_{proton}, and the solar wind bulk velocity (with a pink line that corresponds to the linear fit of v_{sw}). The bottom three panels are *hodograms* that plot the magnetic field RTN components by pairs, with pink lines representing the hourly average of the data, and three dots that correspond to the start time of the MC. Figure generated following the method used in González-Álvarez (2019) adapted to this event.

where T_d is the duration of the whole MC period. In this case, the DiP has a value of 0.507, indicating the presence of a highly symmetric profile characteristic of ideal MFR structures.

3.4.2 Reconstructing the event

The MC *in situ* signatures make this ICME a good candidate for the reconstruction by cylindrical MFR models. Therefore, the CC model (explained in section 3.3) and the elliptical-cylindrical (EC) analytical model (a generalization of the CC model, developed in Nieves-Chinchilla et al., 2018b) have been applied by Lario et al. (in review). The longitude ϕ and tilt θ of the MFR axis when it intercepts PSP has given similar results in both models, $\phi_{CC} = 173^{\circ}$ and $\theta_{CC} = -2^{\circ}$ for the CC model, and $\phi_{EC} = 169^{\circ}, \theta_{EC} = -1^{\circ}$ for the EC model. The impact parameter y_0 ($y_{0CC}/R_{CC} = 0.90$, $y_{0EC}/R_{EC} = 0.80$) shows that PSP intercepts the MC close to its edge, and the radius obtained is rather small ($R_{CC} = 0.0084$ AU, $R_{EC} = 0.0129$ AU). The EC model gives an aspect ratio $\delta = 0.82$ of the elliptical cross section, suggesting that it is slightly distorted with respect to an ideal circular shape.

The Graduated Cylindrical Shell (GCS) model (Thernisien et al., 2009) has also been used in Lario et al. (in review) to reproduce the 3D structure of the ICME using remote sensing observations from SOHO and STEREO A. This model assumes a MFR-like structure of the CME, with conical legs that connect it to the Sun, and a torus-like front edge. The simultaneous observations from two different points of view, as well as the temporal sequence of them, allows the GCS model to provide an estimate of the propagation direction, orientation, height and speed (see Figure 3.6).

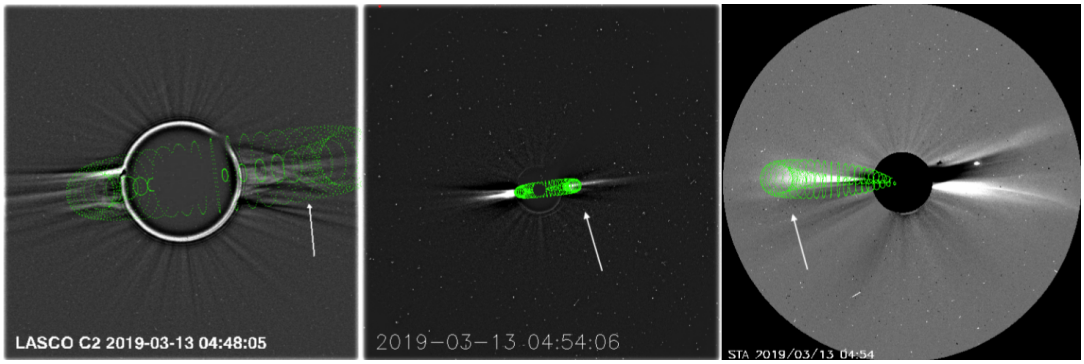

Figure 3.6: GCS modeling results represented as green grids overplotted in coronagraph images. From left to right: LASCO/C2 (covers from 2 to 7 solar radii), LASCO/C3 (covers from 3.7 to 30 solar radii) and STEREO-A/COR-2 (covers from 2.5 to 15.6 solar radii). The first two images were taken at 04:54 UT on March 13, 2019, and the third one, at 04:48 UT on March 13, 2019. The white arrows indicate the main body of the MFRs. Retrieved from Lario et al. (in review).

3.4.3 Comparison of the CC and GCS 3D reconstruction techniques

Figure 3.7 has been generated to simultaneously show the results of the *in situ* EC model and the remote sensing GCS reconstruction, with the aim of evaluating their mutual consistency. It is observed that, under the assumption of a self-similar expansion of the GCS reconstruction, PSP intercepts one of the legs of the structure. In addition, the orientation of the MFR axis given by the EC model is consistent with this interpretation, as seen in Figure 3.7. The main difference between the both reconstruction techniques is in the radius of the MFR: the EC radius ($R_{EC} = 0.0129$ AU) is more than 5 times smaller than the GCS radius ($R_{GCS} = 0.068$ AU at the portion intercepted by PSP).

This discrepancy could be due to the fact that the self-similar expansion assumption is not realistic, since it neglects the interactions of the CME with the ambient solar wind, as well as other processes of expansion, compression, distortion, magnetic forces, and even rotations. The limitation of only having a 1D cut through the CME, inherent in *in situ* reconstruction techniques, could be adding

even more uncertainty. For this particular ICME, it is suggested in Lario et al. (in review) that a high-speed solar wind stream could have interacted with the MC compressing it and thus modifying its shape. Indeed, there are a lot of phenomena in the interplanetary space that could give birth to different expanding regimes of MFRs that strongly differ from the typical self-similar expansion assumption. In section 4.2.4 of the next chapter, various expanding behaviors will be discussed in terms of the occurrence of the kink instability.

This analysis highlights the importance of carrying out studies like Nieves-Chinchilla et al. (2012) or González-Álvarez (2019), since the exploration of the sources that create differences between the various types of reconstruction techniques, can give important clues on CME dynamics and their evolutionary processes. Moreover, the combination of multiview remote sensing observations as well as multipoint *in situ* measurements provide a better perspective and helps in analyzing the consistency of the reconstructed structures.

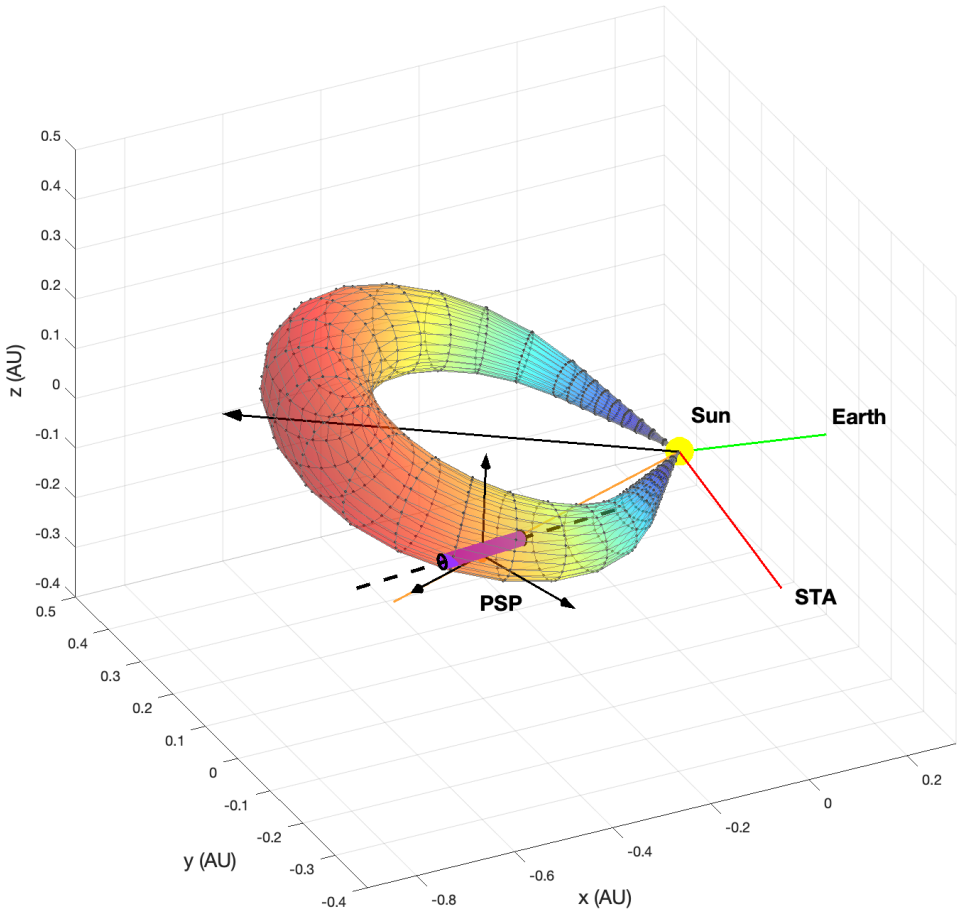

Figure 3.7: The colored hollow croissant structure corresponds to the GCS fit, self-similarly expanded to the distance where the CME intercepts PSP. The purple cylinder is the EC reconstruction of the MC and the black arrows indicate the PSP RTN coordinate system, with PSP located at the center. The dashed straight black line is the axis of the EC MFR. The orange, green and red straight lines show the radial direction towards PSP, Earth and STEREO A, respectively. The long black arrow is the direction of propagation of the nose of the CME as derived by the GCS reconstruction technique. The coordinate system of the figure is HEEQ (the z axis is the solar rotation axis, the x axis is directed from the center of the Sun towards the intersection between the solar equator and its central meridian, and the y axis is chosen to complete the right-handed basis). Figure generated following the method used in González-Álvarez (2019) adapted to this event, as a contribution to the analysis in Lario et al. (in review).

4 . Studying the kink instability of MFR models of CMEs

A numerical method has been developed in this thesis to analyze the helical kink stability of MFRs with different twist distributions, which is based on the theoretical stability analysis in Linton et al. (1996). This chapter presents the methodology and results, and discusses them in relation to the occurrence of rotations, magnetic forces, expansion, reversed chirality, and the shape of the twist profile, among others. The contents of this part of the chapter have been accepted in Solar Physics and will be published shortly (Florido-Llinas et al., in review). Finally, the numerical procedure for the linear stability analysis has been applied to obtain optimal parameters in nonlinear MHD simulations, which will be used by Mark George Linton and Kalman Knizhnik at NRL for ongoing research about the emergence of MFRs in the Sun.

4.1 Methodology

4.1.1 Magnetic field configuration

This method can be applied to any MFR model that assumes an axially symmetric cylindrical magnetic configuration, with cross-sectional radius R. The non-force-free CC model has been chosen because it has the ability to model various types of magnetic forces, as well as different twist distributions that increase along the radius of the MFR. Although the real twist profile of MFRs is still unknown (as explained in section 3.2.3), its increasing behavior has been supported by observations (Lanabere et al., 2020) and eruption theory (Démoulin et al., 2019). The extensively used force-free Lundquist and Gold-Hoyle (GH) models will also be employed.

As explained in section 3.3, the CC model assumes a generic polynomial expansion of the current density $\mathbf{j}$. We will adopt here the most usual approach, in which the series is truncated to a single term $\alpha_n r^n$ for j_φ, and $\beta_m r^m$ for j_y. New variables are defined in terms of the original ones in Eq. (3.12),

$$\tau = B_y^0 \Big/ \left(\mu_0 \alpha_n \frac{1}{n+1} R^{n+1}\right), \quad \tilde{C}_{nm} = -\frac{m+2}{n+1}\frac{\alpha_n}{\beta_m} R^{n-m}, \quad \bar{r} = r/R,$$

and the magnetic field components can be rewritten as

$$\begin{cases} B_r = 0 \\ B_y = B_y^0 \left(1 - \dfrac{1}{\tau}\bar{r}^{n+1}\right) \\ B_\varphi = \dfrac{B_y^0}{\tau \tilde{C}_{nm}} \bar{r}^{m+1} \end{cases} . \tag{4.1}$$

To avoid a singularity in the axis, the conditions $n \geq 1$ and $m \geq 0$ must be fulfilled ($\lim_{r\to 0} B_\varphi(r) = 0$ and $\lim_{r\to 0} j_\varphi(r) = 0$). In this thesis, the cases $[n, m] \in \{[1, 0], [2, 1], [3, 2], [1, 1]\}$ will be analyzed. The magnetic field equations for each particular case are given in the second column of Table 4.1. The goal will be to find the range of parameters τ and $\tilde{C}_{nm}$ for which the system is kink unstable

for each pair $[n, m]$. The intervals $\tau \in [0.0, 4.0]$ and $\tilde{C}_{nm} \in [0.5, 2.0]$ will be studied since CC fittings often use parameters inside of these ranges.

On the other hand, the Lundquist and GH models (introduced in section 3.1.2) are parametrized as functions of α and q (see Table 4.1). The aim will be to find α and q for which the system is kink stable.

Model	**B**	$\mathbf{Q} = \frac{\mathbf{B}_\varphi}{\mathbf{r}\mathbf{B}_\mathbf{y}}$	$\sin \mathbf{\Omega}$
CC $[1,0]$	$\begin{cases} B_y = B_y^0 \left(1 - \frac{1}{\tau}\bar{r}^2\right) \\ B_\varphi = \frac{B_y^0}{\tau \tilde{C}_{10}} \bar{r} \end{cases}$	$\frac{1}{\tilde{C}_{10} R(\tau - \bar{r}^2)}$	$\frac{\bar{r}\left(\tau - \bar{r}^2 - \frac{1}{\tilde{C}_{10}^2}\right)}{\left[(\tau - \bar{r}^2)^2 + \frac{\bar{r}^2}{\tilde{C}_{10}^2}\right]^{\frac{1}{2}} \left[\bar{r}^2 + \frac{1}{\tilde{C}_{10}^2}\right]^{\frac{1}{2}}}$
CC $[2,1]$	$\begin{cases} B_y = B_y^0 \left(1 - \frac{1}{\tau}\bar{r}^3\right) \\ B_\varphi = \frac{B_y^0}{\tau \tilde{C}_{21}} \bar{r}^2 \end{cases}$	$\frac{\bar{r}}{\tilde{C}_{21} R(\tau - \bar{r}^3)}$	$\frac{\bar{r}\left(\tau - \bar{r}^3 - \frac{\bar{r}}{\tilde{C}_{21}^2}\right)}{\left[(\tau - \bar{r}^3)^2 + \frac{\bar{r}^4}{\tilde{C}_{21}^2}\right]^{\frac{1}{2}} \left[\bar{r}^2 + \frac{1}{\tilde{C}_{21}^2}\right]^{\frac{1}{2}}}$
CC $[3,2]$	$\begin{cases} B_y = B_y^0 \left(1 - \frac{1}{\tau}\bar{r}^4\right) \\ B_\varphi = \frac{B_y^0}{\tau \tilde{C}_{32}} \bar{r}^3 \end{cases}$	$\frac{\bar{r}^2}{\tilde{C}_{32} R(\tau - \bar{r}^4)}$	$\frac{\bar{r}\left(\tau - \bar{r}^4 - \frac{\bar{r}^2}{\tilde{C}_{32}^2}\right)}{\left[(\tau - \bar{r}^4)^2 + \frac{\bar{r}^6}{\tilde{C}_{32}^2}\right]^{\frac{1}{2}} \left[\bar{r}^2 + \frac{1}{\tilde{C}_{32}^2}\right]^{\frac{1}{2}}}$
CC $[1,1]$	$\begin{cases} B_y = B_y^0 \left(1 - \frac{1}{\tau}\bar{r}^2\right) \\ B_\varphi = \frac{B_y^0}{\tau \tilde{C}_{11}} \bar{r}^2 \end{cases}$	$\frac{\bar{r}}{\tilde{C}_{11} R(\tau - \bar{r}^2)}$	$\frac{\tau - \bar{r}^2\left(1 + \frac{3}{2\tilde{C}_{11}^2}\right)}{\left[(\tau - \bar{r}^2)^2 + \frac{\bar{r}^4}{\tilde{C}_{11}^2}\right]^{\frac{1}{2}} \left[1 + \frac{1}{\tilde{C}_{11}^2}\right]^{\frac{1}{2}}}$
Lund.	$\begin{cases} B_y = B_y^0 J_0(\alpha \bar{r}) \\ B_\varphi = B_y^0 J_1(\alpha \bar{r}) \end{cases}$	$\frac{J_1(\alpha \bar{r})}{R \bar{r} J_0(\alpha \bar{r})}$	0
GH	$\begin{cases} B_y = \frac{B_y^0}{1 + q^2 \bar{r}^2} \\ B_\varphi = \frac{q \bar{r} B_y^0}{1 + q^2 \bar{r}^2} \end{cases}$	$\frac{q}{R}$	0

Table 4.1: Magnetic field, twist and misalignment equations (see Eq. (4.3) for the definition of the force-free measure given by the misalignment $\sin \Omega$).

Figure 4.1a shows the normalized CC magnetic field components B_y (in red) and B_φ (in black) along the normalized radius of the MFR, for $\tau = 1.0$ and $\tilde{C}_{nm} = 1.0$. The axial magnetic field B_y is set to B_y^0 in the core and decreases towards the boundary of the MC by an amount that depends on the parameter τ: it vanishes there if $\tau = 1$, becoming negative when $\tau < 1$ or closer to B_y^0 if $\tau > 1$. The azimuthal component B_φ is zero in the axis and grows towards the outer edge with a rate of change that is inversely proportional to $\tilde{C}_{nm}$ and τ.

Figure 4.1b and 4.1c show the Lundquist and GH magnetic fields for $\alpha = 2.4, 3.4$ and $q = 1.0, 2.0$, respectively. In fact, varying α in the Lundquist model only squeezes or stretches the horizontal axis, and so it indicates where the cutoff point of the Bessel functions is taken as the MFR outer radius. The GH model behaves similarly. For both models, increasing α or q generally entails a bigger difference between B_y in the core and the boundary. For the Lundquist case, B_y becomes negative when $\alpha > 2.4$. In the GH model, B_y stays always positive.

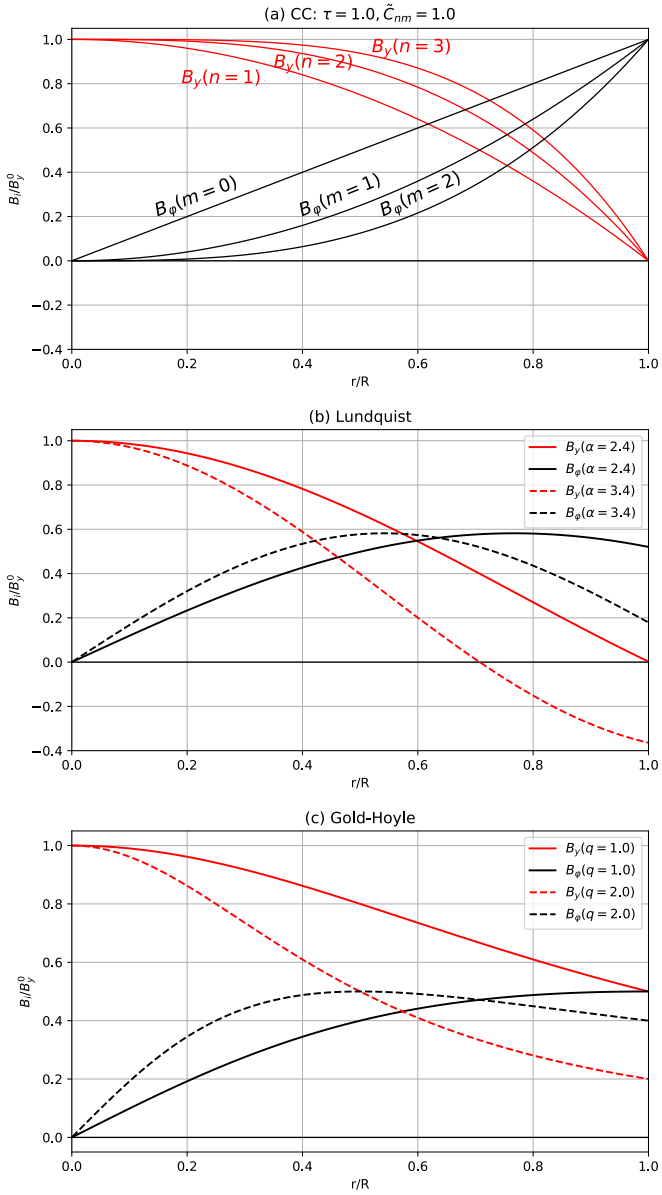

Figure 4.1: Axial and poloidal magnetic field components of (a) the CC model for $[n, m] = [1, 0], [2, 1], [3, 2], [1, 1]$ with parameters $\tau = 1.0, \tilde{C}_{nm} = 1.0$; (b) the Lundquist model for $\alpha = 2.0, 3.0$; (c) the GH model for $q = 1.0, 2.0$.

4.1.2 Twist or helical pitch

The *twist* Q was defined in section 3.2.1 as the wavenumber measuring the angle covered by magnetic field lines per unit length, given by

$$Q = \frac{B_\varphi}{rB_y}, \tag{4.2}$$

and its particular expression for each of the models under study is given in the third column of Table 4.1, which shows that Q is inversely proportional to the MFR cross-sectional radius R.

Figure 4.2a shows the behavior of the product RQ in the CC model, along the normalized radius, for parameters $\tau = 1.5$ and $\tilde{C}_{nm} = 0.5$. For the cases of the form $[n, 0]$, Q adopts the finite value of $1/(\tilde{C}_{n0}R\tau)$ in the core, while it vanishes for the rest of them. Then, it increases towards the

boundary reaching a value that depends on τ: if $\tau = 1$ it goes to infinity in the edge; if $\tau < 1$ the twist becomes infinite at an internal point of the MFR ($\bar{r} = \tau$) and then reverses its sign causing the chirality to change; and if $\tau > 1$, the twist goes to $1/(\tilde{C}_{nm} R(\tau - 1))$ at the edge.

The CC model twist Q is inversely proportional to $\tilde{C}_{nm}$ and R. Its profile decreases with increasing τ and adopts a more uniform shape, so that it is constant to 0 in the limit $\tau \to \infty$. Moreover, for the cases $[k+1, k]$, larger k implies a smaller growth rate of the twist around the core, thus adopting more of a *stage-like* distribution, or in other words, an MFR with a twist distribution around the core that is different from the one in its outer shell (in this case, it would be almost uniform in the core, and abruptly increase close to the boundary).

Figure 4.2b displays in blue the quantity RQ in Lundquist model for $\alpha = 2.4, 3.4$. It has an increasing profile, growing towards a finite value in the boundary if $\alpha < 2.4$ and to infinity if $\alpha = 2.4$. When $\alpha > 2.4$ there is a change in the chirality of the MFR that occurs at $\bar{r} = 2.4/\alpha$. Figure 4.2b also shows in orange the product RQ of GH model for $q = 1.0, 2.0$; indeed, Gold-Hoyle MFRs are uniformly twisted along their cross-sectional radius.

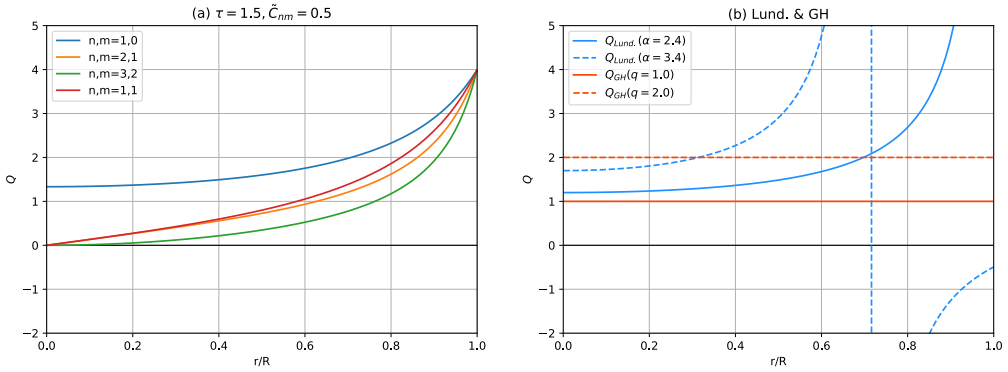

Figure 4.2: Measurement of RQ along the flux rope radius for (a) CC $[n, m] = [1, 0], [2, 1], [3, 2], [1, 1]$ with parameters $\tau = 1.5, \tilde{C}_{nm} = 0.5$; (b) the Lundquist model (in blue) for $\alpha = 2.4$ (continuous) and 3.4 (dashed), and the GH model (in orange) for $q = 1.0$ (continuous) and $q = 2.0$ (dashed).

4.1.3 Misalignment between j and B

An MFR is said to be *force-free* (FF) if the magnetic field is completely aligned with the current density, $\mathbf{j} \times \mathbf{B} = 0$. A measure of the *force-freeness* for the CC model (Eq. (4.1)) is given by the misalignment between $\mathbf{j}$ and $\mathbf{B}$,

$$\begin{aligned} \sin\Omega &= \frac{(\mathbf{j}\times\mathbf{B})|_r}{|\mathbf{j}||\mathbf{B}|} \\ &= \frac{\bar{r}^n(\tau - \bar{r}^{n+1}) - \frac{m+2}{n+1}\frac{\bar{r}^{2m+1}}{\tilde{C}_{nm}^2}}{\left[(\tau - \bar{r}^{n+1})^2 + \frac{1}{\tilde{C}_{nm}^2}\bar{r}^{2(m+1)}\right]^{\frac{1}{2}}\left[\bar{r}^{2n} + \frac{1}{\tilde{C}_{nm}^2}\bar{r}^{2m}\right]^{\frac{1}{2}}}. \end{aligned} \tag{4.3}$$

The configuration is purely FF in the core ($\sin\Omega = 0$ at $\bar{r} = 0$) for the cases with $n > m$. Lundquist and GH models predict MFRs that are completely FF inside. In particular, Lundquist model is a constant-α or linear FF field, while GH is a non-linear FF model (as explained in section 3.1.2).

The criterion used in the present work to establish if a MFR model that allows the presence of magnetic forces, is FF or not, at a particular $\bar{r}$, is given in Nieves-Chinchilla et al. (2016):

- If $\sin\Omega > 0.3$ ($\Omega > 18°$): non-force-free (NFF), with the Lorentz force pointing outwards.
- If $|\sin\Omega| < 0.3$ ($|\Omega| < 18°$): FF.
- If $\sin\Omega < -0.3$ ($\Omega < -18°$): NFF, Lorentz force pointing inwards.

Figure 4.3 displays how the misalignment $\sin\Omega$ between $\mathbf{j}$ and $\mathbf{B}$ varies along the radius and with the parameter $\tilde{C}_{nm}$, for different pairs $[n, m]$ and τ. Three planes corresponding to $\sin\Omega = -0.3, 0, 0.3$ are shown in each of them.

In general, it can be observed that smaller $\tilde{C}_{nm}$ makes the structure inward-NFF in the vicinity of the boundary, while bigger $\tilde{C}_{nm}$ makes it be outward-NFF in the middle and outer sections. The first three panels in Figure 4.3 show how the misalignment changes in the case $[1, 0]$ as τ is increased: larger τ makes the structure be more FF (for small $\tilde{C}_{nm}$) or outward-NFF towards the edge (for big $\tilde{C}_{nm}$), and the inward-NFF behavior disappears. This is valid for the rest of $[n, m]$. The case $[1, 1]$ (see Figure 4.3f) has been included in the analysis because it is outward-NFF in the core, while the ones of the form $[k+1, k]$ are FF in the axis and become slightly more outward-NFF in the mid and outer sections as k is increased (see Figure 4.3b, 4.3d, 4.3e for fixed $\tau = 2.0$).

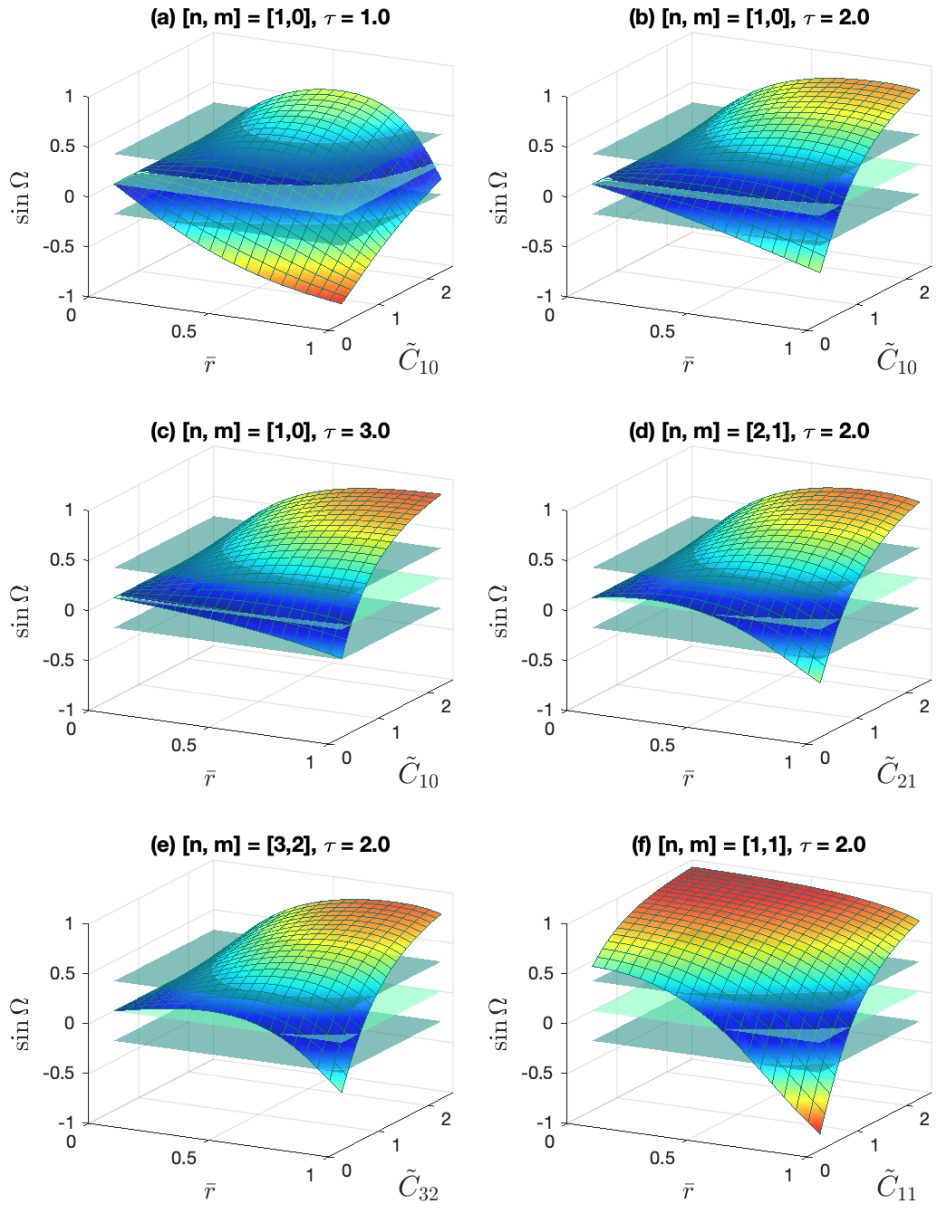

Figure 4.3: Plots of the misalignment $\sin\Omega$ in function of the normalized radius and the parameter $\tilde{C}_{nm}$. (a), (b) and (c) show the variation of $\sin\Omega$ with increasing τ for $[1, 0]$. (b), (d) and (e) show how $\sin\Omega$ changes when k in $[k + 1, k]$ is increased for constant $\tau = 2.0$. The outward-NFF behavior of the case [1, 1] in the core is displayed in (f).

4.1.4 CC model parameters in expanding MFRs

In the ICME journey throughout the heliosphere, the relative magnetic helicity H_r and magnetic fluxes ϕ_y, ϕ_φ are conservative quantities if there is no erosion or reconnection with the ambient solar wind. The expressions for these physical quantities for the general CC model were given in section 3.3.2. They can be rewritten in terms of the CC cases and parameters adopted in this chapter as

$$\begin{aligned}
\phi_y &= \pi R^2 B_y^0 \left[1 - \frac{2}{(n+3)\tau}\right] \\
\phi_\varphi &= LR \frac{B_y^0}{(m+2)\tau \tilde{C}_{nm}} \\
\frac{H_r}{L} &= \frac{4\pi R^3 (B_y^0)^2}{\tau \tilde{C}_{nm}} \left[\frac{1}{2(m+4)} - \frac{1}{(n+3)(m+n+5)\tau}\right],
\end{aligned}$$

where the relative helicity H_r is expressed per unit length. The MFR expands from a radius R to R' and from an axial length L to L'. The CC parameters when the MFR has radius R ($\tau, \tilde{C}_{nm}$ and B_y^0) are known. The aim is to find the parameters $\tau', \tilde{C}'_{nm}$ and $B_y^{0\prime}$ of the MFR when it expands to a radius R' and axial length L', in terms of $\tau, \tilde{C}_{nm}$ and B_y^0. This is achieved by making equal the magnetic fluxes and the relative helicity at the two evolutionary stages: $\phi_y = \phi'_y, \phi_\varphi = \phi'_\varphi$ and $H_r = H'_r$. Isolating $1/\tau'$ in $\phi_y = \phi'_y$, one obtains

$$\frac{1}{\tau'} = \frac{n+3}{2} + \frac{B_y^0}{B_y^{0\prime}} \left(\frac{R}{R'}\right)^2 \left[\frac{1}{\tau} - \frac{n+3}{2}\right], \tag{4.4}$$

and $\phi_\varphi = \phi'_\varphi$ gives

$$\frac{\tilde{C}'_{nm}}{\tilde{C}_{nm}} = \frac{L'}{L}\frac{R'}{R}\frac{B_y^{0\prime}}{B_y^0}\frac{\tau}{\tau'} \tag{4.5}$$

Substituting Eq. (4.4) and (4.5) in $H_r = H'_r$, the final results are

$$\begin{cases}
B_y^{0\prime} = \left(\dfrac{R}{R'}\right)^2 B_y^0 \\
\tau' = \tau \\
\tilde{C}'_{nm} = \dfrac{L'}{L}\dfrac{R}{R'}\tilde{C}_{nm}
\end{cases}. \tag{4.6}$$

Therefore, upon expansion, τ remains constant (i.e. the ratio of B_y in the core to its value in the boundary does not change), B_y^0 decreases in a way inversely proportional to $(R')^2$, and $\tilde{C}_{nm}$ can increase or decrease depending on the relation between L'/L and R'/R. In terms of the magnetic field components and twist,

$$\begin{cases}
B'_y = \left(\dfrac{R}{R'}\right)^2 B_y \\
B'_\varphi = \dfrac{R}{R'}\dfrac{L}{L'} B_\varphi \\
Q' = \dfrac{L}{L'} Q
\end{cases}$$

which implies that the twist will decrease if the MFR axial length increases.

4.1.5 Linear stability analysis

The method to study the kink instability was explained in section 2.3. Here we only summarize the final equations and stability criteria that have been used for the numerical stability analysis. The plasma is perturbed by an arbitrarily small perturbation $\boldsymbol{\xi}(\mathbf{r}, t)$ from a stationary equilibrium. In the normal mode approach, a temporal dependence of $\boldsymbol{\xi}(\mathbf{r}, t) = \boldsymbol{\xi}(\mathbf{r}) e^{i\omega t}$ is assumed. The unknown

Lagrange multiplier λ of the generalized energy $U = W + \lambda K$ is related to the temporal frequency ω through $\lambda = -4\pi\rho_0\omega^2$, where ρ_0 is the equilibrium density of the plasma. In the study of the kink instability, the eigenfunctions $\boldsymbol{\xi}(\mathbf{r})$ have helical symmetry with wavenumber k and arbitrary radial structure, $\boldsymbol{\xi}(\mathbf{r}) = [\xi_r(r), \xi_y(r), \xi_\varphi(r)]e^{i(ky+\varphi)}$. Then, the perturbation that minimizes the generalized energy of the system can be obtained from the radial component ξ_r given by Euler-Lagrange equation

$$\frac{\mathrm{d}}{\mathrm{d}r}\left(f\frac{\mathrm{d}\xi_r}{\mathrm{d}r}\right) - g\xi_r = 0, \tag{4.7}$$

where f and g are defined as

$$f = \frac{r^3(\lambda + \left(kB_y + \frac{B_\varphi}{r}\right)^2}{1 + k^2r^2}, \tag{4.8}$$

$$g = \frac{k^2 r}{1 + k^2r^2}\left[r^2\left\{\lambda + \left(kB_y + \frac{B_\varphi}{r}\right)^2\right\} - r\frac{\mathrm{d}|\mathbf{B}(r)|^2}{\mathrm{d}r}\right. \tag{4.9}$$

$$\left. -2B_\varphi^2\left\{\frac{2\left(kB_y + \frac{B_\varphi}{r}\right)^2}{\lambda + \left(kB_y + \frac{B_\varphi}{r}\right)^2} - 1\right\} + \frac{2}{1 + k^2r^2}(r^2\lambda + k^2r^2B_y^2 - B_\varphi^2)\right]. \tag{4.10}$$

The boundary conditions $\dot{\xi}_r(0) = 0$ and $\xi_r(0) = \xi_0$ (ξ_0 can be set to 1 without loss of generality) ensure regularity at the origin. The imposition of the continuity of the total pressure across the free boundary of the MFR, with no external field, gives the dispersion relation for λ,

$$D(\lambda; R, k) = \left[k^2|\mathbf{B}(R)|^2 + \lambda + \lambda\frac{(1 + k^2R^2)K_1(|k|R)}{|k|RK_0(|k|R) + K_1(|k|R)}\right]\xi_r(R) + \left\{R\lambda + R\left(kB_y + \frac{B_\varphi}{r}\right)^2\right\}\dot{\xi}_r(R) = 0, \tag{4.11}$$

where K_0 and K_1 are modified Bessel functions. As stated in section 2.3.3, a circular-cylindrical MFR with given R and $\mathbf{B}_0(r)$ is said to be kink stable if it is stable to perturbations of any wavenumber k, so a necessary and sufficient condition for kink stability is that the largest λ for which the dispersion relation in Eq. (4.11) holds is negative for all k.

4.1.6 Numerical method for the linear stability analysis

Given a particular pair $[n, m]$ defining the magnetic equilibrium $\mathbf{B}_0(r)$ for the CC model, the purpose of the numerical procedure that has been developed in Python is to find the value of τ for each $\tilde{C}_{nm}$ above which the system becomes kink stable to perturbations of any wavenumber k, called τ_{crit}. The intervals of interest are $\tau \in [0.0, 4.0]$ and $\tilde{C}_{nm} \in [0.5, 2.0]$ because CC fittings use parameters that are usually inside of these ranges. An outline of the numerical method is presented in this section.

For a particular pair of $\tilde{C}_{nm}$ and τ, the main subroutine of the code uses Brent's method (Brent, 2013) to find the zeros of the dispersion relation (4.11). This root-finding algorithm has been chosen because it has the reliability of the bisection method, given an appropriately chosen bracketing interval $[\lambda_0, \lambda_1]$ ($D(\lambda_0; R, k)D(\lambda_1; R, k) < 0$), an it is able to potentially converge to the zero λ_f in the interval as fast as the secant method.

After the first zero λ_f has been found, k is changed to $k+\Delta k$ for a sufficiently small Δk. An interval $[\lambda_f - L, \lambda_f + L]$ is defined around λ_f, and subdivided into a specific number N of subintervals. Starting from above (because we want to find the biggest zero λ, which corresponds to the most unstable mode), the new subintervals are inspected until a bracketing interval is found, such that the function D has opposite signs at both ends of it (i.e., it is checked if $D(\lambda_f + L - 2L/N; R, k +$

$\Delta k)D(\lambda_f + L; R, k + \Delta k) < 0$. If not, then it is checked if $D(\lambda_f + L - 4L/N; R, k + \Delta k)D(\lambda_f + L - 2L/N; R, k + \Delta k) < 0$, and so on). Brent's method is applied in the new bracketing interval to find the precise zero for $k + \Delta k$. The process is repeated varying k until no positive zero of the dispersion relation can be found. The main output parameters of this subroutine are:

- k_{min}, the minimum k for which the largest λ that solves $D(\lambda; R, k) = 0$ is positive.
- k_{max}, the maximum k for which the largest λ that solves $D(\lambda; R, k) = 0$ is positive.
- k_{ext}, the wavenumber k for which the most unstable mode occurs.
- λ_{ext}, the most unstable mode occurring for the wavenumber k_{ext}, such that $\lambda_{ext} = \max\{\lambda > 0 \mid \exists k \text{ s.t. } D(\lambda; R, k) = 0\}$.

Each evaluation of $D(\lambda; R, k)$ requires solving Euler-Lagrange equation to obtain $\xi_r(R), \dot{\xi}_r(R)$, and this has been implemented with `odeint` Python routine (source code from Oliphant), which applies LSODA algorithm for differential equations. The problem is actually solved for the dimensionless quantities $\tilde{\lambda} = \lambda R^2/(B_y^0)^2$, $\tilde{k} = kR$, $\bar{r} = r/R$ and $\tilde{\mathbf{B}} = \mathbf{B}/B_y^0$.

For fixed τ and $\tilde{C}_{nm}$, the program needs a first rough guess of $\tilde{k}_{min}$, $\tilde{k}_{max}$, and also the largest zero of $D(\tilde{\lambda}; 1, \tilde{k})$ only for one arbitrary value of $\tilde{k}$. The output consists of the precise values of $\tilde{k}_{min}$, $\tilde{k}_{max}$, $\tilde{k}_{ext}$ and $\tilde{\lambda}_{ext}$. The first approximations of the aforementioned parameters are provided by graphical inspection for some values of $\tilde{C}_{nm}$ and τ, and the process is then automatized to find them by interpolation of the partial results.

Therefore, for each given $\tilde{C}_{nm}$, the program outputs $\tilde{k}_{min}, \tilde{k}_{max}, \tilde{k}_{ext}, \tilde{\lambda}_{ext}$ for a desired number n of points in the range of $\tau \in [0.0, 4.0]$. Next, a decreasing exponential function is fitted to $\tilde{\lambda}_{ext}$ as a function of τ ($\tilde{\lambda}_{ext}(\tau) = \alpha e^{\beta\tau} + \gamma$, with $\alpha, \beta, \gamma \in \mathbb{R}$). The criterion chosen to define the τ_{crit} above which the system becomes kink stable is to locate the τ at which the fitted function becomes 0. This process is repeated to find τ_{crit} as a function of $\tilde{C}_{nm}$, for $\tilde{C}_{nm} \in [0.5, 2.0]$

The procedure can be restricted to the variation of a single parameter in order to study the kink instability of the Lundquist and GH models in terms of α or q, respectively. Moreover, the radial perturbation ξ_r that solves Euler-Lagrange equation (4.7) can be computed to get more insight into the behavior of the instability. Any other desired cylindrically symmetric magnetic profile can also be analyzed with this method.

4.2 Results and discussion of the stability analysis of MFRs

Figure 4.4 shows the results of the numerical analysis explained in section 4.1.6 for the CC model. The points correspond to the minimum $\tilde{C}_{nm}$ above which the system becomes kink stable for each τ, for the different cases $[n, m]$. The linear stability analysis of the Lundquist magnetic profile has resulted in a stability threshold of $\alpha_{crit} = 3.2$, so $\alpha < \alpha_{crit}$ implies that the system is kink stable. Likewise, the uniformly-twisted Gold-Hoyle model is kink stable if $q < q_{crit}$, with $q_{crit} = 1.2$.

It is observed in Figure 4.4 that, for the CC cases studied, big values of τ and $\tilde{C}_{nm}$ are likely to be kink stable, since they make the twist Q decrease, and $\tau < 1$ implies instability. Lundquist and GH models are kink stable for small α or q. Moreover, among the cases $[k+1, k]$ analyzed, Figure 4.4 shows that $[1, 0]$ is less stable than $[k+1, k]$, for $k \geq 1$, while it is also the only case for which the twist vanishes at $r = 0$ (see Figure 4.2). This suggests that the presence of twist close to the axis could have a kink destabilizing effect.

A modified Weibull distribution (Rinne, 2009) has been fitted to each of the analyzed CC cases, with parameter $\gamma = 1$ in the expression

$$\tilde{C}_{nm}(\tau) = \frac{\rho\beta}{\eta}\left(\frac{\tau - \gamma}{\eta}\right)^{\beta-1} e^{-\left(\frac{\tau-\gamma}{\eta}\right)^{\beta}}, \tag{4.12}$$

where the fitted values of β, η, ρ for each $[n, m]$ are shown in Table 4.2. The adjusted functions are plotted in Figure 4.4 as dashed lines. They provide a good estimate of the stability limit curve for

Model	Stability range
CC $[1,0]$	$\tilde{C}_{10} > \tilde{C}_{10,crit}(\tau) =$ (Eq. (4.12) with $\gamma = 1, \beta = 0.8400, \eta = 5.7, \rho = 5.6382$)
CC $[2,1]$	$\tilde{C}_{21} > \tilde{C}_{21,crit}(\tau) =$ (Eq. (4.12) with $\gamma = 1, \beta = 0.8400, \eta = 5.7, \rho = 4.7935$)
CC $[3,2]$	$\tilde{C}_{32} > \tilde{C}_{32,crit}(\tau) =$ (Eq. (4.12) with $\gamma = 1, \beta = 0.8400, \eta = 5.7, \rho = 4.3101$)
CC $[1,1]$	$\tilde{C}_{11} > \tilde{C}_{11,crit}(\tau) =$ (Eq. (4.12) with $\gamma = 1, \beta = 0.8032, \eta = 5.8, \rho = 6.1000$)
Lund.	$\alpha < \alpha_{crit} = 3.2$
GH	$q < q_{crit} = 1.2$

Table 4.2: Summary of the kink stability thresholds obtained.

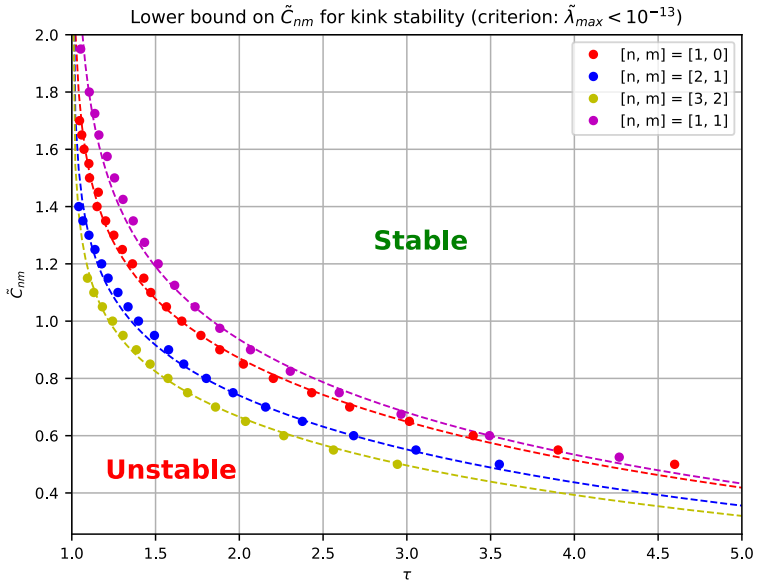

Figure 4.4: Plot of the points and the fitted Weibull distributions (dashed lines) symbolizing the boundary values of $\tilde{C}_{nm}$ at fixed τ between the stable and unstable regimes of the MFR.

$\tau \in [1.0, 4.0]$. It is clearly seen that $[1,1]$ shows the smallest stability range, while the cases of the form $[k+1, k]$ become increasingly stable to kink as k increases. Future exploration of more $[n,m]$ cases could provide an expression relating the fitted parameters with the n, m values considered.

The results obtained can now be compared to well-known thresholds for the kink instability of MFRs that already exist in the literature. They are usually given in terms of the critical total twist angle, Φ_{crit}, which is related to the twist Q by $\Phi = QL$ (L is the MFR axial length).

- The values Φ_{crit} found in the present work depend on the aspect ratio $\frac{L}{R}$, since Q is inversely proportional to R in all cases, as can be seen in Table 4.1. Dungey and Loughhead (1954) studied a uniformly twisted infinite MFR in an incompressible plasma, considering B_y constant, $B_\varphi = Ar$ ($A \in \mathbb{R}$), and uniform twist $Q = A/B_y$. They showed analytically that $\Phi_{crit} = 2\frac{L}{R}$. Here, the uniformly-twisted GH model has been found to predict less stable MFRs, with lower $\Phi_{crit} = q_{crit}\frac{L}{R} = 1.2\frac{L}{R}$. The numerical method developed could be applied to the magnetic field of Dungey and Loughhead (1954) to check that the same result is obtained, and further exploration of the differences between the two models could provide more insight into the physical properties that destabilize MFRs.

- Hood and Priest (1981) found the well-known threshold of $\Phi_c = 2.5\pi$ for line-tied MFRs described by the GH model. A MFR is said to be *line-tied* when its two footpoints are anchored in the photosphere, so one needs to impose that the perturbation $\boldsymbol{\xi}$ vanishes there. Indeed, laboratory experiments resembling solar line-tied MFRs were carried out (Myers et al., 2015), and the same critical twist was obtained. Therefore, the threshold does not depend on the aspect ratio $\frac{L}{R}$ for line-tied MFRs (instead, we found $\Phi_{crit} = 1.2\frac{L}{R}$).

- The constant-α FF Lundquist has given a stability threshold of $\alpha_{crit} = 3.2$ in this work, assuming a free boundary of the structure. Instead, Voslamber and Callebaut (1962) considered a MFR enclosed by a perfectly conducting rigid wall, and obtained a very similar result, $\alpha_{crit} = 3.176$. This suggests that the two types of boundary conditions do not have any significant physical effect on the onset of the kink instability, but this issue should be independently studied in depth in future research.

4.2.1 Rotations and the kink instability

The kink instability is already regarded as a possible explanation for the rotation of emerging MFRs in the photosphere (see Figure 4.5), since it makes the axis of the twisted structure become a helix itself. However, this process has not yet been sufficiently explored to account for rotations in the lower-middle corona and heliosphere that are sometimes observed.

As stated in Florido-Llinas et al. (in review), the accumulation of poloidal magnetic flux during the first stages of the evolution of a CME could modify the internal twist distribution and physical parameters of the MFR, and this change could drive the onset of kink instabilities that would be seen as rotations in remote sensing coronagraphs (Vourlidas et al., 2011; Nieves-Chinchilla et al., 2012). This contrasts with the phenomenon that is commonly referred to as CME *deflection*, which also displays rotation signatures but is caused solely by the interaction with the ambient solar wind, and not from internal physical processes such as the kink instability. On this matter, nonlinear simulations should be done in each case to study how the instabilities evolve in the long run and whether they are consistent with observations.

The critical twists of Table 4.2 could be used along with observational studies in order to infer which MFRs are susceptible to rotate. For example, the study made by Wang et al. (2016) on 126 MCs of Lepping's list (Lepping et al., 2006) with the velocity-modified GH model showed that interplanetary MFRs have a total twist angle Φ bounded by $0.2\frac{L}{R} < \Phi < 2\frac{L}{R}$ with an average

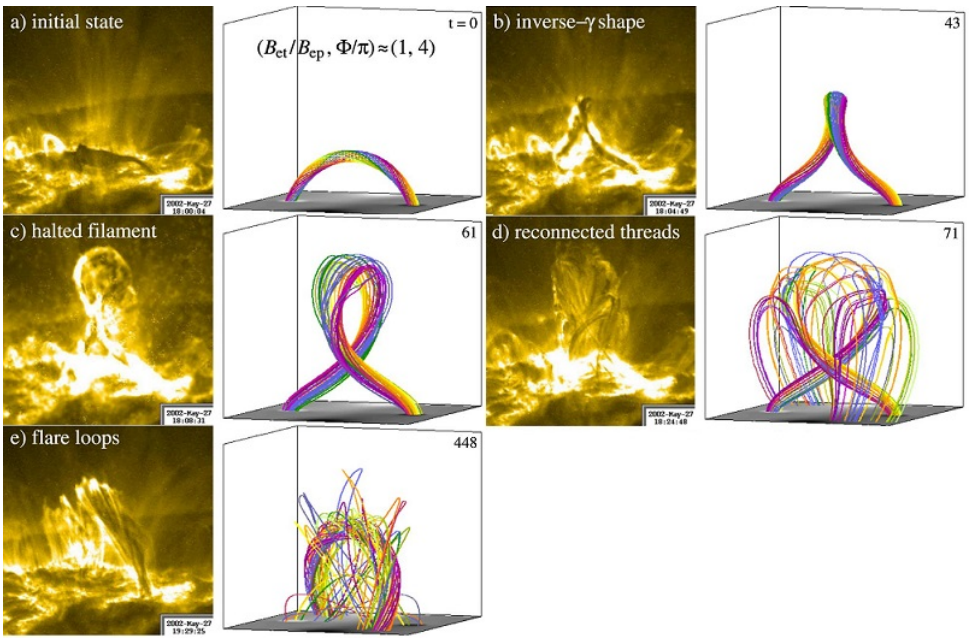

Figure 4.5: Graphical representation of the characteristic stages of a confined filament eruption on May 27, 2002, observed by TRACE (Transition Region and Coronal Explorer). The actual remote sensing measurements (left side of each panel) are compared to a parametric MHD simulation (right side). The kink instability deforms the axis of the emerging MFR, until reconnection occurs with the ambient field lines in panel (d), creating a coronal loop as the final result in panel (e). Retrieved from Hassanin and Kliem (2016).

of $\Phi = 0.6\frac{L}{R}$. The GH threshold found in the present work, $\Phi_c = q_{crit}\frac{L}{R} = 1.2\frac{L}{R}$, denotes that interplanetary MFRs are kink stable on average, but there are a large amount of events with $1.2\frac{L}{R} < \Phi < 2\frac{L}{R}$ that would still be unstable. Further study of these MFRs and of possible signatures of rotation would allow us to gain better insight into the relation between rotations and the occurrence of the kink instability in the interplanetary medium, as well as physically meaningful constraints on MFR models with multiple free parameters.

4.2.2 Magnetic forces and the kink instability

While the inside of Lundquist and GH MFRs is completely FF, the misalignment between $\mathbf{j}$ and $\mathbf{B}$ for the CC model showed different behaviors depending on the pair $[n, m]$ and the parameters $\tilde{C}_{nm}, \tau$, as seen in Figure 4.3. This raises the question of whether there exists any relation between the magnetic forces that act on an MFR and the occurrence of kink instabilities.

For example, the CC $[1, 1]$ case presents a smaller stability range than the cases $[k + 1, k]$ (see Figure 4.4). The main difference between them is that $[k + 1, k]$ cases are FF close to the axis, while $[1, 1]$ is outward-NFF around the core, and has inward magnetic forces close to the boundary in the most unstable regime corresponding to small $\tilde{C}_{nm}$ (see Figure 4.3). In addition, low values of τ make the MFR be more kink unstable as well as inward-NFF around the boundary (as seen in Figure 4.3a, 4.3b and 4.3c). Does this mean that the presence of magnetic forces in opposite directions within the MFR and of inward forces around the edge favor the kink instability?

On the other hand, the boundary of the MFR becomes more outward-NFF at the edge for larger k in cases $[k + 1, k]$ and for high $\tilde{C}_{nm}$ (as seen in Figure 4.3b, 4.3d and 4.3e), which in turn imply an enhanced stability to kink. Has the presence of outward magnetic forces around the boundary of a MFR a kink stabilizing effect?

These questions should be addressed in future research to get more insights into how the kink stability is influenced by magnetic forces, as well as the heliospheric sources of non-force-freeness and the nature of the magnetic forces that they would induce on MFRs (inward or outward, around the core or close to the edge...).

With respect to constant-α FF fields, it is sometimes said in the literature that they are all energy-minimizing and thus stable states of the system. However, this statement is not accurate: as stated in section 3.1.2, Woltjer (1958) showed that, if the energy of a system with given helicity is at a minimum, then $\nabla \times \mathbf{B} = \alpha_0 \mathbf{B}$ for some α_0, but if $\nabla \times \mathbf{B} = \alpha_0 \mathbf{B}$, this only implies that the energy is an extremum but not necessarily a minimum. Therefore, it is not true that all constant-α fields are stable, as shown in the present work and in Voslamber and Callebaut (1962), where α_{crit} was found to be 3.176 for a Lundquist MFR enclosed by a perfectly conducting rigid wall.

4.2.3 Reversed chirality scenario and the kink instability

Another phenomenon that has been observed to occur for certain values of the CC and Lundquist parameters is the change of the sign of B_y at some distance from the MFR axis. In general, assuming that the magnetic field components around the axis are positive (with left-handed (L) chirality), three scenarios in which the sign of the magnetic field components change some distance away from the core can occur. The three possibilities are described in Table 4.3. The GH model does not admit any change in the sign of B_y or B_φ. Lundquist model with $\alpha > 2.4$, and the CC model with $\tau < 1$ for any $[n, m]$, correspond to option (b) in Table 4.3. Lundquist model also predicts an additional change in the MFR chirality if $\alpha > 3.83$, since B_φ becomes negative.

The results of the stability analysis have shown that a CC MFR is always kink unstable for $\tau \leq 1$ (see Figure 4.4), or in other words, option (b) is always kink unstable for the CC $[n, m]$ pairs studied. This is not the case for the Lundquist model, which can be stable in the reversed chirality scenario when $2.4 < \alpha < 3.2$. However, Lundquist double chirality reversal scenario ($\alpha > 3.83$) is kink unstable.

The fact that the Lundquist model remains kink stable in the reversed chirality scenario raises

Option	B properties				Sketch
	Part	B_y	B_φ	Chirality	
(a)	Int.	+	+	L	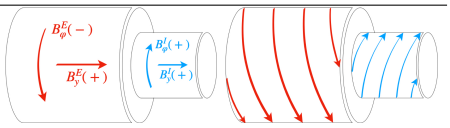
	Ext.	+	-	R	
(b)	Int.	+	+	L	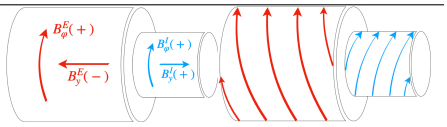
	Ext.	-	+	R	
(c)	Int.	+	+	L	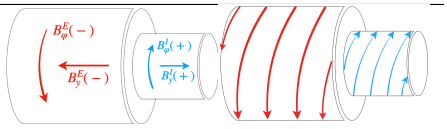
	Ext.	-	-	L	

Table 4.3: Description of the scenarios in which the sign of the magnetic field components changes at some distance from the MFR axis. The internal (int.) axial and poloidal magnetic fields are assumed to be always positive, so that the inner part of the MFR is left-handed (L). The different possibilities of change in the signs of the external (ext.) B_y and B_φ, and their corresponding chirality, are listed. Two sketches of each scenario are included to clarify the directions of the magnetic field components and the helices that they generate.

the question of how magnetic flux can be added in opposite directions during the first stages of the CME evolution. Some events have already been observed that support this hypothesis (Cho et al., 2013; Vemareddy and Démoulin, 2017). Moreover, theoretical studies have been done on the physical consequences of the reversed chirality scenario. For example, Einaudi (1990) found that MFRs with an inversion of the B_y sign have a much higher critical twist for instability and involve more drastic nonlinear evolution of the instability. In the thermonuclear fusion field, a similar magnetic configuration, the reversed field pinch (RFP), which is an axisymmetric toroidal structure with a change of the B_y sign (option (b) in Table 4.3), has been subject of extensive research for the confinement of laboratory plasmas, due to its being a minimum-energy state of the system and stable against localized MHD instabilities (Schwarzschild, 1981).

Nevertheless, further research on the stability and initiation of these MFR scenarios is needed to understand the physical processes that would be occurring and how they could have been generated. The consideration of an additional term of the axial current density of the CC model would also allow an inversion in the B_φ sign, and thus the stability of options (a) and (c) could be explored with the numerical method developed in this thesis.

4.2.4 Expansion and the kink instability

Regarding the evolution of interplanetary MFRs, some conclusions can also be inferred from the results of the stability analysis of the CC model. Equation (4.6) showed the relation between the parameters of an MFR with radius R and axial length L, and their values when it evolves into an MFR with radius $R' > R$ and axial length L': τ remains constant, so any change in the kink stability will be given exclusively by the variation of $\tilde{C}_{nm}$ ($\tilde{C}'_{nm} = \frac{L'}{L}\frac{R}{R'}\tilde{C}_{nm}$). Three possible scenarios can be identified in view of the results in Figure 4.4:

1. $L'/L < R'/R$: the rate of expansion of the axis length is smaller than the radial growth rate. In this scenario, $\tilde{C}'_{nm} < \tilde{C}_{nm}$, so an initially stable MFR can become unstable at some point of its propagation.

2. $L'/L = R'/R$: this scenario corresponds to that of self-similar expansion. $\tilde{C}'_{nm} = \tilde{C}_{nm}$, so no change in the kink stability is produced.

3. $L'/L > R'/R$: the rate of expansion of the axis length is bigger than the radial growth rate. In this case, $\tilde{C}'_{nm} > \tilde{C}_{nm}$, so an initially unstable MFR could become kink stable in the course of its evolution.

These results suggest that different types of interaction may change the stability of a CME and cause its rotation or its stabilization. Examples of each of the three scenarios are sketched in Figure 4.6. In case 1, an interaction taking place along the sides of a CME could slow down the axial length growth, while an interacting agent pushing the MFR front from behind could increase the radial growth rate. This would have a destabilizing effect on it and could cause its rotation, since $\tilde{C}'_{nm} < \tilde{C}_{nm}$. In case 2, without any interactions, the MFR would expand self-similarly and its kink stability would not be affected because $\tilde{C}'_{nm} = \tilde{C}_{nm}$. In case 3, an interaction acting on the front of the CME could slow down the radial growth. This would have a stabilizing effect, since $\tilde{C}'_{nm} > \tilde{C}_{nm}$.

The next step should be to test these hypotheses with the observational data, by inferring the ratios L'/L and R'/R from the parameters commonly used to characterize expanding CMEs in remote sensing observations (e.g. AW_D and AW_L in Cabello et al., 2016; Cremades et al., 2020, or V_{lat} and V_{front} in Balmaceda et al., in prep.). For example, the event detected on March 15, 2019, by PSP (analyzed in section 3.4) could correspond to scenario 3 because the cross-sectional radius inferred by *in situ* models was much smaller than the one predicted by self-similar expansion, so no rotation due to the internal magnetic configuration of the CME would be expected. Single events with $L'/L < R'/R$ (scenario 1) could then be selected and studied to see if they are likely to display rotation signatures during their evolution.

Further studies on the different types of interaction that could take place and their effect on the onset of CME rotations, as well as more comparisons with observational studies and other MFR models, are still needed to improve the current understanding of the evolution of CMEs and their kink stability.

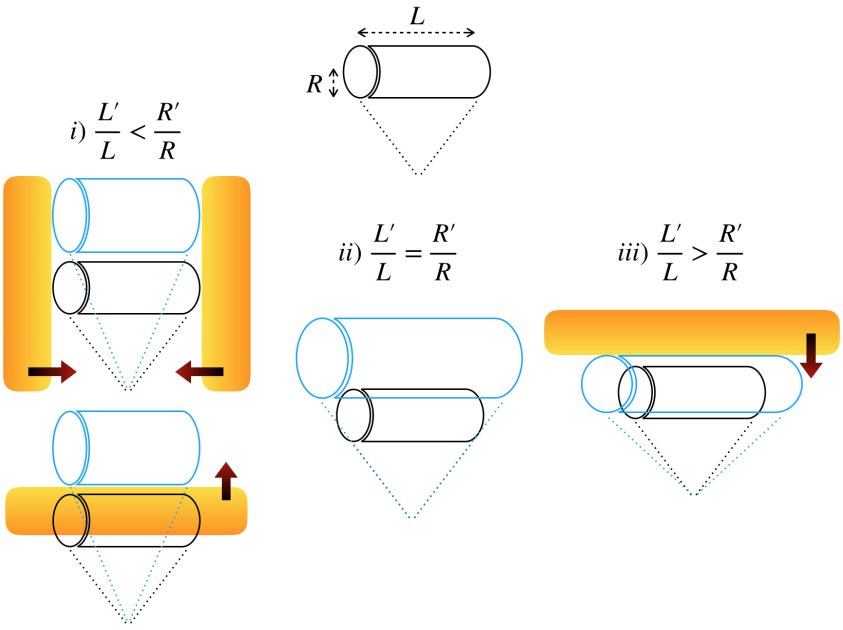

Figure 4.6: Top: schematic representation of an MFR, with the radius R and the axial length L indicated. Bottom: examples of different types of interaction that could be causing each of the three expansion scenarios. The black MFR is the original one, while the blue MFR represents the structure after expansion with radius R' and axial length L'. The orange rectangles are abstractions of possible interacting agents in the heliosphere, moving towards the MFR in the directions indicated by the arrows.

4.2.5 Further remarks

There are two basic types of theories describing the initiation of CMEs on the Sun: *on-the-fly MFR theories* assume that the MFR forms during the eruption due to a sequence of motions and reconnections, while *preformed MFR theories* assume that an MFR had already formed prior to the eruption. The second type of initiation scenario is more prone to generate MFRs with a stage-like twist distribution (the term is used to describe distributions that show different behavior of the twist around the core and in the outer shell), which coincides with the twist profile of CC $[k+1, k]$ cases for higher k (almost uniform around the axis and abruptly increasing close to the edge, as noted in section 4.1.2). On the other hand, MFRs with bigger k have been found to be more kink stable than other MFRs with the same B_y and B_φ at the boundary, as observed in Figure 4.4. Since the eruption of a CME requires the triggering of the kink instability, this could suggest that an MFR with continuously distributed twist (i.e. on-the-fly MFR theories) is a more likely initiation scenario than the corresponding more stable stage-like distribution (i.e. preformed MFR theories). However, in order to obtain physically meaningful conclusions, more exploration on the twist distribution that different initiation hypotheses of MFRs theoretically predict, and the analysis of the kink stability of MFR models with the corresponding twist profiles for each case, are still needed.

Finally, the study of the kink instability of MFRs can also help to review the choice of the parameters that is usually made for some models, as well as to find physical constraints for models that include multiple free parameters, in order to avoid the occurrence of the instability. For example, this analysis has shown that α in the Lundquist model can be varied around 2.4 before becoming unstable for $\alpha > 3.2$ (as discussed in Démoulin et al., 2019). Additionally, it has been found that the typical value $\tau = 1$ that is often used to fit events with the CC model results in the kink instability, for the pairs $[n, m]$ considered.

4.3 Study of optimal parameters for solar MHD simulations

The numerical method that has been developed in the present work (outlined in section 4.1.6) can also be used to study which values of the parameters of a particular MFR model will result in the onset of an instability with desirable characteristics, e.g. with the biggest growth rate or with a particular wavenumber k.

This was the case for a nonlinear MHD simulation that researchers Kalman Knizhnik and Mark Linton at NRL wanted to carry out, in order to study the role of the kink instability in the emergence of MFRs from the convection zone into the corona. The goal was to obtain the optimal parameters that gave the biggest growth rate for a particular instability wavelength that had been measured in the Sun through remote sensing observations. In this case, the model used to describe an emerging MFR of cross-sectional radius R is given by

$$\begin{cases} B_y(r) = B_0 \left(1 - \frac{r^2}{R^2}\right)^p \\ B_\varphi(r) = qrB_y(r), \end{cases}$$

where p and q are free parameters. The model is uniformly twisted with twist $Q = B_\varphi/(rB_y) = q$. We want to find a pair of p and q that results in a big growth rate for the instability for a sufficiently large wavelength Λ with magnitude of around $\Lambda \sim 10R$. The MFR under study has physical characteristics of $R = 1$ Mm, $L = 261$ Mm, $B_0 = 13$ T and $\rho_0 = 0.077$ kg/m^3, although they will not be needed for the analysis.

As mentioned in section 4.1.6, the numerical procedure that has been developed works with the adimensional parameters $\tilde{\lambda} = \lambda R^2/B_0^2, \tilde{k} = kR, \bar{r} = r/R, \tilde{q} = qR$. The wavelength Λ of the instability is related to the adimensional wavenumber $\tilde{k}$ of the code through

$$\Lambda = \frac{2\pi}{k} = \frac{2\pi}{\tilde{k}} R.$$

The maximum growth rate ω_{max} can be obtained in terms of the adimensional parameter $\tilde{\lambda}_{ext}$ of the code by taking into account that

$$\lambda = -4\pi\rho_0\omega^2 = \frac{\tilde{\lambda}B_0^2}{R^2}, \quad v_A = \sqrt{\frac{B_0^2}{4\pi\rho_0}}.$$

Therefore, $\tilde{\lambda}_{ext} = -\omega_{max}^2 R^2/v_A^2$, and the final result is

$$|\omega_{max}| = \frac{v_A}{R}\sqrt{\tilde{\lambda}_{ext}}.$$

The output parameters of the main subroutine of the numerical procedure were defined in section 4.1.6: $\tilde{k}_{min}$, $\tilde{k}_{max}$ (the minimum and maximum wavenumbers for which there is kink instability, respectively), $\tilde{k}_{ext}$ (the wavenumber for which the largest growth rate of the instability occurs), $\tilde{\lambda}_{ext}$ ($\tilde{\lambda}$ at which the largest growth rate of the instability occurs). These quantities are illustrated in Figure 4.7.

The variation of the exponent p for fixed values of qR makes the output parameters change, as can be observed in the example of Figure 4.8 for fixed $qR = 1.0$ and p adopting the values $p = 0.0, p = 0.1, p = 0.36$.

The parameter p is fixed to $p = 0.1$ since it is a value commonly used in the literature, and we will explore the variation of $k_{max}, k_{min}, k_{ext}, \lambda_{ext}$ in terms of q. Figure 4.9 shows the results. To find the stability threshold, we can approximate the quantities $\tilde{k}_{min}$ and $\tilde{k}_{max}$ with two lines and find their intersection. The result is that $q_{cr}R \sim 0.32$, which means that the MFR becomes linearly unstable when $q > q_{cr}$.

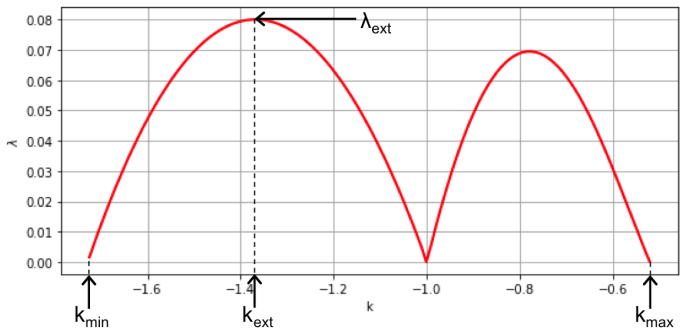

Figure 4.7: Graphical representation of the maximum $\tilde{\lambda}$ that solves the dispersion relation $D(\lambda; R, k) = 0$ (see equation (4.11)) as a function of of the wavenumber $\tilde{k}$, for the parameters $qR = 1.0$ and $p = 0.0$. The tildes on the parameters have been omitted to simplify the image.

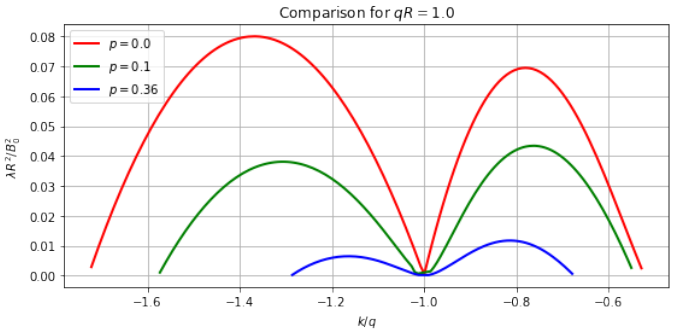

Figure 4.8: Comparison of the results for the biggest $\tilde{\lambda} = \lambda R^2/B_0^2$ solving the dispersion relation (4.11) as a function of k/q, for $qR = 1.0$.

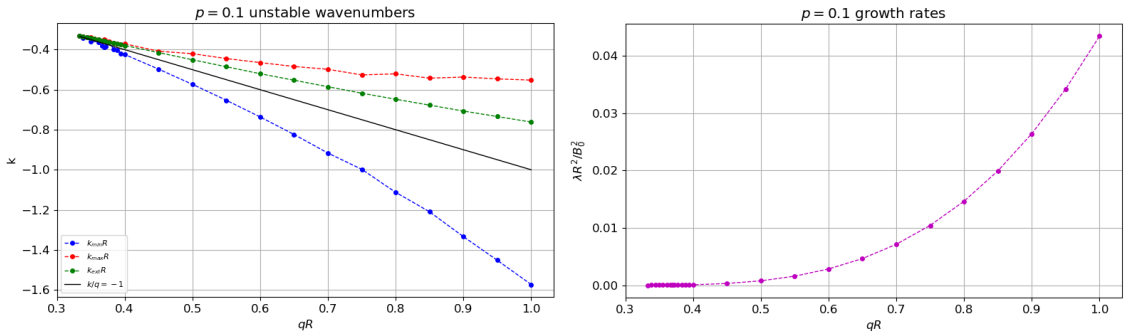

Figure 4.9: Output of the code for different values of qR and $p = 0.1$.

To find the wavelength Λ of the most unstable mode as a function of qR, we need to relate it to the code parameter $\tilde{k}_{ext}$ that gave the wavenumber at which the most unstable instability occurred. The pink dots in Figure 4.10 (left) represent the values of $\tilde{k}_{ext}$ found numerically for each qR. They display a linear behavior, so Λ is found as a function of qR as

$$k_{ext}R = c(qR) + d, \quad \begin{cases} c = -0.66213953 \\ d = -0.11361216 \end{cases},$$

which implies that

$$\Lambda = \frac{2\pi}{|c(qR) + d|}R. \tag{4.13}$$

This equation allows to predict the wavelength at which the maximum growth rate occurs for each value of qR. The plot of Λ is shown in Figure 4.10 (right).

To find the maximum growth rate $|\omega_{max}|$ as a function of qR, we need to relate it to the code parameter $\tilde{\lambda}_{ext}$. Figure 4.11 (left) shows that $\log(\sqrt{\tilde{\lambda}_{ext}}) = \log(\omega_{max}R/v_A)$ displays a linear behavior as a function of $\log((q^2 - q_{cr}^2)R^2)$, where q_{cr} was found to be $q_{cr}R = 0.32$. Therefore, taking into account that $|\omega_{max}| = v_A\sqrt{\tilde{\lambda}_{ext}}/R$, it can be approximated as

$$\log(\sqrt{\tilde{\lambda}_{ext}}) = a[\log((q^2 - q_{cr}^2)R^2)] + b, \quad \begin{cases} a = 1.21984623 \\ b = -1.34042807 \end{cases},$$

which ultimately gives

$$\omega_{max} = \frac{v_A}{R}e^{a[\log((q^2 - q_{cr}^2)R^2)]+b}. \tag{4.14}$$

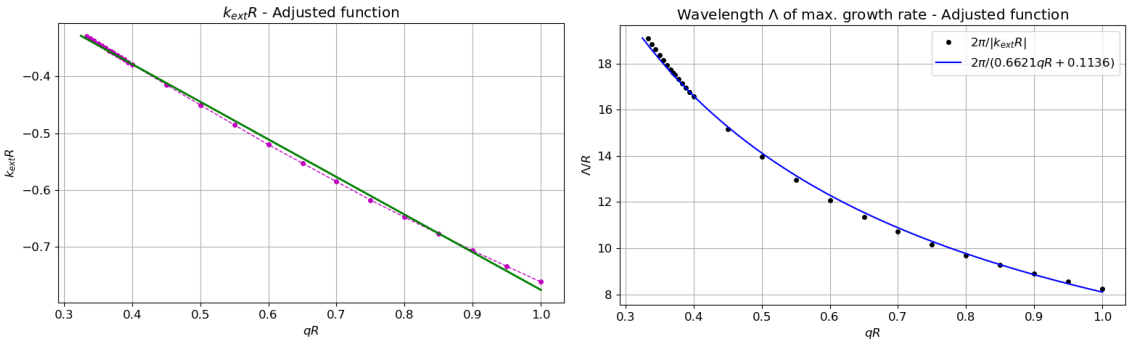

Figure 4.10: Left: The linear behavior of the interpolated points of $k_{ext}R$ is shown in magenta. The adjusted function $k_{ext}R = c(qR) + d$ is plotted in green. Right: Plot of the deduced wavelength Λ of each individually calculated qR (black dots), and the adjusted function of Eq. (4.13) (blue line).

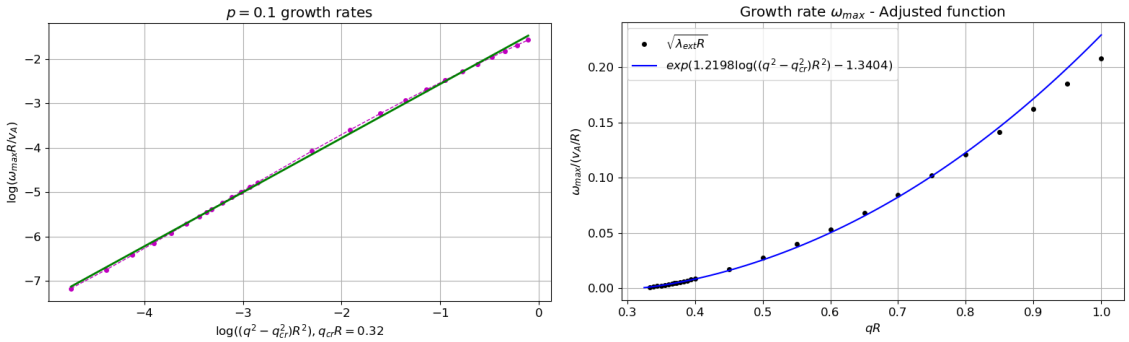

Figure 4.11: Left: The linear behavior of the interpolated points of $\log(\sqrt{\tilde{\lambda}_{ext}}) = \log(\omega_{max}R/v_A)$ is shown in magenta. The adjusted function $\log(\sqrt{\tilde{\lambda}_{ext}}) = a[\log((q^2 - q_{cr}^2)R^2)] + b$ is plotted in green. Right: Plot of the deduced maximum growth rate ω_{max} of each individually calculated qR (black dots), and the adjusted function of Eq. (4.14) (blue line).

This relation allows to predict the maximum growth rate for each value of qR, occurring at the wavelength Λ specified by Eq. (4.13). The plot of $|\omega_{max}|$ is shown in Figure 4.11 (right).

Finally, to get some insights into the behavior of the radial perturbation ξ_r, the Euler-Lagrange equation (4.7) can be solved for different values of qR, at the wavelength λ of maximum growth rate ω_{max} given by equations (4.13) and (4.14), respectively. The results are shown in Figure 4.12, where the instability is observed to be an internal motion of the plasma for $qR \in [0.6, 0.7]$ approximately, compressing the boundary for $qR < 0.6$, and expanding it for $qR > 0.7$.

Since the wavelength Λ decreases with qR and the growth rate ω_{max} increases with qR, a trade-off between them is needed. The final choice of parameters results in $qR = 1.0$ for $p = 0.1$, because the fastest growing mode that has been analyzed (with $\omega_{max} = 0.21 v_A/R$) gives a sufficiently large wavelength ($\Lambda = 8R$) for the purposes of the solar MHD simulations that will be done.

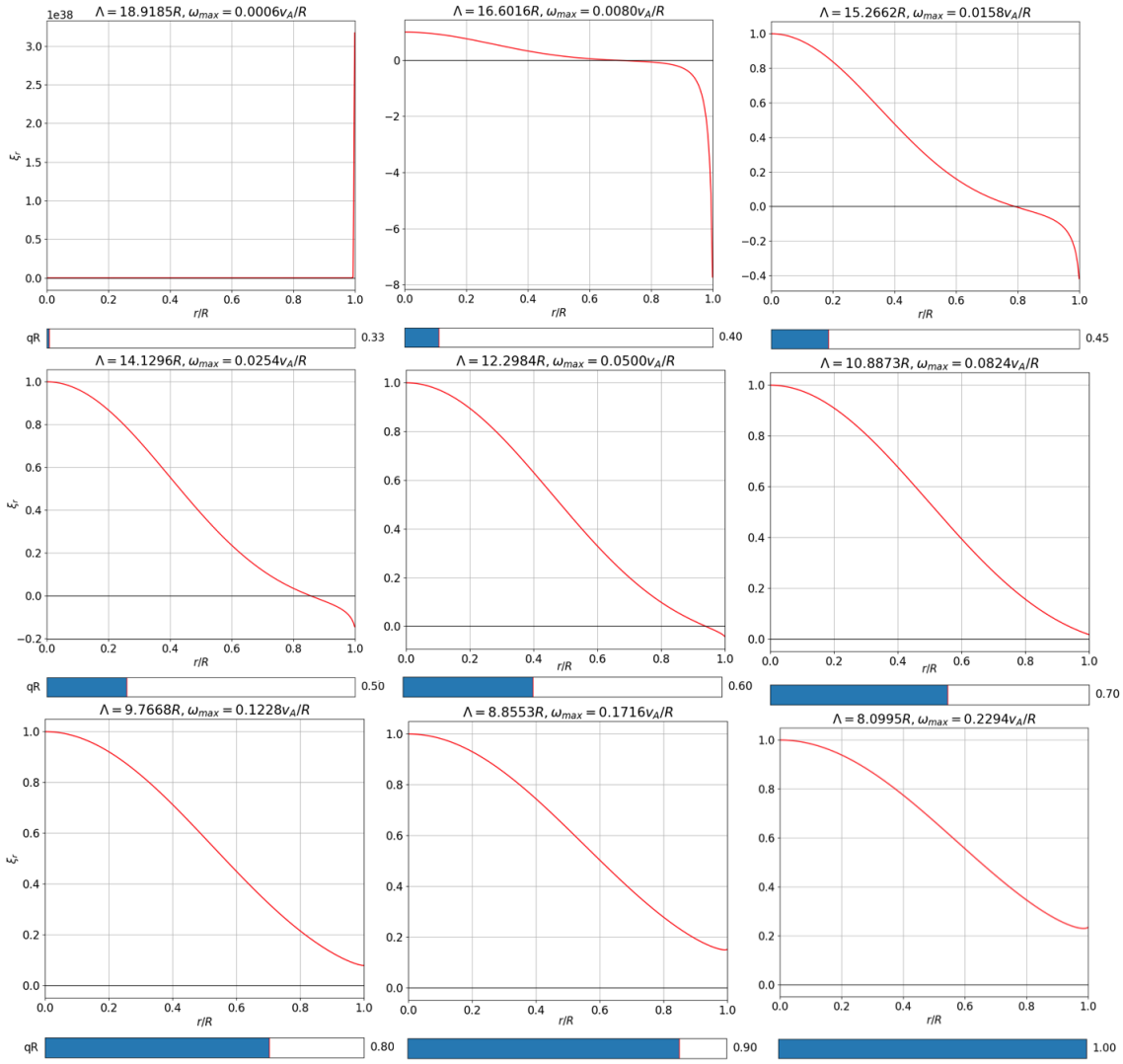

Figure 4.12: Shape of ξ_r for $qR = 0.33, 0.4, 0.45, 0.5, 0.6, 0.7, 0.8, 0.9, 1.0$. The wavelength Λ at with the maximum growth rate ω_{max} occurs for each qR, and ω_{max} (as computed with Eq. (4.13) and (4.14)) are indicated in the titles.

Summary and conclusions

In the present work, the internal magnetic configuration and dynamics of MFRs have been studied in terms of MFR modeling and plasma instabilities, with the aim of providing theoretical background to address fundamental questions about the twist distribution and the magnetic structure of a dynamically expanding MFR.

The inclusion of the expansion in the CC reconstruction technique has been studied, as well as the effect of conserved quantities on the physical parameters of the model. In addition, the GCS model and the EC model have been applied to a particular CME detected by PSP on March 15, 2019, to check their mutual consistency. The results have shown a big discrepancy in the cross-sectional radius predicted, which could be due to the fact that the self-similar expansion assumption is not realistic, and to the limitations imposed by the one-dimensional nature of *in situ* measurements.

Then, a numerical method has been developed and applied to study the kink instability of differently twisted MFR models. The stability thresholds found are shown in Table 4.2 and Figure 4.4. The kink instability has been discussed as a possible cause of CMEs rotations that are produced solely by their internal magnetic configuration, so the stability thresholds would actually indicate the range of parameters for which some MFRs are susceptible to rotate. Moreover, the analysis of the magnetic forces has shown that their occurrence in opposite directions within the MFR could have a strong destabilizing effect, while outward magnetic forces near the plasma edge could stabilize the structure.

More phenomena like the reversed chirality scenario or the expansion have also been considered. The occurrence of the kink instability in expanding MFRs described by the CC model depends on the ratio of the axial and radial expansion rates: an initially stable MFR could become unstable during its propagation if $L'/L < R'/R$, while $L'/L > R'/R$ would have a stabilizing effect. Self-similar expansion does not lead to changes in the kink stability of the system.

Finally, the numerical procedure developed has been used to obtain the optimal parameters for a nonlinear MHD simulation of the emergence of MFRs at the Sun, which lead to the onset of an instability with the desired wavelength and growth rate.

Bibliography

J. Allen, H. Sauer, L. Frank, and P. Reiff. Effects of the March 1989 solar activity. *Eos, Transactions American Geophysical Union*, 1989. DOI. URL.

L. Balmaceda, A. Vourlidas, G. Stenborg, and O. St. Cyr. On the expansion speed of Coronal Mass Ejections. Implications for self-similar evolution. *Solar Physics*, in prep.

G. Bateman. *MHD instabilities*. MIT Press, Cambridge, Mass, 1978.

P. M. Bellan, S. You, and S. C. Hsu. Simulating Astrophysical Jets in Laboratory Experiments. *Astrophysics and Space Science*, July 2005. DOI. URL.

D. B. Berdichevsky. On Fields and Mass Constraints for the Uniform Propagation of Magnetic-Flux Ropes Undergoing Isotropic Expansion. *Solar Physics*, May 2013. DOI. URL.

M. A. Berger and G. B. Field. The topological properties of magnetic helicity. *Journal of Fluid Mechanics*, Oct. 1984. DOI. URL.

I. B. Bernstein, E. A. Frieman, M. D. Kruskal, R. M. Kulsrud, and S. Chandrasekhar. An energy principle for hydromagnetic stability problems. *Proceedings of the Royal Society of London. Series A. Mathematical and Physical Sciences*, Feb. 1958. DOI. URL.

D. Biskamp. *Nonlinear magnetohydrodynamics*. Cambridge University Press, Cambridge, U.K.; New York, 1997. URL.

J. E. Borovsky and J. A. Valdivia. The Earth's Magnetosphere: A Systems Science Overview and Assessment. *Surveys in Geophysics*, Sept. 2018. DOI. URL.

R. P. Brent. *Algorithms for Minimization Without Derivatives*. Courier Corporation, June 2013.

L. Burlaga, E. Sittler, F. Mariani, and R. Schwenn. Magnetic loop behind an interplanetary shock: Voyager, Helios, and IMP 8 observations. *Journal of Geophysical Research: Space Physics*, 1981. DOI. URL.

I. Cabello, H. Cremades, L. Balmaceda, and I. Dohmen. First Simultaneous Views of the Axial and Lateral Perspectives of a Coronal Mass Ejection. *SoPh*, Aug. 2016. DOI. URL.

F. F. Chen. *Introduction to Plasma Physics and Controlled Fusion: Volume 1: Plasma Physics*. Springer US, 2 edition, 1984. DOI. URL.

K.-S. Cho, S.-H. Park, K. Marubashi, N. Gopalswamy, S. Akiyama, S. Yashiro, R.-S. Kim, and E.-K. Lim. Comparison of Helicity Signs in Interplanetary CMEs and Their Solar Source Regions. *Solar Physics*, May 2013. DOI. URL.

H. Cremades, F. A. Iglesias, and L. A. Merenda. Asymmetric expansion of coronal mass ejections in the low corona. *arXiv*, Jan. 2020. URL.

S. Dasso, C. H. Mandrini, P. DéMoulin, and C. J. Farrugia. Magnetic helicity analysis of an interplanetary twisted flux tube. *Journal of Geophysical Research (Space Physics)*, Oct. 2003. DOI. URL.

P. A. Davidson. *An Introduction to Magnetohydrodynamics*. Mar. 2001. URL.

J. Dungey and R. Loughhead. Twisted Magnetic Fields in Conducting Fluids. *Australian Journal of Physics*, 1954. DOI. URL.

P. Démoulin, S. Dasso, M. Janvier, and V. Lanabere. Re-analysis of Lepping's Fitting Method for Magnetic Clouds: Lundquist Fit Reloaded. *Solar Physics*, Dec. 2019. DOI. URL.

G. Einaudi. Ideal instabilities in a magnetic flux tube. *GMS*, 1990. URL.

M. Florido-Llinas, T. Nieves-Chinchilla, and M. G. Linton. Analysis of the helical kink stability of differently twisted magnetic flux ropes. *Solar Physics*, in review.

P. Foukal. *Solar astrophysics*. 1990. URL.

J. P. Freidberg. *Plasma physics and fusion energy*. Cambridge University Press, Cambridge, 2007.

J. P. Freidberg. *Ideal MHD*. 2014.

J. P. H. Goedbloed and S. Poedts. *Principles of Magnetohydrodynamics*. Cambridge University Press, Cambridge, GBR, 2010. URL.

M. González-Álvarez. *Analysis of Interplanetary Coronal Mass Ejections Observed by STEREO and MESSENGER*. Bachelor Thesis, Universitat Politècnica de Catalunya, May 2019. URL.

J. Harvey. Hale's Discovery of Sunspot Magnetic Fields. *The Astrophysical Journal*, Nov. 1999. URL.

A. Hassanin and B. Kliem. Helical Kink Instability in a Confined Solar Eruption. *The Astrophysical Journal*, Dec. 2016. DOI. URL.

A. W. Hood and E. R. Priest. Critical conditions for magnetic instabilities in force-free coronal loops. *Geophysical & Astrophysical Fluid Dynamics*, Jan. 1981. DOI. URL.

T. Howard. *Coronal Mass Ejections: An Introduction*. Astrophysics and Space Science Library. Springer-Verlag, New York, 2011. DOI. URL.

S. Q. Hu. The Grad-Shafranov reconstruction in twenty years: 1996-2016. *Science China Earth Sciences*, Aug. 2017. DOI. URL.

S. W. Kahler, S. Krucker, and A. Szabo. Solar energetic electron probes of magnetic cloud field line lengths. *Journal of Geophysical Research: Space Physics*, 2011. DOI. URL.

M.-B. Kallenrode. *Space Physics: An Introduction to Plasmas and Particles in the Heliosphere and Magnetospheres*. Springer Science & Business Media, Mar. 2004.

K. J. Knizhnik, M. G. Linton, and C. R. DeVore. The Role of Twist in Kinked Flux Rope Emergence and Delta-spot Formation. *The Astrophysical Journal*, Sept. 2018. DOI. URL.

V. Lanabere, S. Dasso, P. Démoulin, M. Janvier, L. Rodriguez, and J. J. Masías-Meza. Magnetic twist profile inside magnetic clouds derived with a superposed epoch analysis. *Astronomy and Astrophysics*, Mar. 2020. DOI. URL.

D. Lario, L. Balmaceda, M. Mays, N. Alzate, I. Richardson, R. Allen, M. Florido-Llinas, T. Nieves-Chinchilla, A. Koval, C. Arge, P. Macneice, D. Odstrcil, N. Lugaz, L. Jian, A. Szabo, M. Desai, P. Whittlesey, M. Stevens, G. Ho, and J. Luhmann. The Streamer Blowout Origin of a Flux Rope and Energetic Particle Event Observed by Parker Solar Probe at 0.5 AU. *The Astrophysical Journal*, in review.

R. P. Lepping, J. A. Jones, and L. F. Burlaga. Magnetic field structure of interplanetary magnetic clouds at 1 AU. *Journal of Geophysical Research*, 1990. DOI. URL.

R. P. Lepping, D. B. Berdichevsky, C.-C. Wu, A. Szabo, T. Narock, F. Mariani, A. J. Lazarus, and A. J. Quivers. A summary of WIND magnetic clouds for years 1995-2003: model-fitted parameters, associated errors and classifications. *Annales Geophysicae*, Mar. 2006. DOI. URL.

A. E. Lifschitz. *Magnetohydrodynamics and spectral theory*. Developments in electromagnetic theory and applications. Kluwer Academic Publishers, Dordrecht, Boston, 1989.

M. G. Linton, D. W. Longcope, and G. H. Fisher. The Helical Kink Instability of Isolated, Twisted Magnetic Flux Tubes. *The Astrophysical Journal*, Oct. 1996. DOI. URL.

D. W. Longcope, G. H. Fisher, and S. Arendt. The Evolution and Fragmentation of Rising Magnetic Flux Tubes. *The Astrophysical Journal*, June 1996. DOI. URL.

S. Lundquist. On the Stability of Magneto-Hydrostatic Fields. *Physical Review*, July 1951. DOI. URL.

Z. Mikic, D. D. Schnack, and G. van Hoven. Dynamical Evolution of Twisted Magnetic Flux Tubes. I. Equilibrium and Linear Stability. *The Astrophysical Journal*, Oct. 1990. DOI. URL.

R. Mitalas and K. R. Sills. On the photon diffusion time scale for the sun. *The Astrophysical Journal*, Dec. 1992. DOI. URL.

C. E. Myers, M. Yamada, H. Ji, J. Yoo, W. Fox, J. Jara-Almonte, A. Savcheva, and E. E. Deluca. A dynamic magnetic tension force as the cause of failed solar eruptions. *Nature*, Dec. 2015. DOI. URL.

NASA Image and Video Library. URL.

National Research Council. Severe Space Weather Events: Understanding Societal and Economic Impacts: A Workshop Report. Technical report, Washington, DC: The National Academies Press, Dec. 2008. URL.

T. Nieves-Chinchilla. Modeling Heliospheric Flux Ropes: A Comparative Study of Physical Quantities. *IEEE Transactions on Plasma Science*, July 2018. DOI. URL.

T. Nieves-Chinchilla, M. G. Linton, M. A. Hidalgo, A. Vourlidas, N. P. Savani, A. Szabo, C. Farrugia, and W. Yu. A Circular-cylindrical Flux-rope Analytical Model for Magnetic Clouds. *The Astrophysical Journal*, May 2016. DOI. URL.

T. Nieves-Chinchilla, L. F. Guedes dos Santos, A. Vourlidas, N. A. Al-Haddad, N. Savani, and A. Szabo. Reconstruction of the near-Earth interplanetary coronal mass ejections during 1995-2015: Catalog of geometrical and physical properties. *AGUFM*, Dec. 2018a. URL.

T. Nieves-Chinchilla, M. G. Linton, M. A. Hidalgo, and A. Vourlidas. Elliptic-cylindrical Analytical Flux Rope Model for Magnetic Clouds. *The Astrophysical Journal*, July 2018b. DOI. URL.

T. Nieves-Chinchilla, A. Vourlidas, J. C. Raymond, M. G. Linton, N. Al-haddad, N. P. Savani, A. Szabo, and M. A. Hidalgo. Understanding the Internal Magnetic Field Configurations of ICMEs Using More than 20 Years of Wind Observations. *Solar Physics*, Feb. 2018c. DOI. URL.

T. Nieves-Chinchilla, R. Colaninno, A. Vourlidas, A. Szabo, R. P. Lepping, S. A. Boardsen, B. J. Anderson, and H. Korth. Remote and in situ observations of an unusual Earth-directed coronal mass ejection from multiple viewpoints. *Journal of Geophysical Research: Space Physics*, 2012. DOI. URL.

T. Oliphant. SciPy/integrate/odepack.py. URL.

E. J. Oughton, A. Skelton, R. B. Horne, A. W. P. Thomson, and C. T. Gaunt. Quantifying the daily economic impact of extreme space weather due to failure in electricity transmission infrastructure. *Space Weather*, 2017. DOI. URL.

E. Priest. *Magnetohydrodynamics of the Sun*. Cambridge University Press, Cambridge, 2013. DOI. URL.

M. R. E. Proctor, A. D. Gilbert, and Cambridge University Press. *Lectures on Solar and Planetary Dynamos*. Cambridge University Press, Cambridge, 1995.

H. Rinne. *The Weibull distribution: a handbook*. CRC Press, Boca Raton, 2009.

Z. J. Rong, W. X. Wan, C. Shen, T. L. Zhang, A. T. Y. Lui, Y. Wang, M. W. Dunlop, Y. C. Zhang, and Q.-G. Zong. Method for inferring the axis orientation of cylindrical magnetic flux rope based on single-point measurement. *Journal of Geophysical Research (Space Physics)*, Jan. 2013. DOI. URL.

M. Schuessler. Magnetic buoyancy revisited: analytical and numerical results for rising flux tubes. *A&A*, Jan. 1979. URL.

B. M. Schwarzschild. Reversed-field pinch stable 8 msec. *PhT*, 1981. DOI. URL.

J. Stenflo. History of Solar Magnetic Fields since George Ellery Hale. *Space Science Reviews*, Sept. 2017. DOI. URL.

STEREO Mission Official Website. URL.

A. Thernisien, A. Vourlidas, and R. A. Howard. Forward Modeling of Coronal Mass Ejections Using STEREO/SECCHI Data. *Solar Physics*, May 2009. DOI. URL.

T. Török and B. Kliem. Confined and Ejective Eruptions of Kink-unstable Flux Ropes. *The Astrophysical Journal*, Sept. 2005. DOI. URL.

J. M. Vaquero, M. C. Gallego, and J. A. García. A 250-year cycle in naked-eye observations of sunspots: A 250-year cycle in naked-eye observations of sunspots. *Geophysical Research Letters*, Oct. 2002. DOI. URL.

P. Vemareddy and P. Démoulin. Successive Injection of Opposite Magnetic Helicity in Solar Active Region NOAA 11928. *Astronomy & Astrophysics*, Jan. 2017. DOI. URL.

D. Voslamber and D. K. Callebaut. Stability of Force-Free Magnetic Fields. *Physical Review*, Dec. 1962. DOI. URL.

A. Vourlidas, R. Colaninno, T. Nieves-Chinchilla, and G. Stenborg. The First Observation of a Rapidly Rotating Coronal Mass Ejection in the Middle Corona. *The Astrophysical Journal*, June 2011. DOI. URL.

Y. Wang, B. Zhuang, Q. Hu, R. Liu, C. Shen, and Y. Chi. On the twists of interplanetary magnetic flux ropes observed at 1 AU. *Journal of Geophysical Research: Space Physics*, 2016. DOI. URL.

L. Woltjer. A Theorem on Force-Free Magnetic Fields. *Proceedings of the National Academy of Science*, June 1958. DOI. URL.

H. Zohm. *Magnetohydrodynamic Stability of Tokamaks*. John Wiley & Sons, Feb. 2015.